

4 Identify hangingwall deformation mechanisms and their impact on tendon performance requirements

4.1 Introduction

The focus of this section is on hangingwall deformation mechanisms and the influence thereof on rockbolting in the immediate stope face area. The mine visits (discussed in Chapter 2) showed that rockbolting is used on various mines on which different geotechnical and geological rock mass conditions prevail. It was earlier indicated that most of the mines that use rockbolting are mining at relatively shallow depths (less than 1600 m below surface). In shallow mining conditions, joints are very common, whereas in deep mining environments fractures are more common. If the hangingwall consists of a layered rock type (e.g. quartzites), bedding planes are present in the hangingwall, whereas with a hangingwall consisting of a rock type such as lava, no bedding planes will be found in the hangingwall. The stope widths in which the rockbolts are installed varies from approximately 1 m to 5 m.

In the following sections the different hangingwall deformation mechanisms under static conditions are identified by means of numerical modelling and underground observations. The effects of hangingwall deformation mechanisms on rockbolt performance requirements are investigated and the effect of cable anchors on the peak particle velocities of rock blocks under dynamic loading is analysed.

4.2 Rockbolting at the stope face

4.2.1 Introduction

This investigation forms part of the identification of deformation mechanisms existing in hangingwall strata and their impact on rockbolt performance requirements. The scope of work contained in this section cover the numerical modelling of rockbolt reinforcement of the stope face hangingwall.

The stability of the stope face area is critical with regard to the safety of the workers in this area and the productivity of the stoping operation with respect to face availability. Stabilisation of the rock mass in this area of the stope excavation has traditionally relied upon prop units, which have enabled successful mining of many production areas. However, the use of prop units does impede access to the face area for drilling and cleaning operations, may necessitate removal prior to blasting or be at risk of being displaced during the blasting operation, often making the immediate face area relatively poorly supported immediately after the blast.

An opportunity thus exists for the possible introduction of rockbolting technologies in the immediate face area of stopes, which may be more effective and efficient than the current support technology. Rockbolting must provide suitable reinforcement and support capacities, while potentially providing improved face area stability immediately after the blast and improved access for face area operations.

4.2.2 Rock mass instability and mechanisms of rockbolt interaction

Fundamental to the use of any rock mass reinforcement system is an understanding of the interaction between the reinforcement unit and the rock mass. This enables an appropriate reinforcement design for the envisaged mechanisms of rock mass instability. Typical rockbolt reinforcement schemes, adapted for stope hangingwall reinforcement, are illustrated in Figure 4.2.1. A critical point of differentiation in the mechanism of rock mass reinforcement is the relationship between the anticipated depth of rock mass instability and the depth of penetration of the rock mass reinforcement. That is, if the rockbolt installation is such that it has sufficient depth of anchorage to be external to the depth of anticipated instability, then analysis of stability may be based on the mechanism of suspension. If the depth of anchorage does not exceed the depth of instability, then ensuring stability of the hangingwall must rely on the creation of a reinforced rock mass structure. The depth of anchorage will be a function of the length of the rockbolt unit and the inclination of the installation. Typically, unless specialised drilling is utilised, the maximum depth of anchorage will always be less than the stoping width at the point of installation.

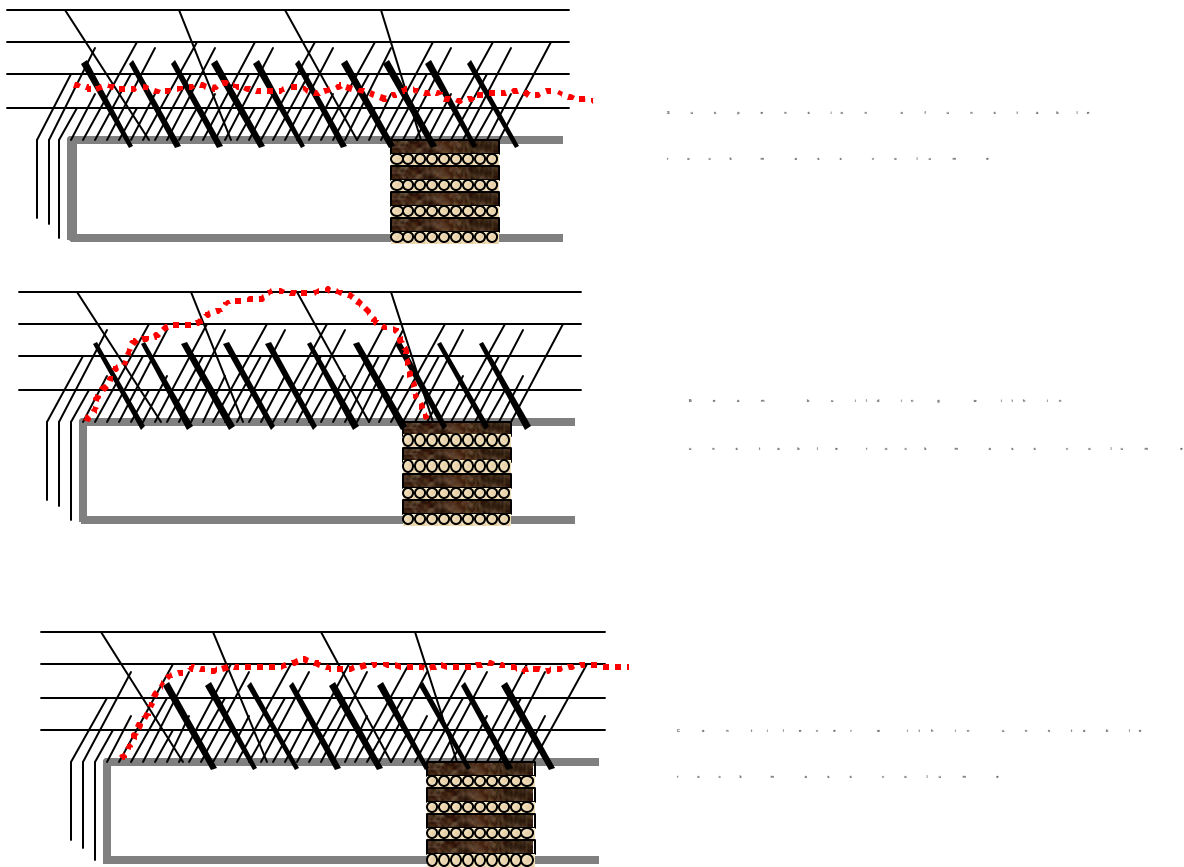


Figure 4.2.1 Rockbolt reinforcement and support schemes for stope face area stability.

When considering a rockbolt reinforcement scheme, the interaction of the individual rockbolts within the rock mass will determine the capacity of the reinforced structure to carry load and the potential instability of the rock mass between the rockbolt units. The inherent instability of a hangingwall rock mass has been found to be dependent principally on the structure of the rock mass in relation to the orientation and installation density of the rockbolt reinforcement. It can be envisaged, and has been

shown in SIMRAC project GAP 335 (Haile *et al.*, 1998), that an increase in the density of discontinuities in the rock mass, and an increased persistence of discontinuities sub-parallel to the axis of the rockbolt installation, results in reduced rockbolt interaction and lower reinforcement capacity.

4.2.3 Envisaged evaluation and design process

At this preliminary stage the investigation of rockbolting has considered a conceptual design process to assist in envisaging the potential outputs of the research, its practical application and the definition of areas of investigation within future research programmes. The simplified steps in this design process are shown in Figure 4.2.2.

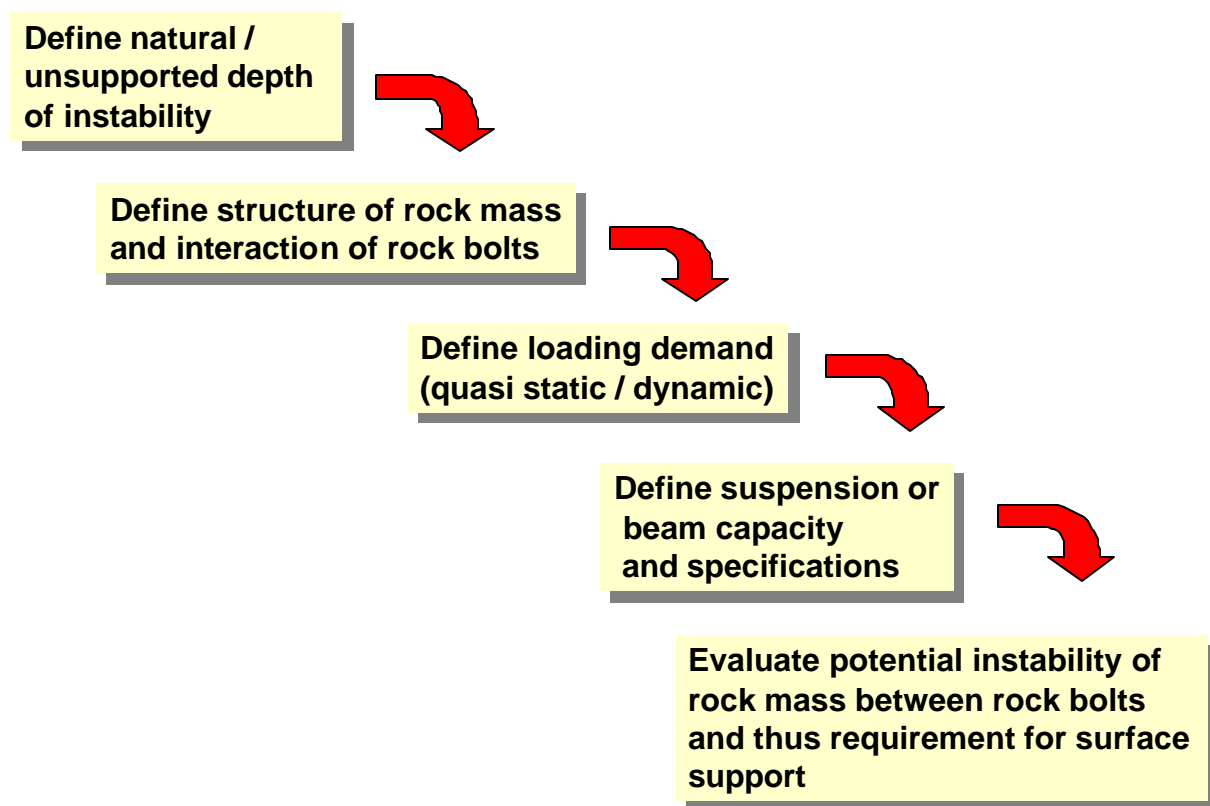


Figure 4.2.2 Conceptual design process for slope face rockbolting.

The major components of the design process are:

- the estimation of the depth of rock mass instability and loading conditions (quasi static / dynamic);
- the mechanism of rock mass stabilisation by the appropriate reinforcement and support scheme; and
- the estimation of the potential for rock mass instability between the rockbolt reinforcement.

This evaluation of the potential for the use of rockbolting in the stope face area has been restricted to the consideration of preventing hangingwall unravelling by the creation of a reinforced rock mass structure. This aims to satisfy objectives including mechanistic qualification of the controlling parameters such as the rock mass structure and assessment of performance of current support systems and loading conditions. Numerical modelling has been selected to enable this mechanistic evaluation of the interaction between the rockbolt reinforcement and the rock mass in the stope face environment.

4.2.4 Numerical modelling evaluation

The numerical modelling evaluation has been conducted using the two-dimensional Universal Distinct Element Code (Itasca, 1996), as this is considered to adequately capture the mechanisms of reinforcement within a pre-existing discontinuous rock mass structure. The additional complexity of a three-dimensional numerical model is considered inappropriate for this preliminary level of investigation.

The model has been constructed to idealistically represent the hangingwall rock mass in the immediate stope face area. The approximate dimensions of the model shown in Figure 4.2.3 are 5 m on strike and 1,5 m of hangingwall height. The influence of the face abutment and back area support is represented by the application of boundary conditions to this discontinuous model. Rockbolt reinforcement is modelled explicitly by joint reinforcement or cabling elements with axial and shear characteristics representative of a typical 16 mm, grout-encapsulated rockbolt. Loading of the model is applied through incremental increase in “gravitational” acceleration. As this load is applied in an incremental manner the load-deformation response of the structure is monitored via a FISH function (UDEEC’s macro language) to capture the capacity (energy absorption) of the structure.

The performance of a reinforced rock mass system is evaluated on the basis of the whole structure as opposed to the performance of the individual rockbolt unit. The design capacity of the reinforced structure, by maximising the inherent rock mass strength, may exceed that historically estimated by analysis of the rockbolt unit alone.

An example of the numerical analysis is shown in Figure 4.2.3.

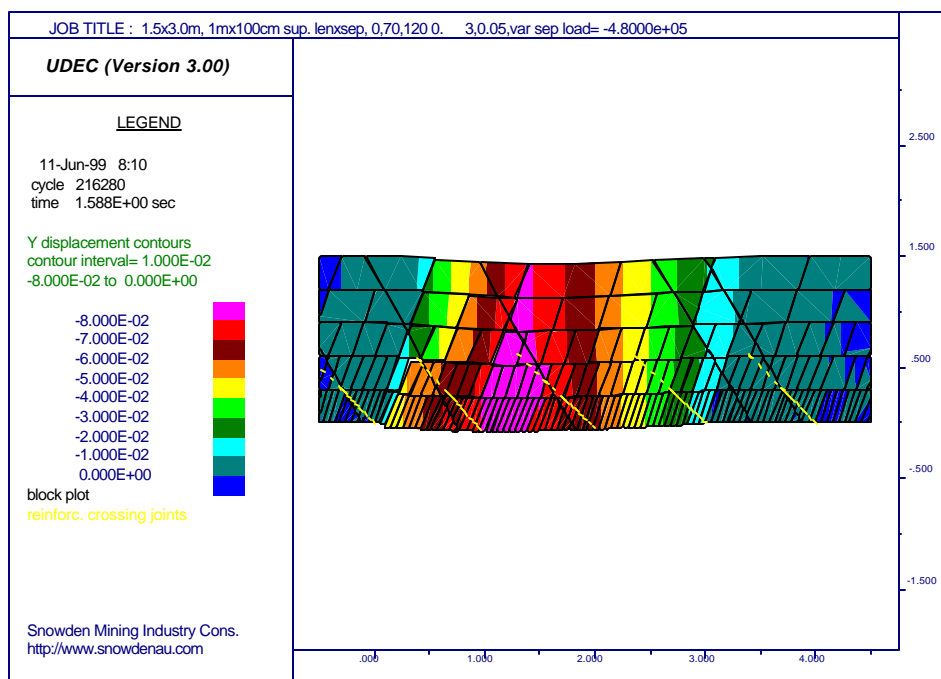


Figure 4.2.3 Example of UDEC modelling of reinforced stope face hangingwall structure.

The rock mass characteristics as used in this evaluation are summarised in Table 4.2.1

Table 4.2.1 Summary of rock mass properties used for numerical evaluation.

Rock mass property	Value
Bulk modulus (GPa)	40
Shear Modulus (GPa)	28
Density (kg/m ³)	2750
Joint friction (°)	35
Joint cohesion (MPa)	0
Joint tension (MPa)	0
Joint normal and shear stiffness (GPa/m)	10
Joint spacing (m)	variable
Joint angle (°)	variable

4.2.4.1 Rockbolt reinforcement parameters

The numerical modelling work has focused on the effectiveness of rockbolt reinforcement for the creation of a reinforced rock mass structure in the stope face area. That is, the length of the rockbolt units or inclination is such that there is insufficient depth of penetration to provide effective anchorage of the immediate hangingwall rock mass to deeper, more stable ground.

The relationships between rockbolt length and spacing on reinforced rock mass capacity are illustrated in Figures 4.2.4 and 4.2.5 respectively. The energy calculations are based on the area under the load-deformation characteristic of the structure (reinforced rock mass system, as derived from a fish function) to a point where this significantly deviated from linear. Models were taken to failure but energy absorption capacity analysis was only considered for the portion of deformation characteristic, which was considered stable.

These relationships verify the concept that, within a typically fractured rock mass structure (Figure 4.2.3), there are limitations to the extent of rockbolt interaction. Based on the assumed rock mass characteristics, a rockbolt length of less than 0,5 m (at 0,5 m spacing) and spacing greater than 1,0 m (for a 1,0 m rockbolt length) are found to be ineffective in enhancing the integrity of the hangingwall rock mass. Based on the numerical modelling results, this may imply a minimum ratio between rockbolt length and spacing (in this case 1:1) for a given rock mass structure.

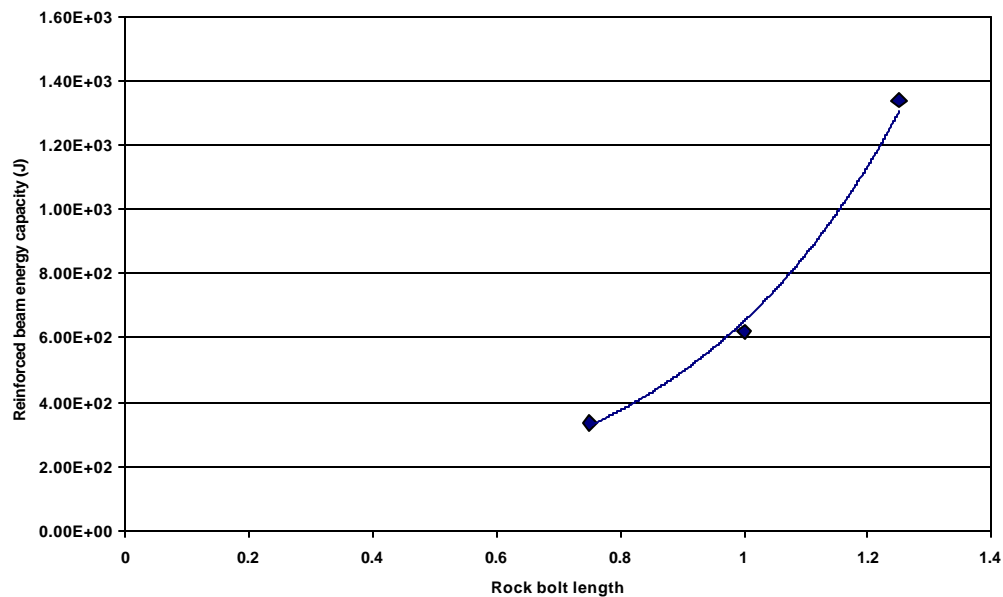


Figure 4.2.4 Relative influence of rockbolt length (at 0.5 metre spacing) on reinforced beam capacity.

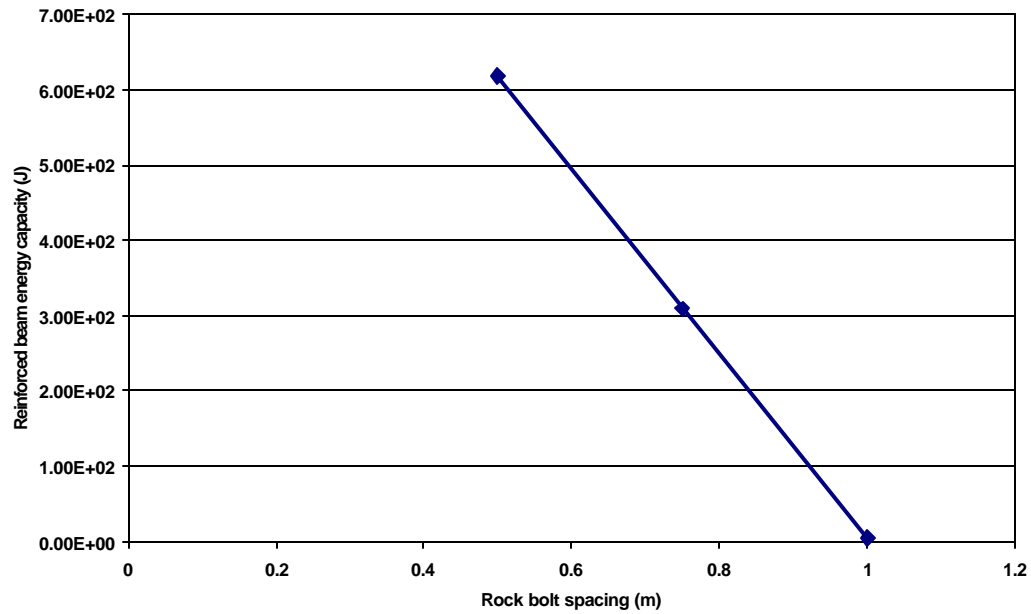


Figure 4.2.5 Relative influence of rockbolt spacing (at 1,0 m rockbolt length) on reinforced beam capacity.

It is clear that, as the rockbolt length increases, so to does the thickness of the reinforced rock mass. The relationship in Figure 4.2.4 shows the reinforced rock mass capacity to be approximately proportional to the cube of the rockbolt length. Due to the similarity of this relationship with that of the relationship between beam load and beam thickness in theoretical beam analysis, this may be directly attributed to the increased reinforced thickness. The increased reinforced rock mass capacity with increased rockbolt reinforcement density (Figure 4.2.5) is found to be attributable to an increased stiffness of the structure for fairly comparable ultimate beam deflections.

The inclination of rockbolt installation will influence both the thickness of the reinforced rock mass structure and the mechanism of interaction between the rockbolt and the discontinuities within the rock mass. Relative to the horizontal, a low angle of inclination results in reduced thickness of reinforcement of the hangingwall rock mass. As discussed above, this may produce a reduced reinforced beam capacity, as would also result from a reduction in rockbolt length. However, a reduction in rockbolt inclination will also result in a change in the rockbolt loading characteristic and the degree of overlap of adjacent rows of reinforcement. This mechanism of increased reinforcing action with reduced reinforcement thickness, for the current numerical model assumptions, appears to dominate the behaviour of the system (Figure 4.2.6). The mechanisms of rockbolt and rock mass interaction would require a far more detailed analysis, beyond the scope of this general analysis, to obtain an understanding of the relative contribution of the respective system mechanisms.

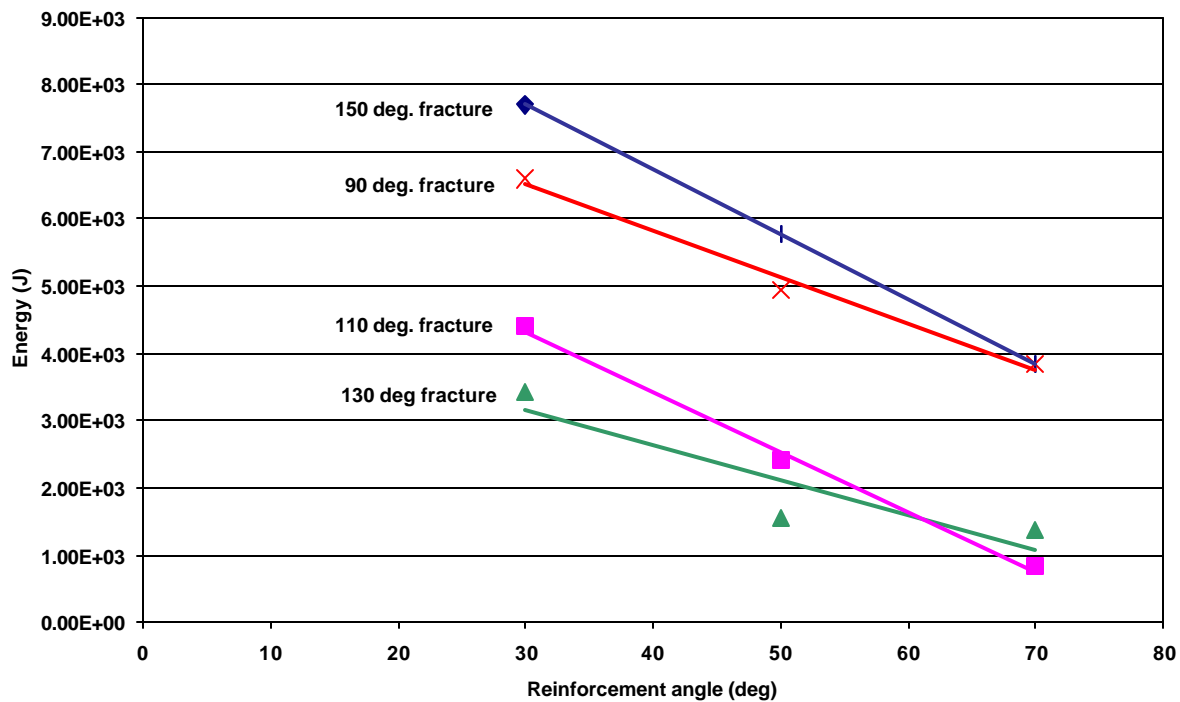


Figure 4.2.6 Influence of rockbolt inclination (at 1.0 metre rockbolt length and spacing of 0,5 m) and fracture inclination on reinforced beam capacity.

An important layout design component for the relative stability of the stope face area is the length of the exposed stope hangingwall span. Again, as would be anticipated, the characteristics of the numerical model capture the overall reduction in relative stability with increasing span (Figure 4.2.7). Significant relative improvement in stability (100 %) can be obtained by reducing the exposed, although reinforced, hangingwall span from 4 m to 2,5 m. However, the indicated improvement in performance of the numerical model is significantly lower than would be predicted from theoretical beam analysis.

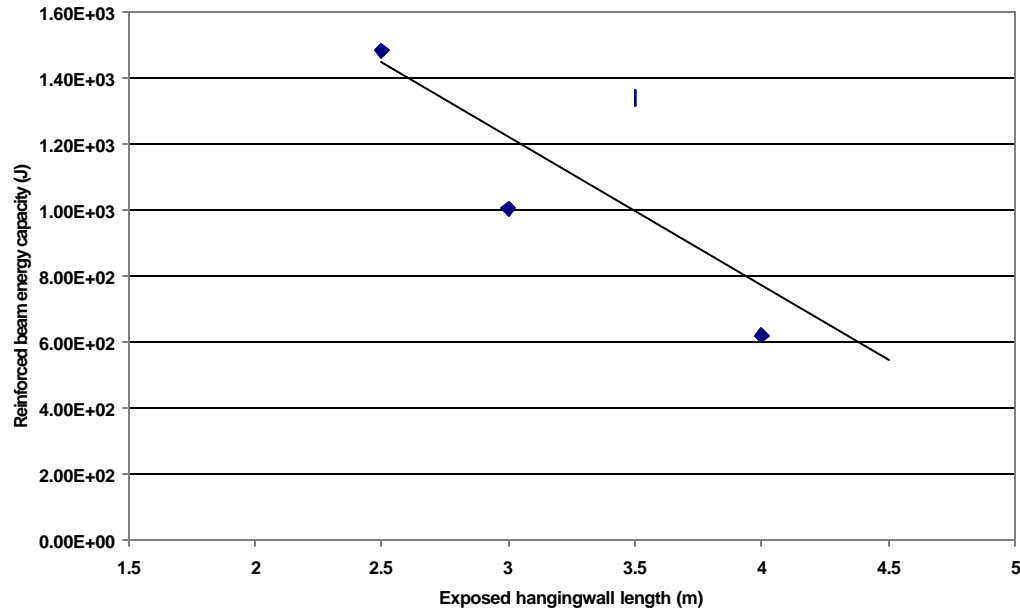


Figure 4.2.7 Relative influence of stope face area hangingwall span on reinforced beam capacity (1 metre bolts, 70° at 0,5 metre spacing).

4.2.4.2 Rock mass structure parameters

The structural characteristics of the rock mass will also influence the capability of rockbolting to maintain a competent hangingwall in the exposed stope face area. In this analysis, a simple representation of the rock mass structure, with 'general' discontinuity properties, has again been assumed.

The primary design consideration would probably be the influence of the angle of fracturing relative to the stope hangingwall and reinforcement orientation. This will influence both the inherent stability of the rock mass and the effectiveness of rockbolt reinforcement. Where the fractures are sub-vertical, the inherent rock mass strength will be high. As the angle of stope fracturing tends towards sub-horizontal and dipping towards the face, the inherent rock mass strength is reduced due to the increased potential for shearing and spalling. However, in this lower fracture angle environment the effectiveness of sub-vertical rockbolting increases. These mechanisms are illustrated by the results from the numerical modelling exercise (Figure 4.2.8) for various inclinations of rockbolt reinforcement, and are comparable to the characteristics of reinforcement interaction and excavation stabilisation observed in tunnels (Haile *et al.*, 1998). It is of interest to note the increased reinforcing action of low angle rockbolts, as also discussed in Section 4.2.4.1 of this report.

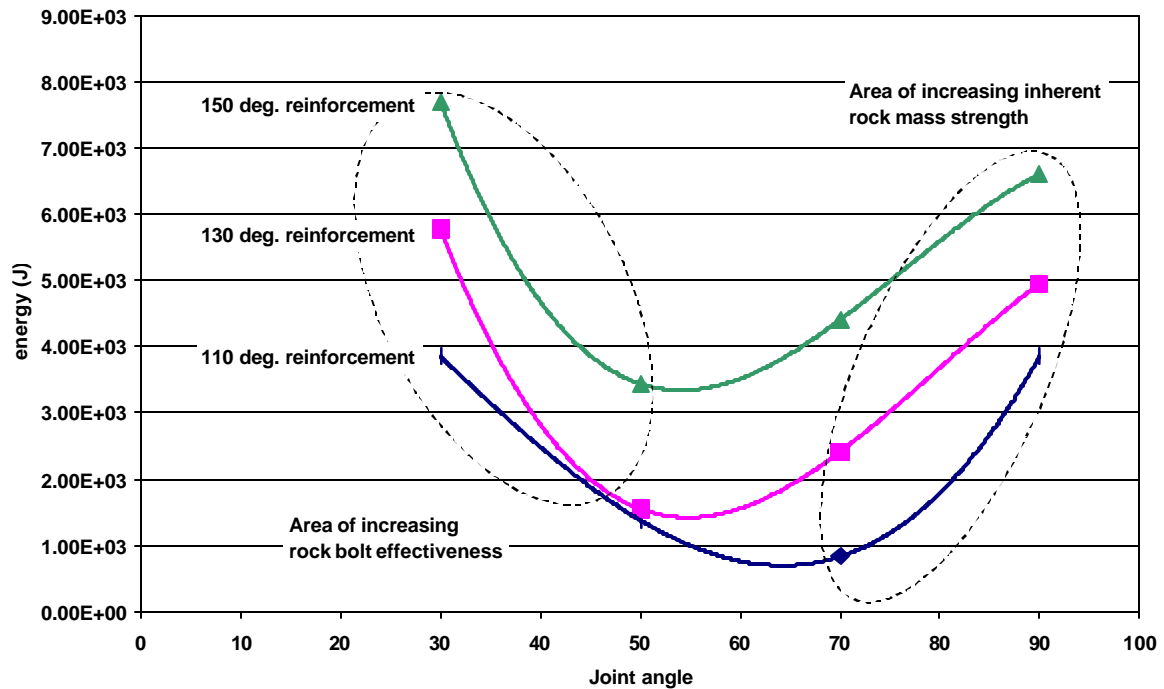


Figure 4.2.8 Influence of fracture angle relative to the stope hangingwall and reinforcement inclination on reinforced rock mass structure capacity.

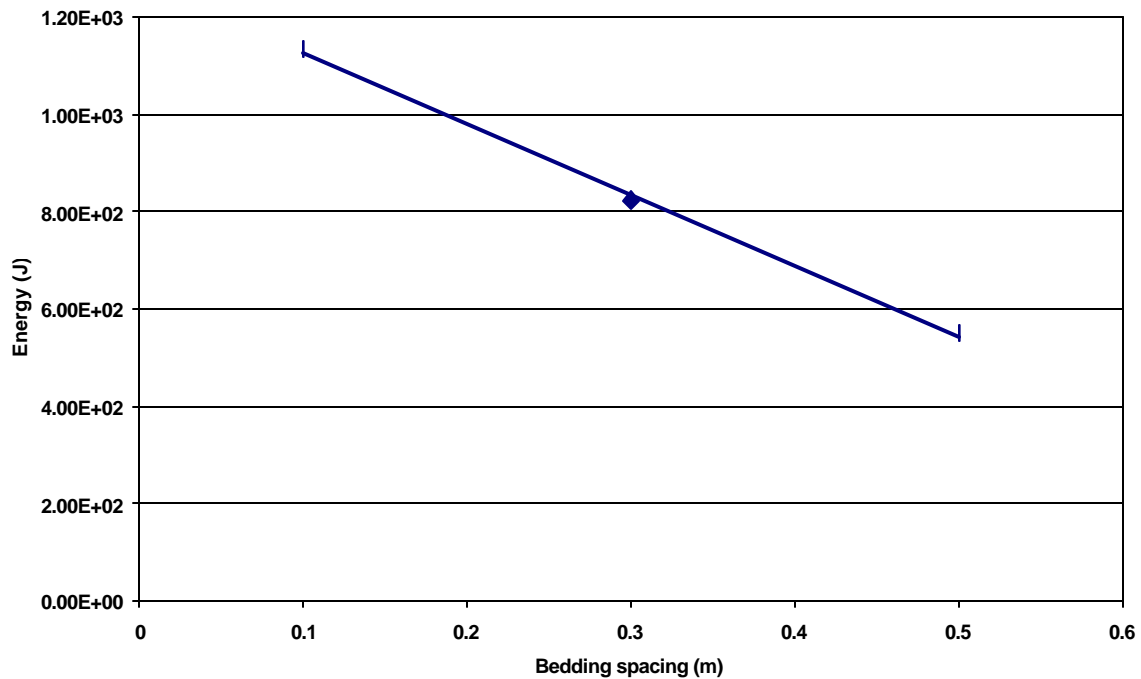


Figure 4.2.9 Influence of sub-horizontal bedding spacing on reinforced rock mass structure (70° fracture dip) capacity.

Figure 4.2.9 illustrates the influence of sub-horizontal bedding on the stability of a reinforced rock mass structure. It is interesting to note that, as the structure of the rock mass becomes more 'discontinuous' due to reduced bedding spacing, the reinforced rock mass system has a greater energy absorption capacity. Intuitively it would be anticipated that under these conditions the inherent rock mass strength would be reduced, rockbolt interaction is more restricted and the overall capacity of the system deteriorates. However, on examination of the load–deformation characteristics of the system, this increased capacity is a result of the substantially greater deformation that the more discontinuous system can sustain prior to localisation of failure. This can be compared to a reduction in rock mass modulus as a function of poorer rock mass quality as captured in empirical rock mass classification systems. However, ultimately the degree of discontinuity of the rock mass resulted in loss of interaction of the rockbolting as a system and thus loss of load bearing capacity of the structure.

A similar mechanism of increased capacity with increased fracture frequency is shown in Figure 4.2.10.

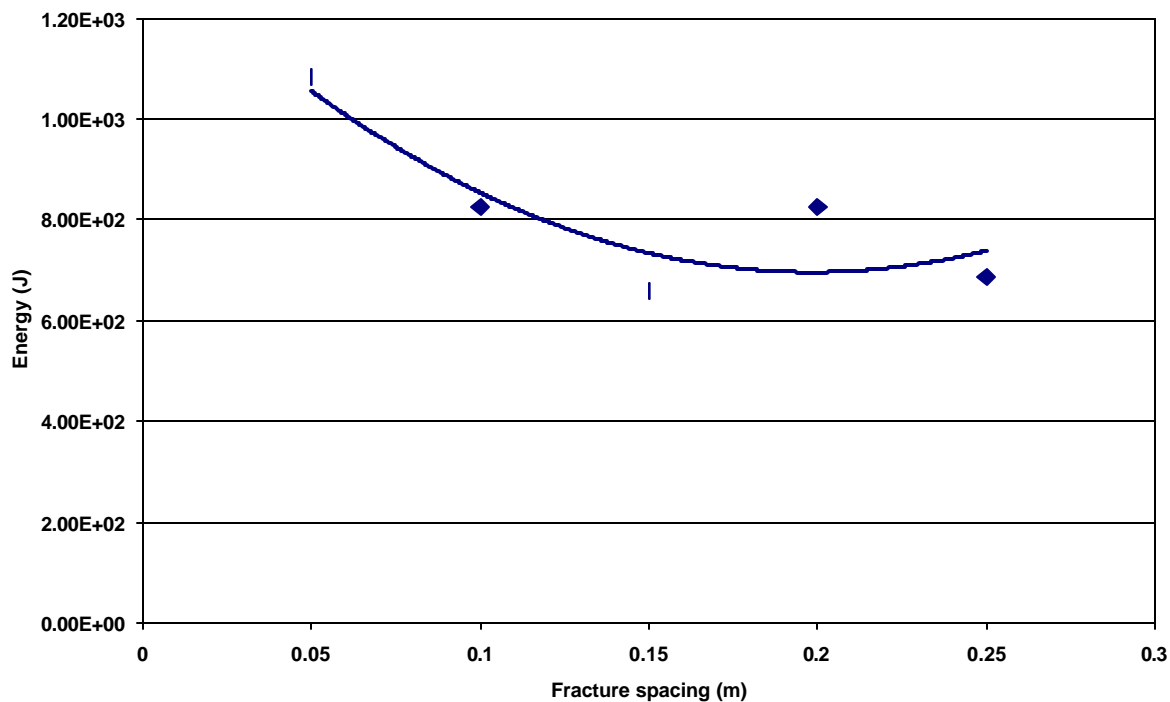


Figure 4.2.10 *Influence of spacing of (70°) fractures on reinforced rock mass structure capacity.*

Again, ultimately there is the tendency for the reinforced hangingwall to break down under conditions of very high discontinuity and also rapidly increase in load bearing capacity with increased general rock mass competency. At a fracture spacing of only 0,35 m (not shown in Figure 4.2.10), there is an order of magnitude increase in the energy absorption capacity of the reinforced hangingwall structure compared to the level indicated in Figure 4.2.10. This is principally due to the increased stiffness of the reinforced rock mass structure.

The increased ability of the rock mass and the reinforcement system to accommodate deformation (shear) within a highly discontinuous rock mass structure is illustrated in Figure 4.2.11 from

observations in tunnels. The capacity of the rockbolt reinforcement system to accommodate this shear deformation was examined in detail in GAP 335 (Haile *et al.*, 1998).



Figure 4.2.11 ***Shear deformation of smooth bar rockbolt.***

Although increasing discontinuity within the rock mass will ultimately weaken the reinforced structure to the extent that failure due to ineffective reinforcement interaction will result, suitable reinforcement within a ‘moderately’ discontinuous medium will allow significant stable deformation. However, a more competent rock mass, with higher load capacity, will exhibit a more brittle type of failure with deformation. Under dynamic loading this may be likened to the relative suitability of stiff or yielding systems. It should be noted that the rock mass structure as modelled in all the above cases would be inherently unstable without rockbolt reinforcement.

The current analysis of the numerical modelling did not allow for the detailed evaluation of the potential for rock mass instability between the rockbolt reinforcement. Although this is an important consideration for operational safety it would however not have affected the relative structural capacity of the reinforcement systems as evaluated in this analysis.

4.2.5 Considerations and conclusions

This preliminary evaluation of the use of rockbolting in the stope face area has indicated that rockbolt reinforcement may have the potential to stabilise discontinuous hangingwall rock mass structures even within the limitations of current drilling and installation lengths. However, current (numerical) analysis has indicated that, although the reinforced rock mass structure has the capacity to absorb dynamic energy, this is of a relatively low level for large spans (4 m in model)

but with a substantial improvement over shorter spans (< 3 m in model). In the majority of simulations the onset of failure of the structure is dominated by persistent sub-vertical discontinuities.

In order to gain an appreciation of the critical design parameters that may influence the capacity of a reinforced hangingwall rock mass structure, a sensitivity analysis based on a 10 % variance of typical design values has been conducted (Figure 4.2.12). It is evident from this analysis that the critical issue for the stability of the reinforced hangingwall is the angle of rockbolt installation in relation to the structure of the rock mass (as reflected by the angle of fracturing relative to the horizontal). The fracture angle could represent a potential geotechnical control on the applicability of rockbolting for slope face area stability. The inclination of the rockbolt reinforcement will influence both the depth of rock mass reinforcement and the mechanism of interaction between the rockbolt and the rock mass.

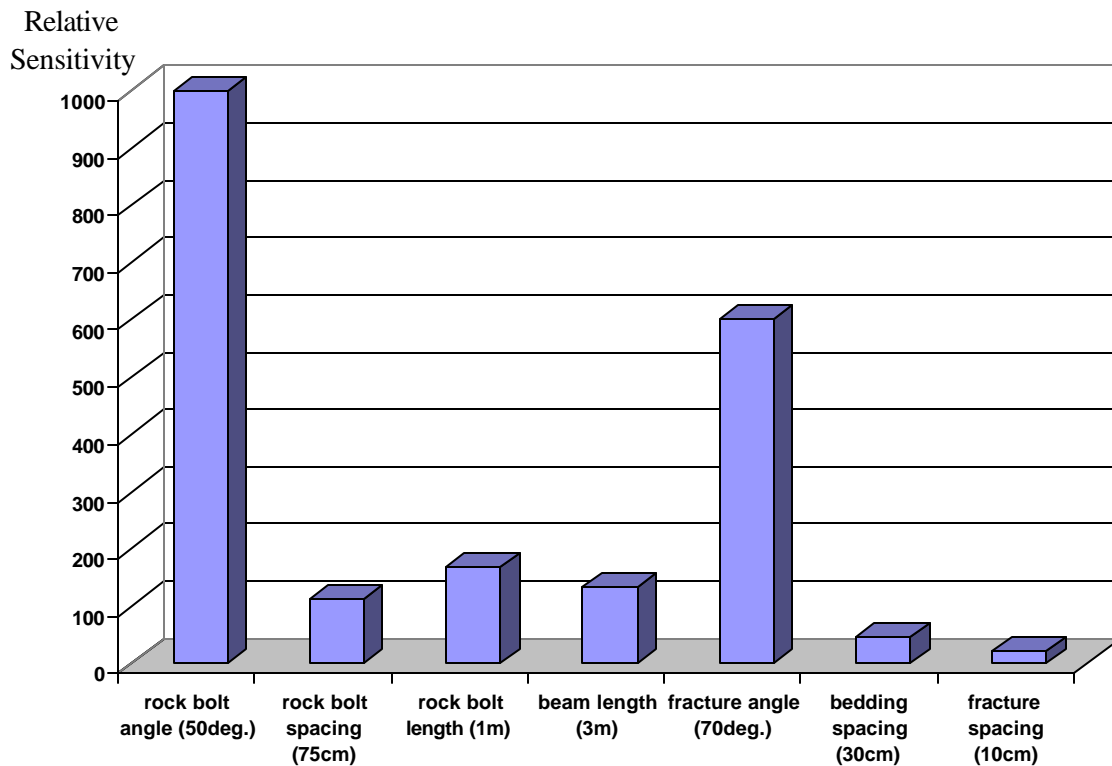


Figure 4.2.12 *Relative sensitivity of reinforced rock mass structure to design variables.*

The importance of the depth of rock mass reinforcement is reiterated by the sensitivity of the model to the length of the rockbolt reinforcement. Other general points of consideration with regard to the use of rockbolting in the slope face area, in addition to the above design discussions, are:

- the estimation of the appropriate mechanism of reinforcement in relation to the depth of rock mass instability;

- the evaluation of mechanisms of direct interaction between the rockbolt and rock mass (e.g. grout encapsulation, end anchor or frictional) on the mechanism of rock mass reinforcement;
- the susceptibility of the above to blasting vibration in the face area and additionally the potential for impact of exposed attachments;
- susceptibility of some rockbolt reinforcement units to installation quality and the consequent inherent risk in the system to variability in installation practice;
- difficulties in communicating to face workers the necessary understanding of rockbolt reinforcement mechanisms;
- the possible additional requirement of surface support and integration with the bolting system;
- assessment of the integration of the rockbolting process into the production cycle, quantification of potential face availability improvement (pre-support of face area prior to blast), reduction in back area support density (if appropriate) and general system economics;
- influence of shearing on bedding; and
- horizontal stress.

4.3 Identification of hangingwall deformation mechanisms and their impact on rockbolting

4.3.1 Introduction

The hangingwall deformation mechanisms were identified and classified by means of underground observations and numerical modelling using the Universal Distinct Element Code, UDEC (Itasca, 1993). Four different areas were identified in which rockbolting is used, as either face area support in conjunction with other permanent support or as the only panel support. The areas are classified according to the potential mechanism of failure of the hangingwall and the rock mass structure (geotechnical classification). The mechanisms of failure of the hangingwall are:

- i) cantilever failure of hangingwall beam,
- ii) deadweight failure of hangingwall beam,
- iii) shear failure at the abutment,
- iv) buckling failure of hangingwall beam due to high horizontal stresses.

These four mechanisms are shown in Figures 4.3.1 to 4.3.4. Although a combination of these mechanisms can occur simultaneously, this scenario is not considered in this study.

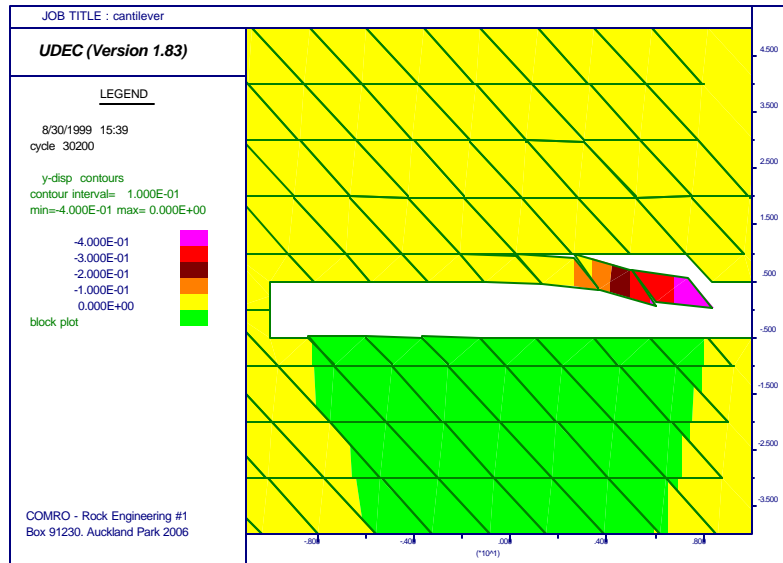


Figure 4.3.1 Cantilever failure of hangingwall beam.

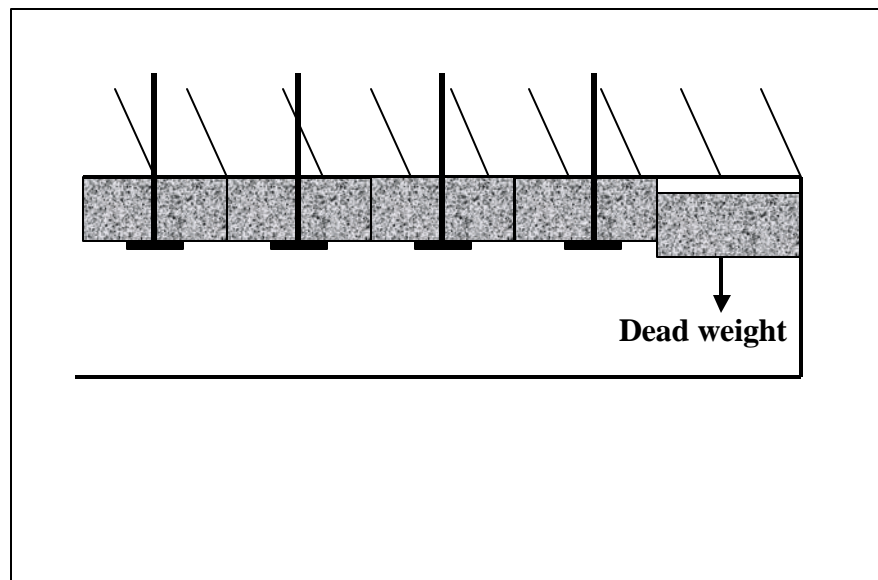


Figure 4.3.2 Gravity induced failure of block in hangingwall.

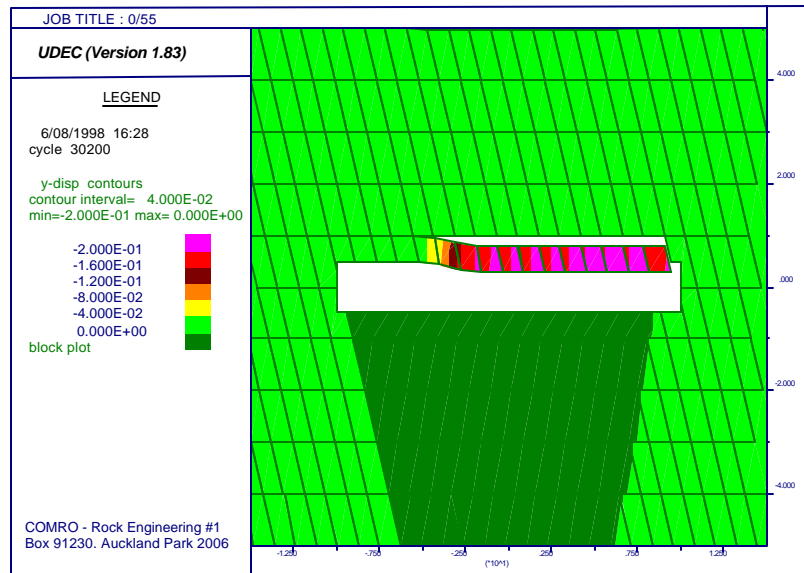


Figure 4.3.3 Shear failure at the abutment.

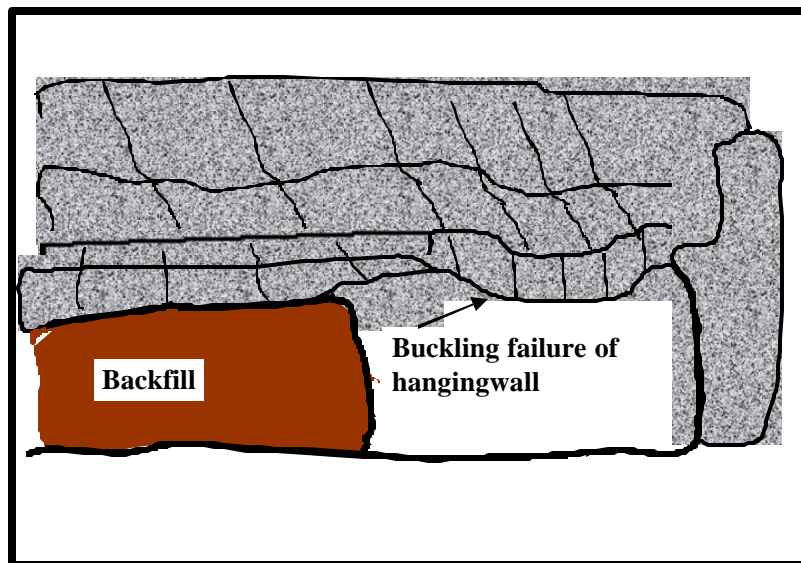


Figure 4.3.4 Buckling failure of hangingwall due to high horizontal stresses.

A rockbolt installed in the hangingwall will either experience a tensile stress or a shear stress due to the deformation mechanisms of the hangingwall (cases presented in Figures 4.3.1 to 4.3.4). The factors that should be taken into account when designing a support system consisting of rockbolts are:

- i) the depth and volume of unstable rock to be supported,
- ii) the maximum span between support units,

- iii) the amount of deformation (shear and axial) that is expected to occur during the mining period,
- iv) the tensile and shear strength of the rockbolt units, and
- v) the shear strength of the grout – rockbolt interface, the grout – rock interface, and the grout.

Consider the following three scenarios:

- i) support of a deadweight that causes a tensile stress on the rockbolt (see Figure 4.3.5),
- ii) supporting a hangingwall consisting of low angle joints or fractures that cause a shear stress in the rockbolt (see Figure 4.3.6), and
- iii) supporting a hangingwall beam with cantilever failure mechanism, induced at the face of the stope, resulting in both an induced shear and tensile stress on the rockbolt due to the moment around the point at which the rockbolt is installed (see Figure 4.3.7).

A graphical representation and a summary of the conditions for stability for each scenario mentioned above is given below.

4.3.2 Effect of deadweight on rockbolt

The case of a rockbolt supporting a dead weight is shown in Figure 4.3.5.

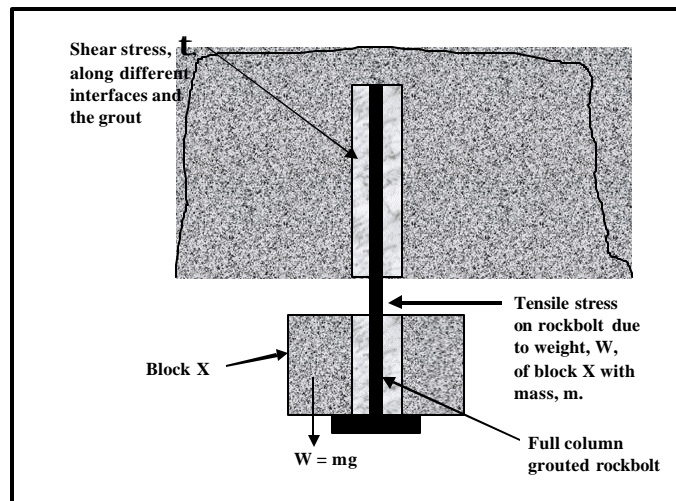


Figure 4.3.5 Deadweight causing a tensile stress in the roofbolt.

The successful suspension of block X shown in Figure 4.3.5 is dependent on the shear strength of the grout, S_g , the shear strength of the grout – rock, S_{gr} , and grout – rockbolt, S_{gb} , interfaces and the tensile strength of the rockbolt, T_b . If the shear strengths of the grout, the different interfaces or the tensile strength of the rockbolt are less than the weight, W , of block X, failure will occur. Thus, the condition for stability can be written as:

$$S_g ; S_{gr} ; S_{gb} > t \quad 4.3.1$$

$$T_b > W (= mg) \quad 4.3.2$$

Where: m is the mass of block X,
 g is the gravitational acceleration, and
 t is the shear stress on the rockbolt, grout and interfaces.

4.3.3 Effect of shear movement on rockbolt

The case of a rockbolt under the influence of a shear stress is shown in Figure 4.3.6.

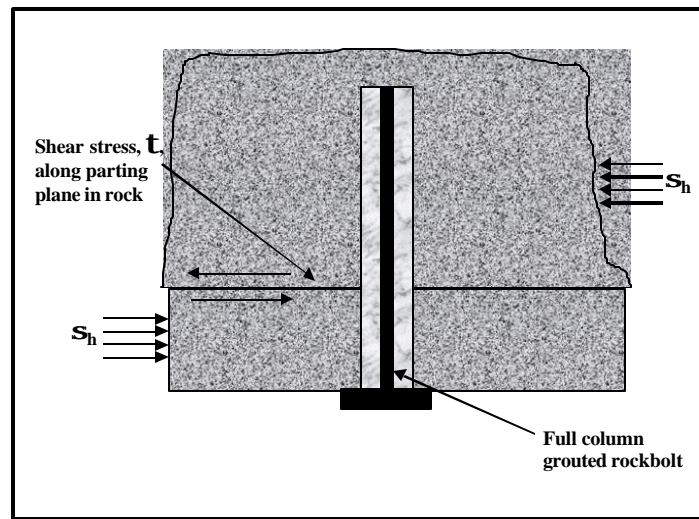


Figure 4.3.6 Shear stress exerted perpendicular to rockbolt, along a parting plane.

The stability of the system in Figure 4.3.6 is dependent on both the shear strength of the grout (S_g) and the rockbolt (S_b). Thus, the condition for stability can be written as:

$$S_g ; S_b > t. \quad 4.3.3$$

Where:

$$S_g = s_n \tan f_g + c_g \quad 4.3.4$$

and s_n is the normal stress in the grout, c_g is the cohesion of the grout and f_g is the internal friction angle of the grout.

4.3.4 Effect of bending moment on rockbolt

Figure 4.3.7 shows the cantilever failure of a block in the hangingwall. The effect of this type of failure on the rockbolt is discussed below.

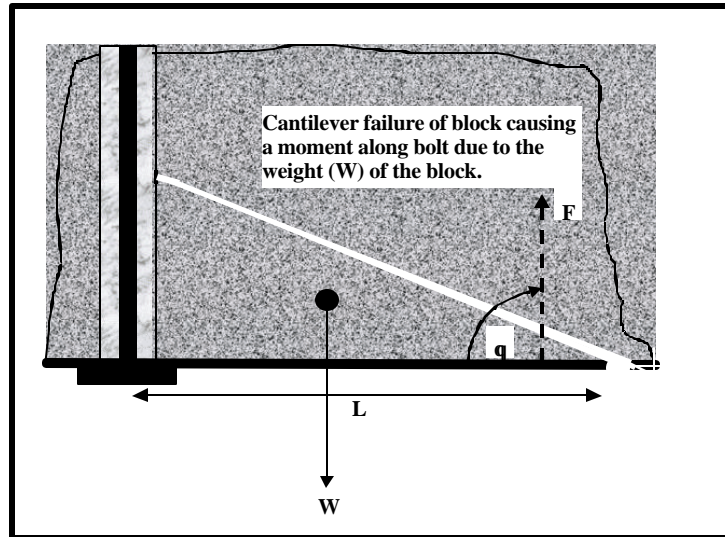


Figure 4.3.7 *Effect of bending moment on the stability of a rockbolt.*

Two approaches can be followed to prevent the type of failure shown in Figure 4.3.7. The first is to preload the bolt such that it does not allow opening of the fracture to occur and the second is to install another bolt to prevent the fracture from opening. The preload on the tendon must be equal or greater than the weight of the rock to prevent opening of the fracture. If the length L is so great that the preload of the tendon is not sufficient to prevent opening, a second tendon can be installed to prevent opening of the fracture.

4.3.5 Determination of support spacing using tributary area theory

4.3.5.1 Introduction

In this section a method for determining the spacing of support units is proposed. The method is based on the tributary area theory.

4.3.5.2 Discussion

Assume that tendons are installed on a rectangular pattern based on the tributary area principle. The volume, V , of rock supported by each tendon is the product of the unstable height or bedding thickness, b , and the tributary area, A , that each tendon is supporting.

$$V = b A \quad 4.3.5$$

The weight, W , of the block is a function of the gravitational acceleration, g , the density, ρ , and the volume, V , of the rock.

$$W = g V r \quad 4.3.6$$

Thus,

$$W = g (b A) r \quad 4.3.7$$

If we assume that the preload, L_p , of the tendon is equal to the weight, W , of the block, then the maximum allowable support spacing can be determined from the following equation.

$$A = L_p / (b g r) \quad 4.3.8$$

This equation was used to plot graphs of support spacing, s , versus the bedding thickness or unstable height, b , as a function of the preload. These graphs are shown in Figure 4.3.8.

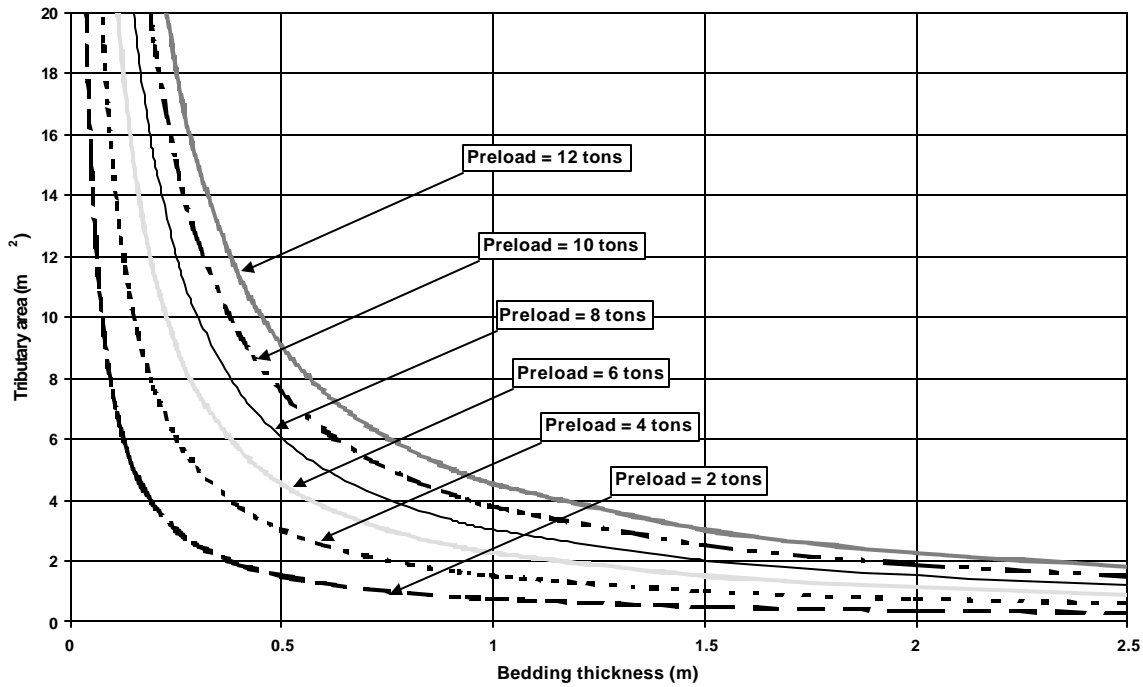


Figure 4.3.8 *Maximum allowable support spacing for different bedding thickness and preload of tendons.*

From Figure 4.3.8 we see that a higher preload and a thinner bed allows a wider spacing of support units. The graphs shown in Figure 4.3.8 are based on the tributary area principle and should only be applied to scenarios where a tendon is supporting a discrete block. This is mostly the case in shallow mining environments.

If we assume that the peak load, L_{max} of a tendon is equal or greater than the block that it is supporting, the same equation can be used to determine the maximum support spacing based on the peak load of tendons. The peak load of the different tendons can be obtained from load-deformation graphs (shown in Figures 4.3.9 and 4.3.10). Substituting the preload, L_p , in Equation 4.3.8 with the peak load, L_{max} , similar graphs to those in Figure 4.3.8 can be drawn. These graphs were drawn for the different tendons (Figure 4.3.9 and Figure 4.3.10) as shown in Figure 4.3.11.

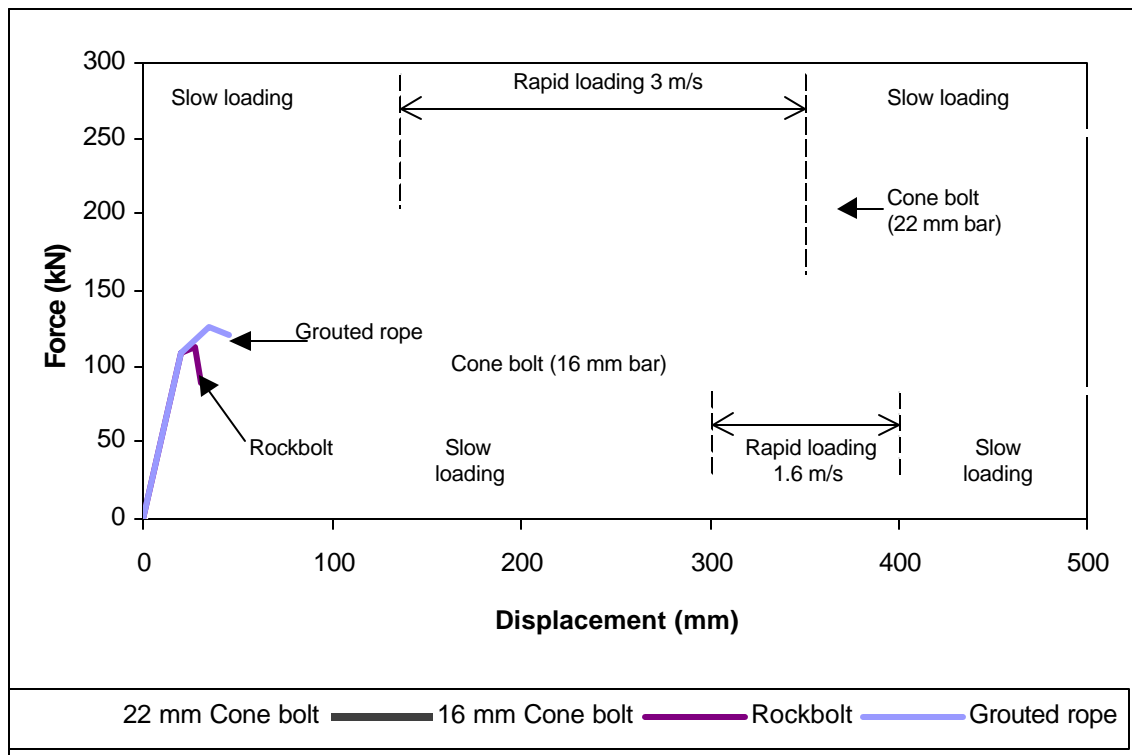
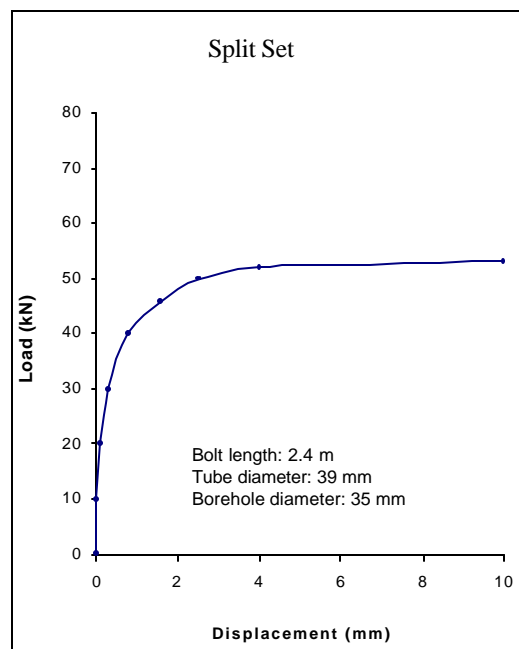


Figure 4.3.9 Load-deformation curves for cone bolts, rockbolts and grouted ropes.



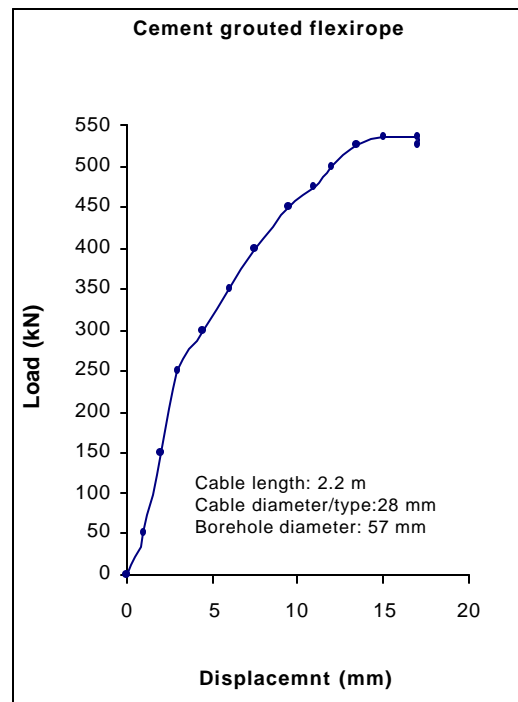
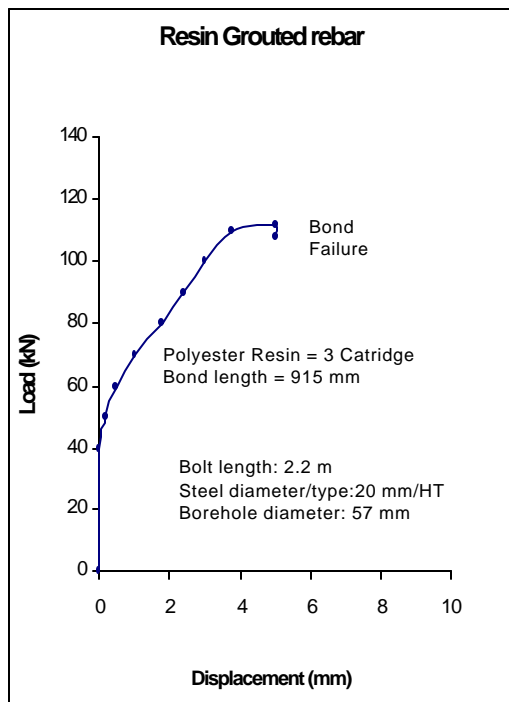
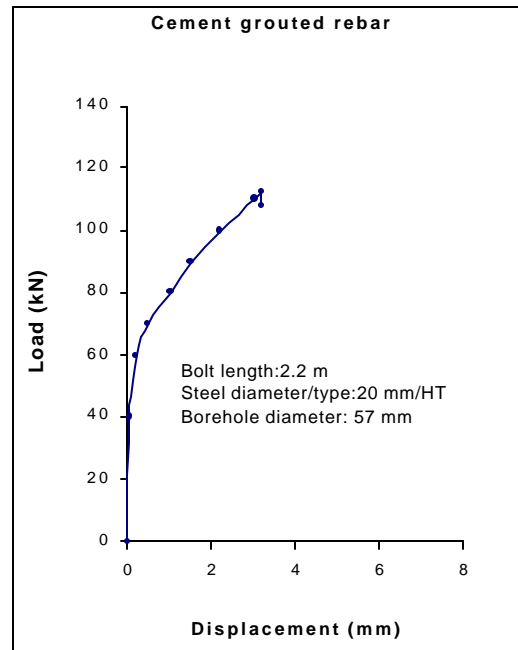
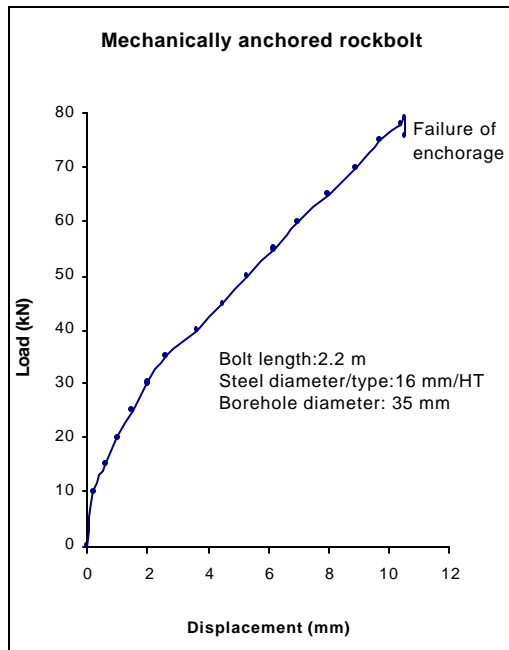


Figure 4.3.10 *Load deformation curves for different tendons (after Stillborg, 1986).*

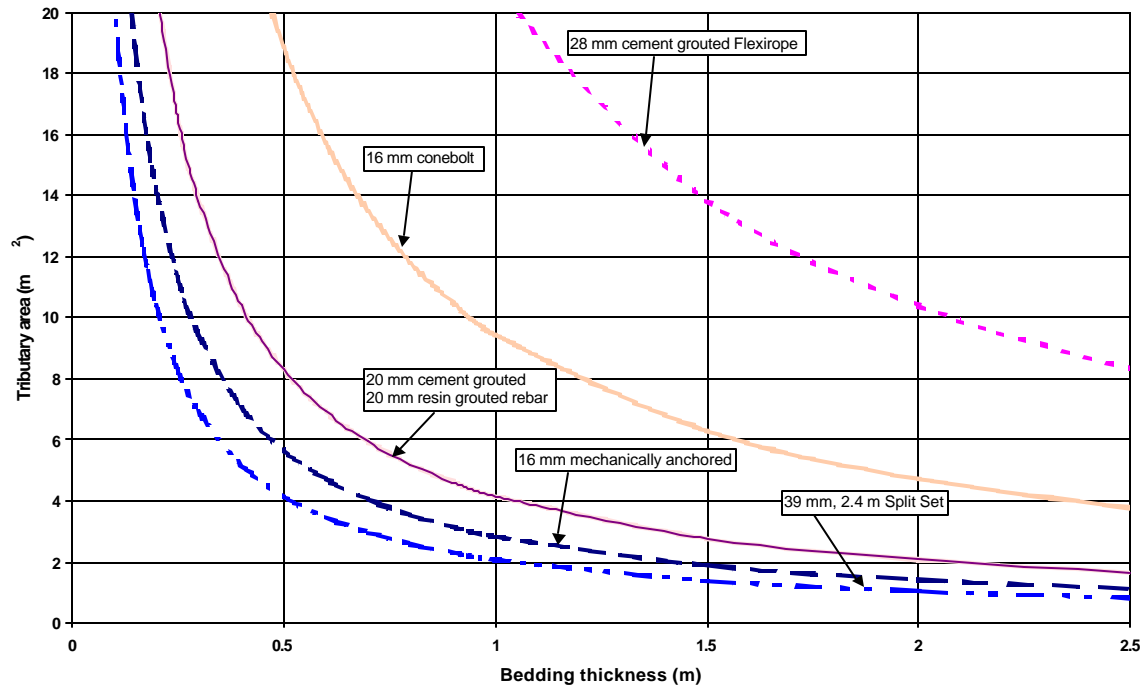


Figure 4.3.11 *Maximum allowable support spacing as a function of different bedding thickness and peak load of tendons.*

From Figure 4.3.11 it can be seen that the Flexirope allows a wider support spacing than the other tendons. This is a function of the peak load of the tendons, which is a function of the diameter of the tendon. The cone bolt requires a closer support spacing than the Flexirope, but its diameter is 16 mm compared to the 28 mm of the Flexirope.

4.3.6 Effect of dynamic loading on rockbolt

Assume for the case shown in Section 4.3.2 that there is a seismic wave that causes movement in the vertical direction. If this wave imposes a downward velocity to the block that is being supported, the total downward force, F_d , will increase. This is a function of the mass, m , of the block and the change in acceleration, a , of the block. This is given by:

$$F_d = ma \quad 4.3.9$$

$$F_d = m [g + (dv/dt)] \quad 4.3.10$$

$$F_d = mg + m (dv/dt) \quad 4.3.11$$

where v is the velocity experienced by the block due to the seismic wave and t is the time period in which the block is excited by the wave.

The load deformation curves of the different tendons can be used to calculate the energy absorption capabilities of the different tendons by calculating the area under the graph. The total energy of a block in the hangingwall of a stope is a combination of the kinetic and potential energy. The kinetic energy is zero if the velocity of the block is zero. Thus, the energy absorption capability of a tendon is given by:

$$E_t = m [(1/2)v^2 + gh] \quad 4.3.12$$

where h is the maximum downward deformation of a tendon, m is the mass of the block that the tendon is supporting, g is the gravitational acceleration and v is the velocity of the block induced by dynamic loading.

Thus, m can be expressed as:

$$m = E_t / [(1/2)v^2 + gh] \quad 4.3.13$$

The mass of the block in the hangingwall is a function of its volume, V , and the density, r , of the rock.

$$m = r V \quad 4.3.14$$

and,

$$V = b A \quad 4.3.15$$

Where b is the bedding plane height and A is the tributary area supported by each tendon.

Therefore,

$$m = r b A \quad 4.3.16$$

Thus,

$$A = m / r b \quad 4.3.17$$

This equation can be used to determine the spacing of the support units as a function of the mass of the blocks in the hangingwall, the density of the rock and the bedding plane thickness. The maximum mass of the block in the hangingwall that a tendon can support can be determined from equation 4.3.13. The energy absorption capability, E_t , and the maximum downward deformation (h) of the tendon can be determined from the load – deformation graphs and the velocities can be measured by geophones.

Using the equations 4.3.13 and 4.3.17, the graphs shown in Figures 4.3.12, 4.3.13 and 4.3.14, were drawn. These graphs were drawn for a block that is subjected to an initial of 3 m/s, 2 m/s and 1 m/s, respectively.

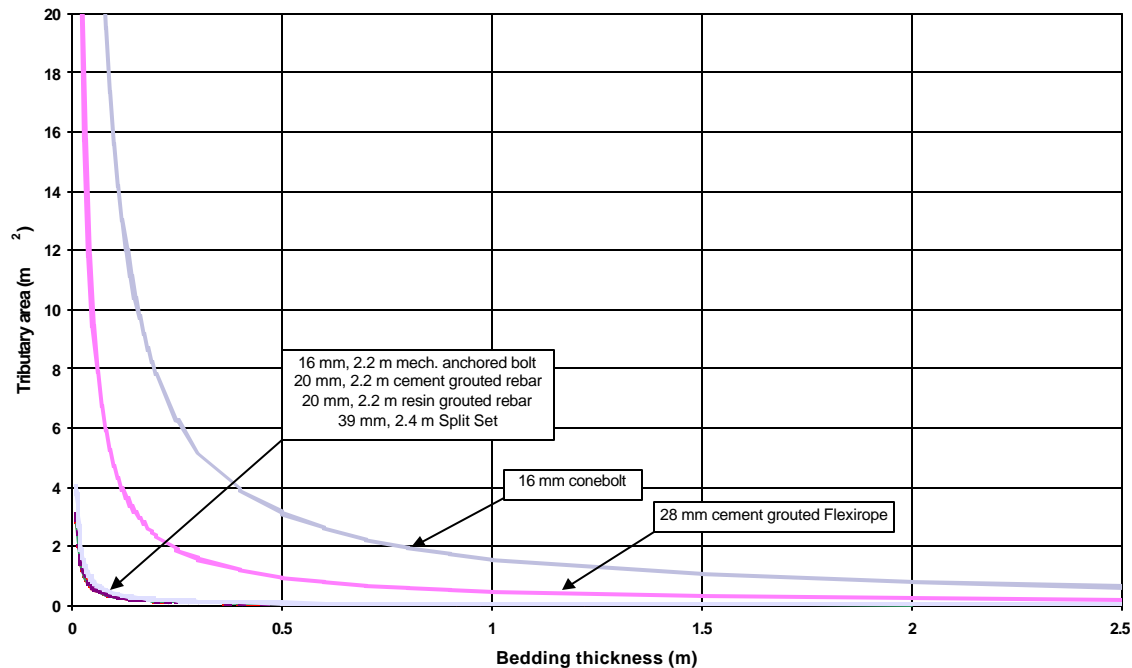


Figure 4.3.12 *Maximum allowable support spacing for a block experiencing a velocity of 3 m/s. The support spacing is a function of the bedding thickness and energy absorption capabilities of the tendons.*

The spacing of the tendons can be obtained from the graphs as a function of the bedding thickness. At a 3 m/s velocity, the cone bolt has the highest energy absorption capability and the Flexirope has the second highest energy absorption capability. The other tendons have similar, and comparatively low, energy absorption capabilities. From this analysis it is apparent that the only tendon-type support systems suitable for use under dynamic conditions are the Conebolt and Flexirope. These systems offer substantial energy absorption capacity and are suitable to as rockburst resistant support.

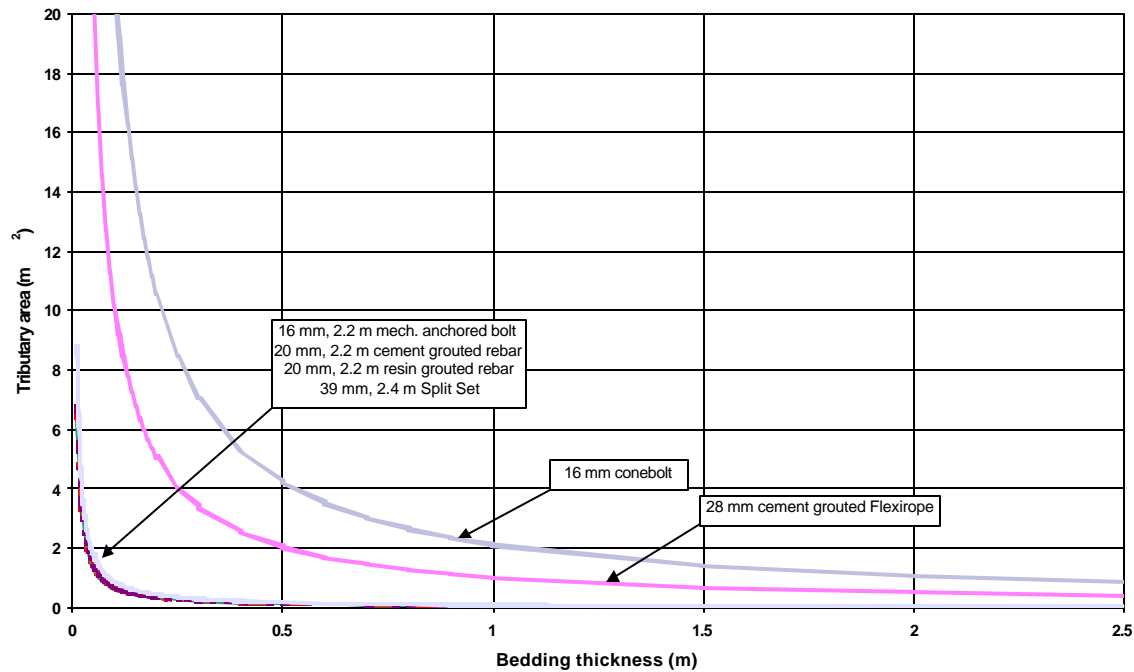


Figure 4.3.13 *Maximum allowable support spacing for a block experiencing a velocity of 2 m/s. The support spacing is a function of the bedding thickness and energy absorption capabilities of the tendons.*

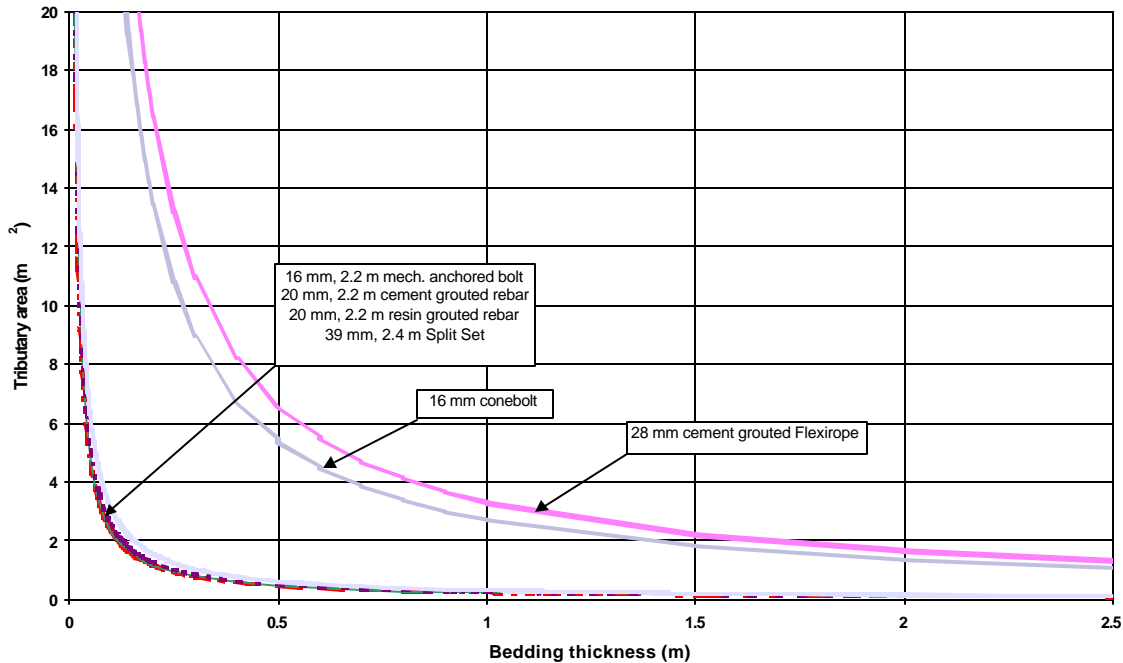


Figure 4.3.14 *Maximum allowable support spacing for a block experiencing a velocity of 1 m/s. The support spacing is a function of the bedding thickness and energy absorption capabilities of the tendons.*

4.4 Zones of influence of rockbolt support units

4.4.1 Introduction

The work presented in Chapter 4.3 is based on previous knowledge of rockbolt support and tributary area theory. This section gives a brief overview of the proposed methods to quantify the zone of influence of a rockbolt, as a function of the rock mass structure. This includes a summary of the work done in SIMRAC Projects GAP 335 (Haile *et al.*, 1998) and GAP 627 (Daehnke *et al.*, 1999).

4.4.2 Review of numerical and analytical methods to quantify zones of support influence

The analysis discussed in this section was done for GAP 335 (Haile *et al.*, 1998) and GAP 627 (Daehnke *et al.*, 1999) and is repeated here for convenience.

4.4.2.1 Review of SIMRAC Project GAP 335 (Haile *et al.*, 1998)

Numerical modelling was used to verify the concept and mechanisms of the interaction of rockbolt reinforcement within a highly discontinuous rock mass structure (Haile *et al.*, 1998). A UDEC (Itasca, 1996) model was utilised and is able to analyse the discontinuous nature of the rock mass structure and to evaluate discrete block stability. An example of the numerical modelling output is shown in Figure 4.4.1 for a simulated blocky, interlocking rock mass structure. The vertical edges of the model represent the location of two rockbolts, which are modelled with properties corresponding to those determined *in situ*, and in this example are anchored into the block at the upper boundary of the model. The lower boundary of the model represents the free surface of the tunnel at the spacing of the rockbolt reinforcement system. The displacement of the blocks is controlled by the loading condition and the assigned discontinuity properties are appropriate for the simulated fracture zone (Haile *et al.*, 1998).

From the modelling results, relationships have been developed between the structure of the rock mass and the relative stability of the reinforced rock mass. In this analysis, it is the structure of the rock mass relative to the orientation of the rockbolt reinforcement that is considered critical. The defined critical discontinuity parameters that govern the rock mass stability are the volume and the shape of the blocks relative to the rockbolt axis, expressed as their aspect ratio in the plane of the analysis.

The relationship between the rock mass structure and the relative stability of the rock mass between the rockbolt reinforcement is shown in Figure 4.4.2. The results are based on the numerical modelling analyses.

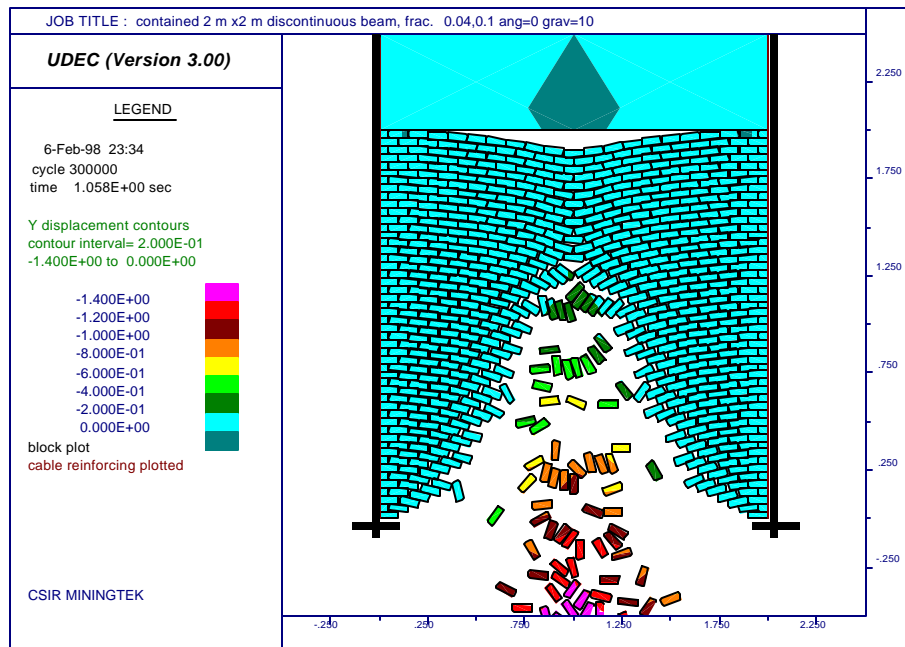


Figure 4.4.1 Example of numerical modelling of rock mass stability between rockbolt reinforcement (after Haile et al., 1998).

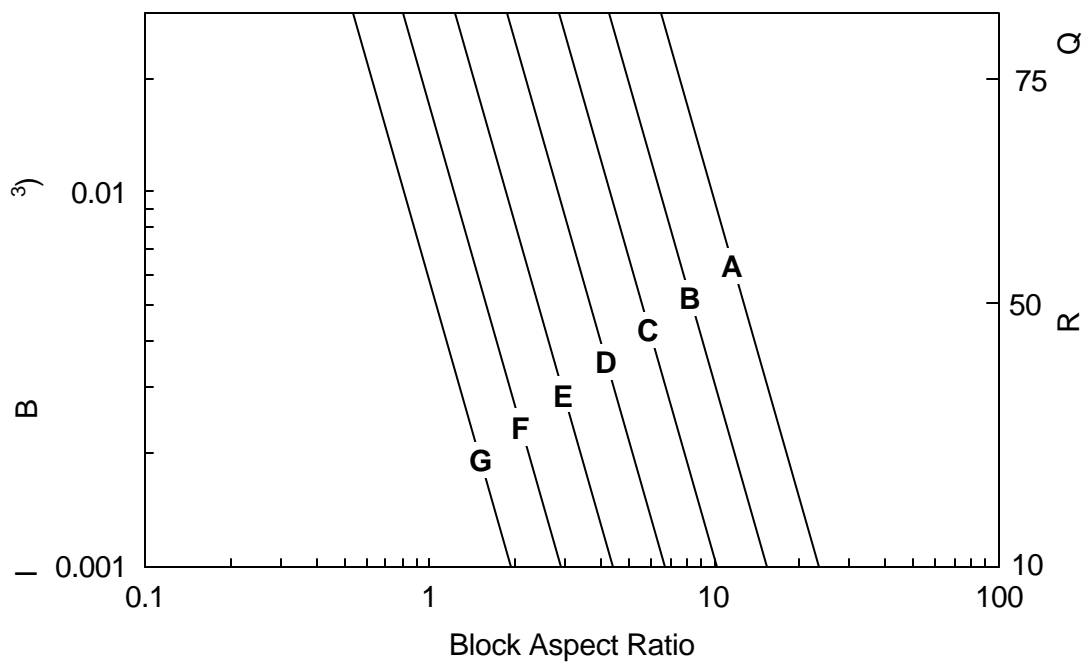


Figure 4.4.2 Chart of relative stability of rock mass structure between rockbolt reinforcement based on numerical modeling (after Haile et al., 1998).

In Figure 4.4.2 the classifications A to G represent the relative stability of the rock mass from relatively stable to unstable, respectively. The classification of a given rock mass structure is based on the block aspect ratio on the y-axis and on the block volume ($0.001 - 0.1 \text{ m}^3$) or RQD ($10 - 90$) on the x-axes (Figure 4.4.2). A given level of stability, as reflected by a rock mass class, may be attained by either increased block volume for a lower aspect ratio or by a high aspect ratio at a reduced volume. The high aspect ratio is comparable to large thin slabs perpendicular to the rockbolt in the sidewall of a tunnel.

The stability of the rock mass between the rockbolt reinforcement will also be a function of the spacing, and, thus, the interaction of the rockbolts within the support system. It would be anticipated that the closer the rockbolt spacing, and, thus, the higher the reinforcement density, the more stable the rock mass between the rockbolts would be. This has been shown from *in situ* observations and from the *in situ* instrumentation of the performance of the overall support system (Haile *et al.*, 1998). The numerical modelling analysis, as illustrated in Figure 4.4.1, was also used to evaluate the influence of the rockbolt reinforcement spacing on the extent of instability between the rockbolts under gravitational loading conditions (Haile, 1998). The results of this analysis are shown in the form of a chart in Figure 4.4.3.

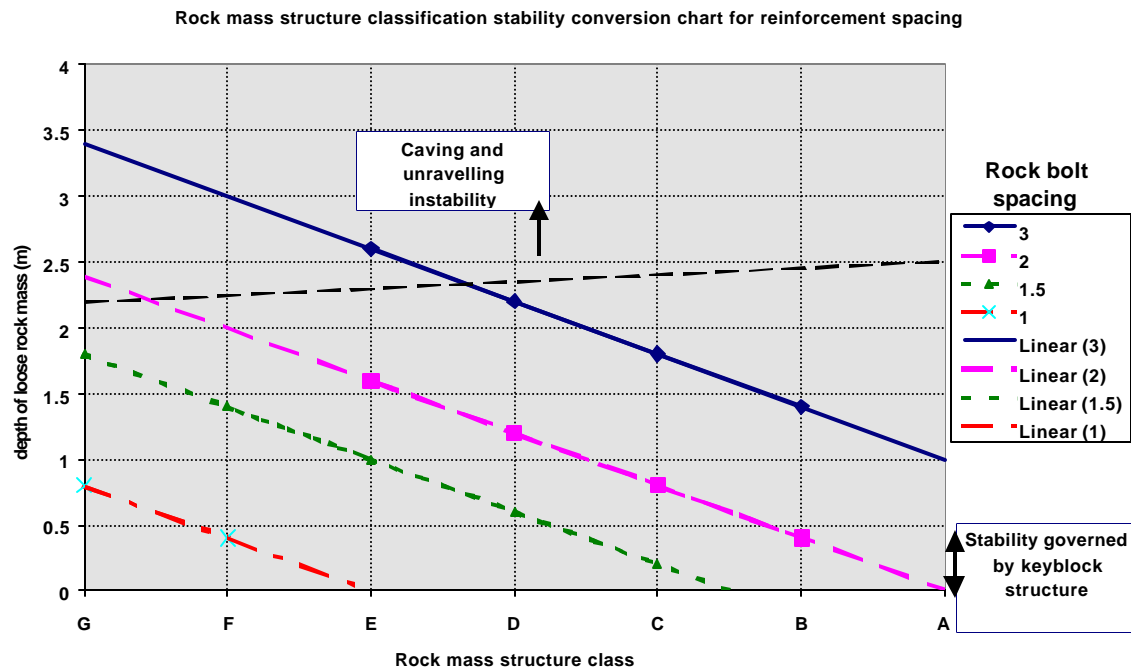


Figure 4.4.3 Chart of the influence of rockbolt spacing, based on rock mass classification as derived from Figure 4.4.2, on depth of instability between the rockbolts (Haile *et al.*, 1998).

The y-axis of the chart in Figure 4.4.3 represents the depth to which anticipated unravelling of the rock mass may occur between the rockbolt reinforcement. Figure 4.4.3 illustrates the tendency for reduced instability of the rock mass with reduced rockbolt spacing and also the increased stability of the rock mass from G to A, i.e. increasing block volume and reducing block aspect ratio.

At high values of unravelling of the rock mass, interaction between the rockbolt units may be completely lost (in the absence of fabric support) and result in total unravelling of the rock mass from around the rockbolts. Where unravelling of the rock mass structure is indicated to be restricted due to a good rock mass class or low support spacing, consideration must still be given to the potential for isolated structural instability of blocks not directly retained by the rockbolt reinforcement.

The chart shown in Figure 4.4.3 illustrates the relationship between the rock mass classification and the rockbolt spacing on the estimated depth of instability based on gravitational loading. In many cases stopes within the deep-level South African mines will also be subjected to loading due to seismic events. This dynamic loading of the rock mass may result in an increased depth of instability around the stope, and also in the increased instability of the rock mass between the rockbolt reinforcement.

By simple geometrical analysis, the volume of the potentially unstable rock mass between the rockbolt reinforcement can now be estimated for a defined rockbolt pattern and loading condition (Haile *et al.*, 1998). Using the data in Figure 4.4.3, a chart to determine the spacing of tendons as a function of the unstable rock between support and the rock mass structure class can be plotted. This chart is shown in Figure 4.4.4 a.

For rockburst conditions Figure 4.4.2 is used to determine the appropriate rock mass class, based on the geometrical parameters of the blocks. Figure 4.4.4 b is then applied to estimate maximum unsupported spans as a function of rock mass class and depth of instability. Figure 4.4.4 b is based on dynamic correction factors established by Haile *et al.* (1998), where the block ejection velocity is assumed to be 3 m/s and the reduced support spacing for dynamic conditions is proportional to the anticipated increase in the depth of instability.

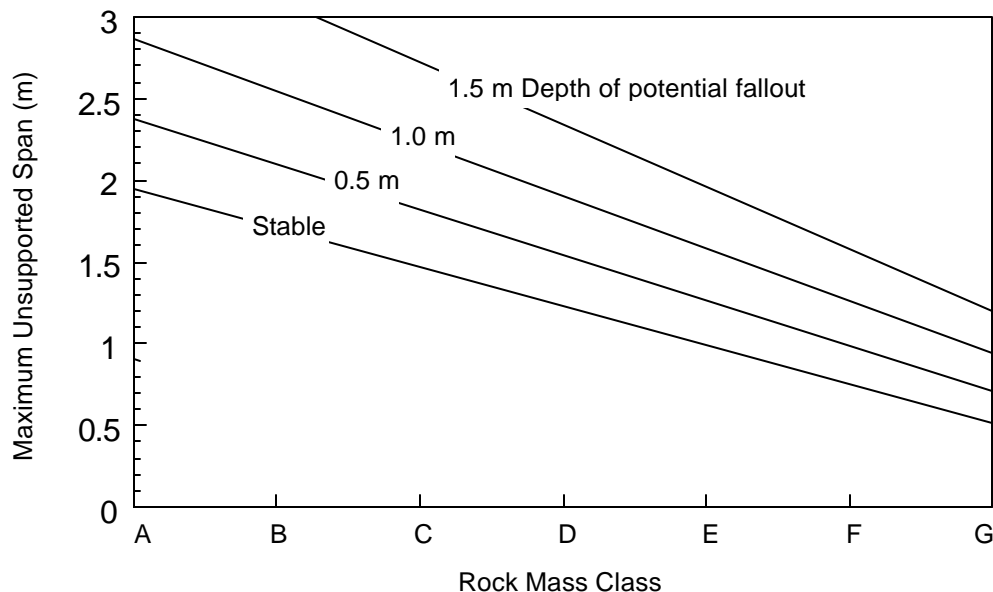


Figure 4.4.4 a *Proposed chart to determine tendon spacing and depth of unstable rock between tendons (rockfall conditions).*

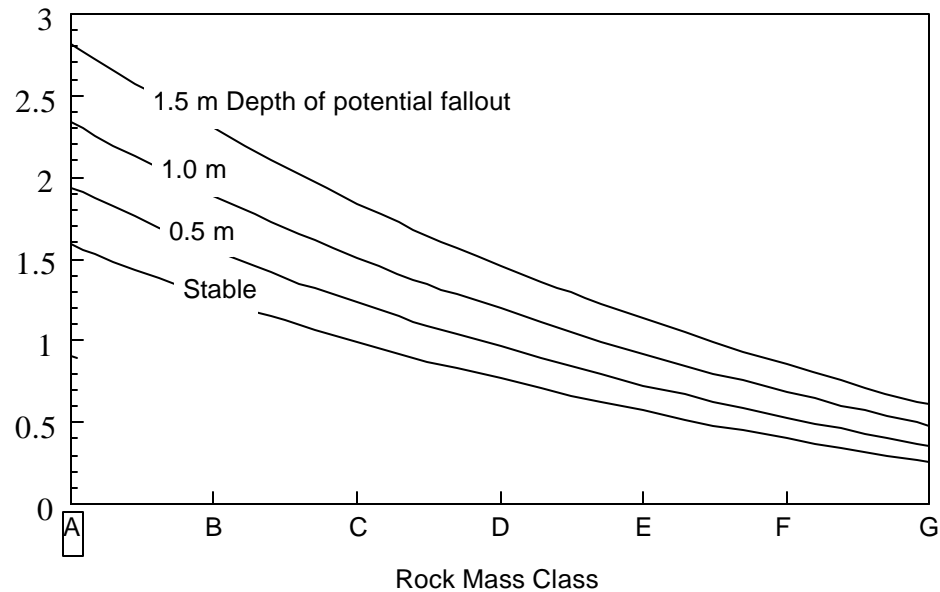


Figure 4.4.4 b *Proposed chart to determine tendon spacing and depth of unstable rock between tendons (rockburst conditions).*

From Figures 4.4.4 a and b we can see that the tendon spacing can be determined if the rock mass structure class is known. Although the graphs are drawn for different depths of unstable rock between the support units, the aim of support design should be to have zero instability.

The approach followed in GAP 335 (Haile *et al.*, 1998) can be used to estimate the zone of support influence and the depth of unstable rock between the rockbolt support units, as a function of the rock mass structure (see design process flowchart given in Figure 4.4.5). The stability of the rock mass is dependent on the type of support used to retain the unstable rock between the rockbolt support units. In tunnels, shotcrete and/or mesh and lacing support is used to stabilize the rock between the supports. In stopes it is recommended that engineering judgement should be applied first to determine whether rockbolt or tendon support should be used or not, secondly, whether areal support is needed or not, and thirdly, which type of areal support should be used. If rockbolts are to be used in very blocky ground conditions, the areal support, e.g. base plates, must be sufficiently large to prevent unravelling between the rockbolts. If the base plates are not large enough to prevent unravelling of the rock, the spacing of the rockbolts can be reduced to decrease the area and depth of potential instability.

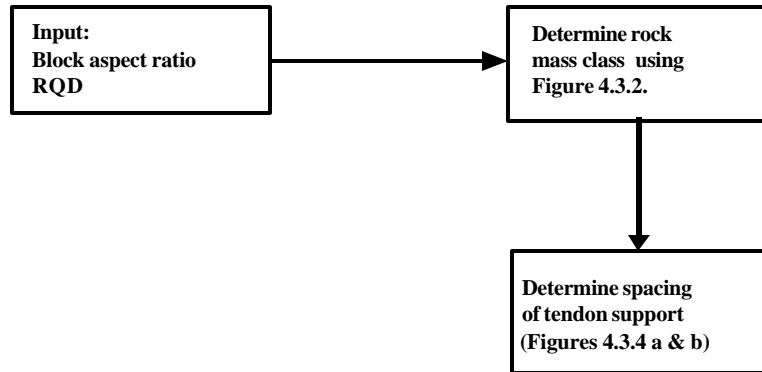


Figure 4.4.5 *Proposed flow chart to determine tendon spacing and depth of unstable rock between tendons based on GAP 335 (after Haile et al., 1998).*

4.4.2.2 Review of SIMRAC Project GAP 627 (Daehnke et al., 1999)

Two-dimensional, plane strain formulation of zones of support influence in a homogeneous hangingwall beam

The simplest zone of influence model is associated with a homogeneous hangingwall beam, i.e. a continuous hangingwall beam not discretised by any discontinuities. The boundary element program UDEC (ITASCA, 1993) was used to model the interaction of a single support unit with a homogeneous hangingwall beam.

For the purposes of this study, it will be shown that the maximum extent of the zone of support influence, z , is governed by the friction angle, ϕ , at the bedding plane interface and the bedding plane height, b . This concept is schematically illustrated in Figure 4.4.6.

When the stress trajectories intercept the bedding plane at an angle exceeding the friction angle, it is assumed that slip occurs at the bedding plane. This is independent of the force generated by the support unit. Slip at the lowest significant bedding plane results in discontinuities (in the hangingwall beam and in the rock mass above the beam) opening, and comparatively little stress can be transferred across the bedding plane interface. This is a conservative assumption, as in reality bedding plane slip might be prevented due to compressive hangingwall stresses and the presence of comparatively large blocks of intact rock situated immediately above the bedding plane. The conservative engineering approach is, however, appropriate, as generally the presence and nature of discontinuities in the rock above the bedding plane are not well known. Hence, in all cases, support design and the interaction of adjacent support units should be based upon the minimum potential zone of influence.

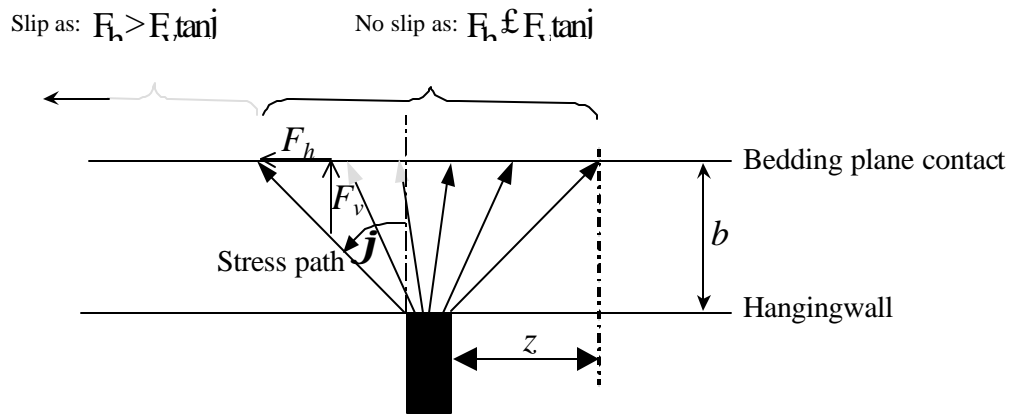


Figure 4.4.6 Maximum extent of the zone of support influence governed by bedding plane friction angle, j , and bedding plane height, b .

Using the simplified model proposed in Figure 4.3.6, it is evident that the zone of support influence extends for a distance of:

$$z = b \tan j \quad (4.4.1)$$

The homogeneous beam model is applicable to shallow mines with comparatively competent and homogeneous hangingwall beams. In intermediate and deep level mines, however, extensive face-parallel mining-induced fractures discretise the hangingwall beam. As a consequence, zones of influence, in the direction normal to the discontinuities, can be of reduced extent. The homogeneous beam model can, however, approximate the zones of influence in the direction parallel to the discontinuities. Numerical models of the homogeneous hangingwall beam are used to quantify the vertical stress profile (induced by the support unit) at the bedding plane interface. Figure 4.4.7 shows the numerically calculated vertical stress distribution at the interface, based on a two-dimensional plane strain model. The normalised support resistance is calculated as the ratio of the vertical stress induced in the hangingwall and the stress transmitted by the support unit. The support resistance is calculated for a support unit $w = 0,5\text{ m}$ wide and carrying a load of $F = 200\text{ kN}$. The friction angle at the interface is assumed to be $j = 40^\circ$. Also shown is a mathematical approximation of the numerically determined profile.

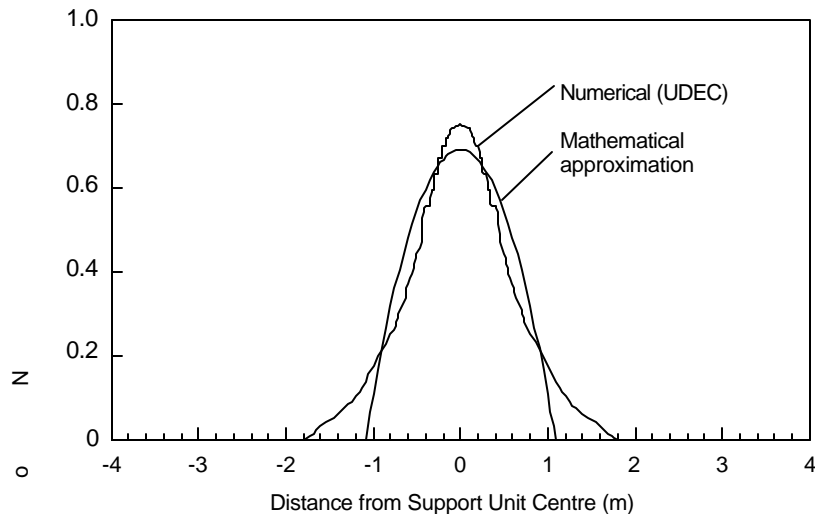


Figure 4.4.7 Numerical versus analytical support resistance profile.

The mathematical function describing the zone of influence stress distribution is in the form of a parabola. The suitability of numerous functions (conical, hyperbolic, Gaussian distribution) was evaluated, and the parabolic distribution was ultimately deemed to be the most appropriate and convenient function to describe stress profiles associated with zones of influence. In two dimensions the stress profile is mathematically described by:

$$s(x) = \begin{cases} 0, & |x| > z \\ \frac{3F}{4z} \left[1 - \left(\frac{x}{z} \right)^2 \right], & |x| \leq z \end{cases} \quad (4.4.2)$$

where: $z = z + r$ for cylindrical support units,
 $z = z + 0,5w$ for rectangular support units,

and, as defined before,

$$z = b \tan \beta . \quad (4.4.3)$$

It is important to ensure that, for all stress profiles,

$$\int_{-z}^z s(x) dx = F , \quad (4.4.4)$$

i.e. the induced stress at the support-hangingwall contact is equal to the total stress within the zone of influence stress profile.

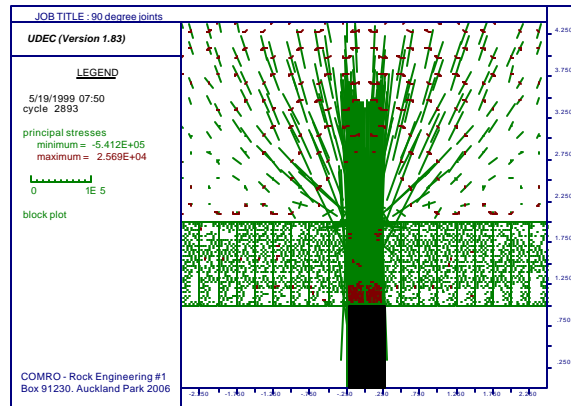
Hangingwall beam discretised by discontinuities

Numerical UDEC models are used to investigate zone of influence profiles in a hangingwall discretised by discontinuities. In intermediate- and deep-level mines, the hangingwall is typically

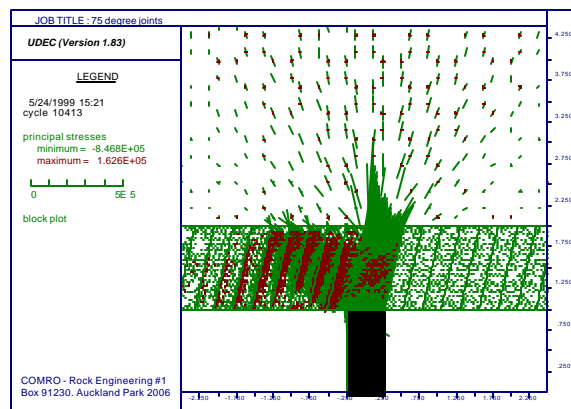
discretised by closely spaced extension fractures. These generally terminate at parting planes and are typically oriented parallel to the stope face.

Figure 4.4.8 shows principal stress vectors as calculated by UDEC for a hangingwall discretised by fractures oriented between 30° and 90° to the hangingwall skin. In these models, no horizontal clamping stresses are applied to the hangingwall beam.

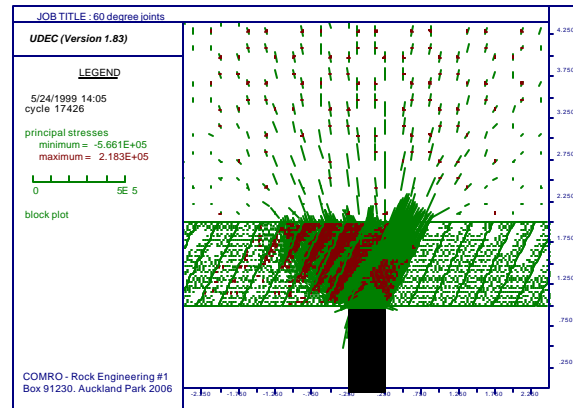
$a = 90^\circ$



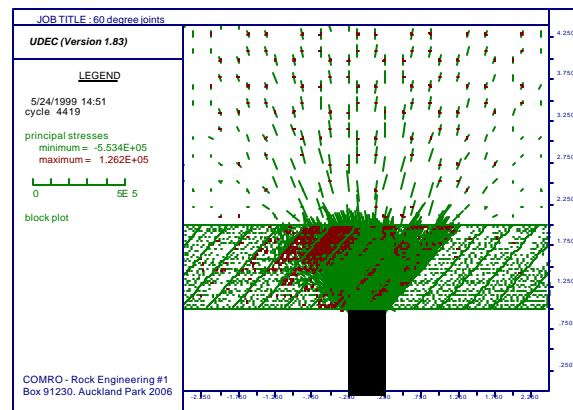
$a = 75^\circ$



$$a = 60^\circ$$



$$a = 45^\circ$$



$$a = 30^\circ$$

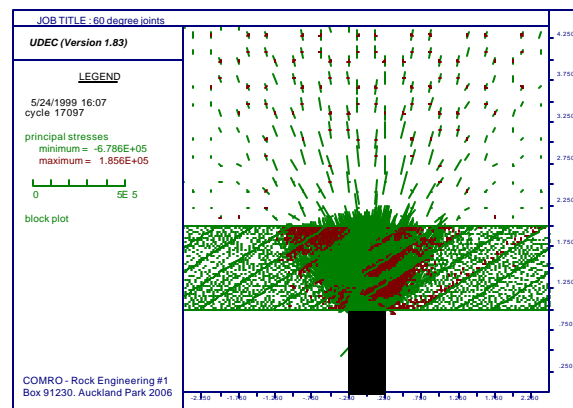


Figure 4.4.8 Principal stress trajectories through a hangingwall beam discretised by 90, 75, 60, 45 and 30 degree extension fractures (UDEC modelling results).

It is apparent that the stress trajectories follow two principal paths, i.e. (i) parallel to the discontinuities, and (ii) perpendicular to the discontinuities. Figure 4.4.9 shows a schematic illustrating the two principal stress paths.

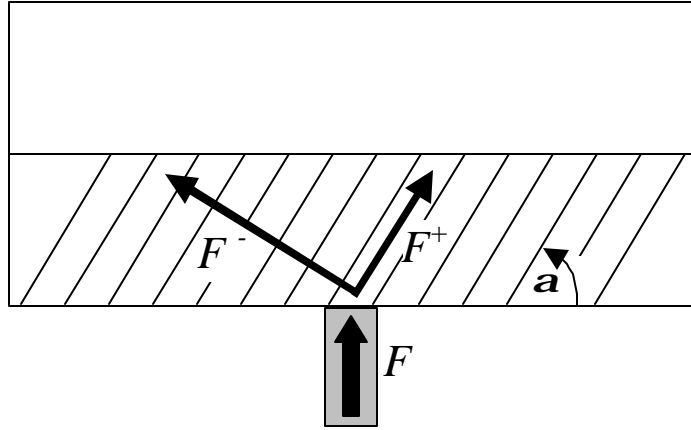


Figure 4.4.9. Stress trajectories through a hangingwall beam discretised by obliquely dipping extension fractures.

The zones on either side of the support unit differ. In an unclamped hangingwall beam, the zones of influence associated with F^+ and F^- are, respectively:

$$z^+ = \frac{b}{\tan a} \quad \text{and} \quad z^- = b \tan j . \quad (4.4.5)$$

The value of z^+ cannot exceed z^- and, if $90^\circ - a > j$, then $z^+ = z^-$.

Solving for the force vectors, it can be shown that,

$$F^+ = F \sin a \quad \text{and} \quad F^- = F \cos a . \quad (4.4.6)$$

The vertical components of forces F^+ and F^- are

$$F_v^+ = F \sin^2 a \quad \text{and} \quad F_v^- = F \cos^2 a . \quad (4.4.7)$$

Thus the ratio of F_v^+ versus F_v^- is equal to $\tan^2 a$. As the fracture angle, a , tends to 90° , F_v^- reduces to zero. The corresponding zone of influence, z^- , needs to be modified accordingly, and when $a = 90^\circ$, $z^- = 0$. In this study, the following correction function is applied to z^- :

$$z^- = b \tan j \frac{100}{(100 + \tan^2 a)} \quad (4.4.8)$$

Figure 4.4.10 shows zone of influence stress profiles for $a = 90^\circ$, 60° and 30° .

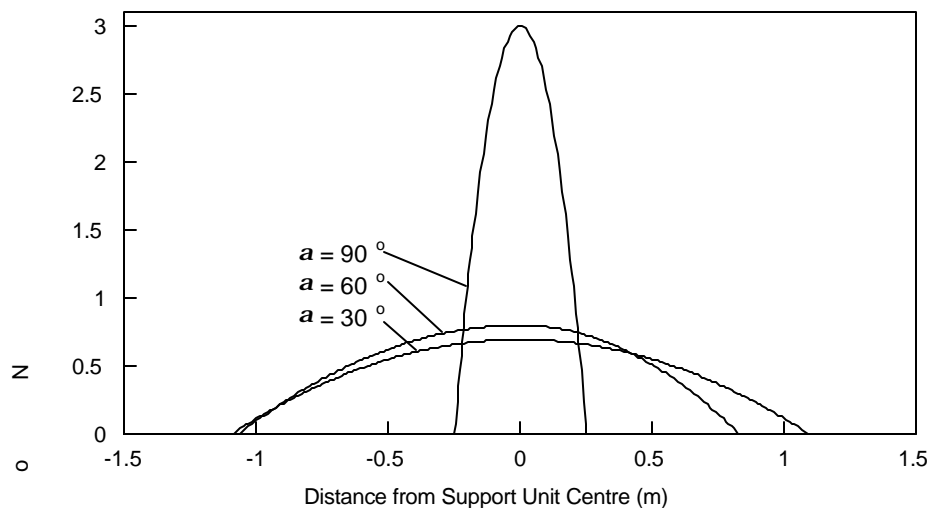


Figure 4.4.10 **Zone of influence profiles for $a = 90^\circ$, 60° and 30° .**

Clamped hangingwall beam discretised by discontinuities

In intermediate- and deep-level mines, fracturing ahead of the stope face induces rock dilation, leading to compressive hangingwall stresses parallel to the skin of the excavation (Jager and Roberts, 1986). Compressive hangingwall stresses usually contribute significantly to the rock mass stability. Squelch (1994) measured maximum compressive hangingwall stresses of 1 to 10 MPa at depths between 0.7 and 2.2 m into the hangingwall. These horizontal stresses clamp the fractured rock together and – depending on the orientation of the fractures – can significantly improve the structural integrity and stability of the hangingwall (Jager and Roberts, 1986).

Herrmann (1987) found that in stopes with back area caving, stress relaxation occurred in the lower layers of the hangingwall, and noted the importance of rock confinement to maintain compressive hangingwall stresses. Rockfalls and caving in the back area generally lead to reduced hangingwall confinement. However, compressive hangingwall stresses can still be maintained when frictional resistance, generated at bedding planes, restricts the lateral hangingwall movement. Such frictional resistance can be induced by appropriate support forces generated under the hangingwall beam (Daehnke *et al.*, 1999).

Compressive hangingwall stresses affect the zone of influence by clamping hangingwall discontinuities together. As a consequence, stresses can be transmitted obliquely across discontinuities, and the zone of influence is extended to either side of the support unit. To quantify the profile and extent of the zone of influence associated with a clamped hangingwall beam, the simplified analytical model shown in Figure 4.4.11 is considered.

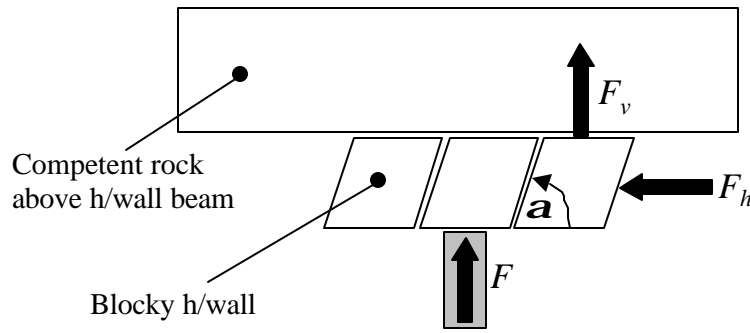


Figure 4.4.11 ***Simplified model used to quantify the zone of support influence in a clamped, discontinuous hangingwall beam.***

By resolving the forces F_h and F_v normal and parallel to the inclined fracture, it can be shown that the maximum vertical force, F_v , that can be transmitted by a hangingwall block, adjacent to the block supported directly by the support unit, is:

$$F_v = F_h \frac{m - \cot a}{1 + m \cot a}, \quad [4.4.9]$$

where $m = \tan f$, and f is the friction angle of the inclined fracture interface. Note that, due to the interlocking nature of *in situ* mining induced fractures, the associated effective friction angle is typically comparatively high, and values of $f = 50^\circ$ to $f = 60^\circ$ are considered realistic. For the two-dimensional plane strain case $F_h = b s_h$. The minimum stress, s_h^{crit} , that is required to clamp the hangingwall discontinuities, is calculated by setting $F_v = F \sin^2 a$ (from Equation 4.4.7), i.e.

$$s_h^{crit} = \frac{F}{b} c \quad \text{and} \quad c = \frac{\sin^2 a (1 + m \cot a)}{m - \cot a}. \quad [4.4.10]$$

If, for example, $b = 1.0$ m, $f = 50^\circ$ and $a = 60^\circ$, then $s_h^{crit} = 2.1 F$. For a typical elongate load of $F = 200$ kN, this implies that the horizontal compressive stresses should be at least $s_h = 0.42$ MPa for the discontinuities to be sufficiently clamped that the zones of influence correspond to the zones in a homogeneous hangingwall beam. This is an important and positive insight, as it implies that in intermediate- and deep-level mines, where typically $s_h > 1.0$ MPa, the zones of influence in a hangingwall discretised by moderately to steeply dipping fractures can generally be accurately approximated by the corresponding zones in homogeneous beams.

Three-dimensional formulation of zones of support influence in a homogeneous hangingwall beam

The three-dimensional formulation of the zone of influence in a homogeneous hangingwall beam follows analogous to the two-dimensional formulation. The zone of influence of stress distribution in a homogeneous hangingwall beam is described by a circular paraboloid, i.e.

$$\mathbf{s}(x, y) = \begin{cases} 0, & \left(\frac{x}{z}\right)^2 + \left(\frac{y}{z}\right)^2 > 1 \\ \frac{2F}{p z^2} \left[1 - \left(\frac{x}{z}\right)^2 - \left(\frac{y}{z}\right)^2 \right], & \left(\frac{x}{z}\right)^2 + \left(\frac{y}{z}\right)^2 \leq 1 \end{cases} \quad (4.4.11)$$

Figure 4.4.12 shows a three-dimensional carpet plot of $\mathbf{s}(x, y)$, where $z = r + b \tan j$.

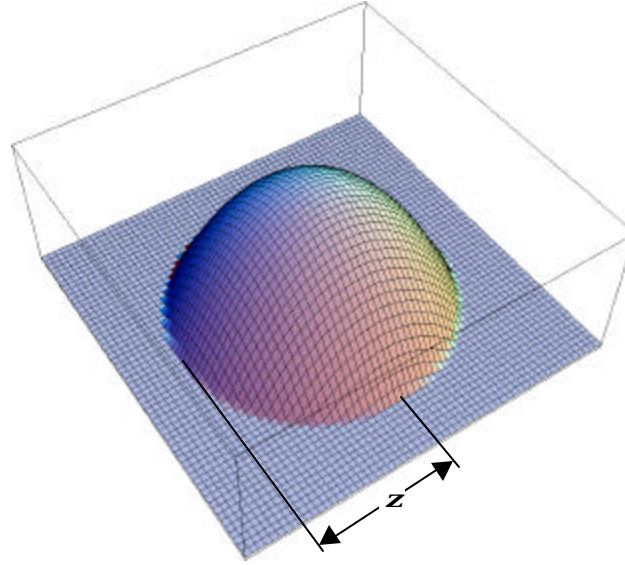


Figure 4.4.12 **Zone of influence within a homogeneous beam in the shape of a circular paraboloid.**

As in the two-dimensional case, it can be shown (Daehnke *et al.*, 1999) that comparatively low hangingwall clamping stresses are required such that the zones of influence in a discontinuous hangingwall beam correspond to the zones of influence within a homogeneous hangingwall beam.

4.4.3 **Applicability of SIMRAC Project GAP 627 results to tendon support**

The results obtained from GAP 627 (Daehnke *et al.*, 1999), were based on either a pack or elongate support unit. In this section of the report, UDEC modelling is used to investigate whether the same approach can be applied to tendon support units. The aim of the analysis is to ascertain whether the stress trajectories follow similar paths for both the tendon support and the elongate or pack support. A similar model to the one that was used in GAP 627 (Daehnke *et al.*, 1999) is applied in this analysis.

Within the UDEC code, the shear and tension characteristics of a rockbolt (tendon) unit are defined by the 'Reinforce' command. This is used to apply reinforcement across all joints intersected along the defined length of reinforcement. The reinforcement function allows for the definition of both axial

and shear stiffness, and capacities of a support unit across a joint (Haile *et al.*, 1998). A force of 100 kN is applied to the rock mass at the position of the rockbolt.

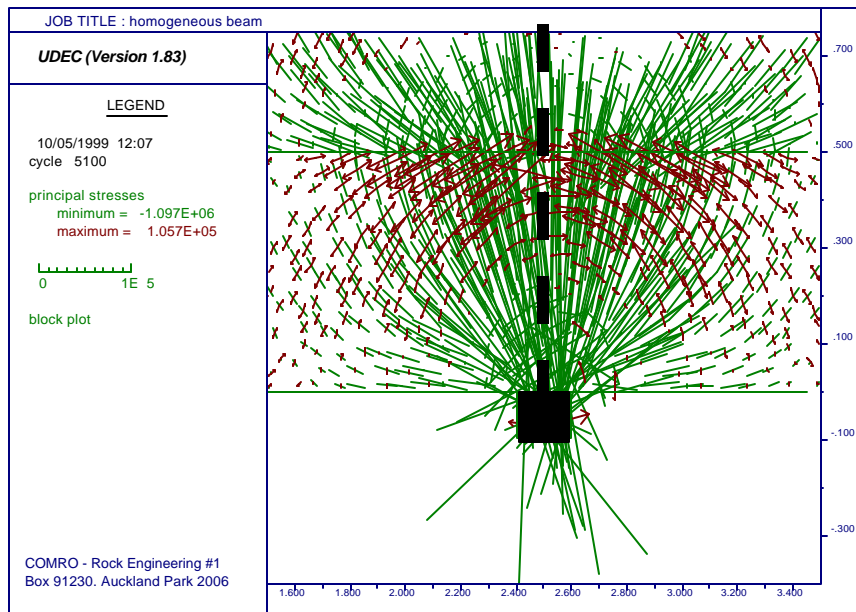
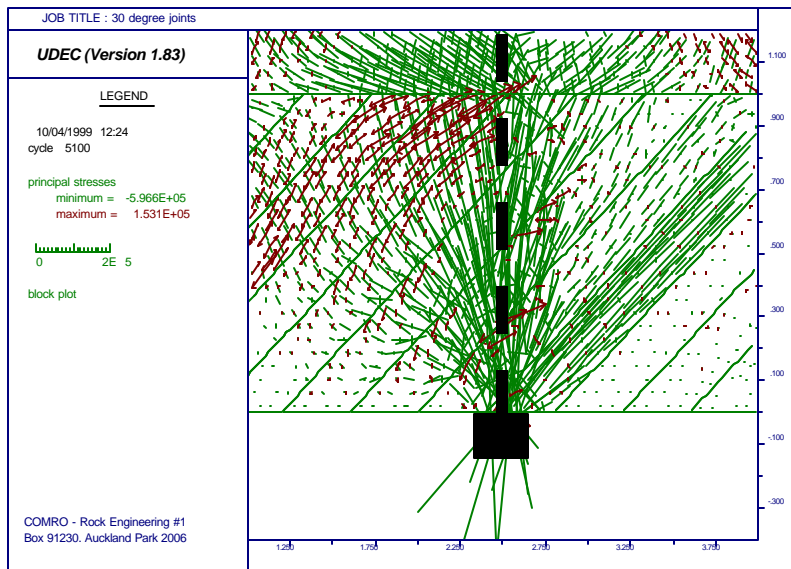
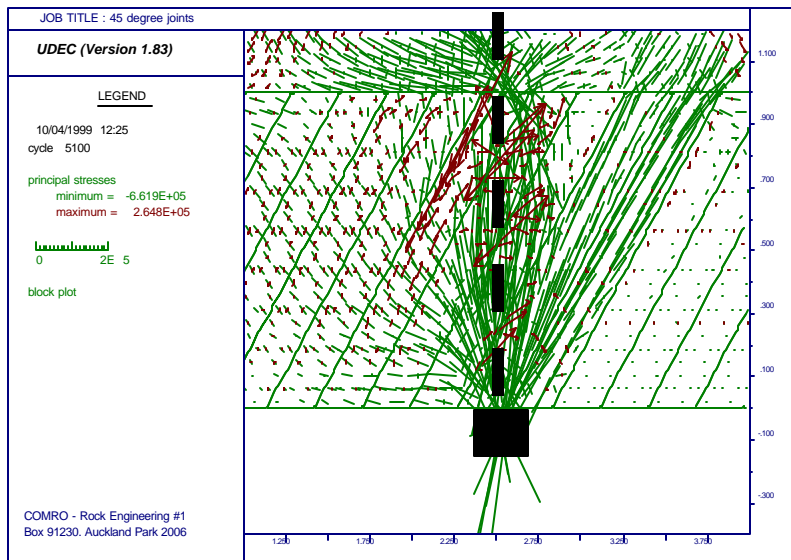


Figure 4.4.13 *Principal stress trajectories through a homogeneous hangingwall beam loaded by a single support unit. ($b = 1,0\text{ m}$, $j = 40^\circ$, $F = 100\text{ kN}$, $w = 0,2\text{ m}$).*

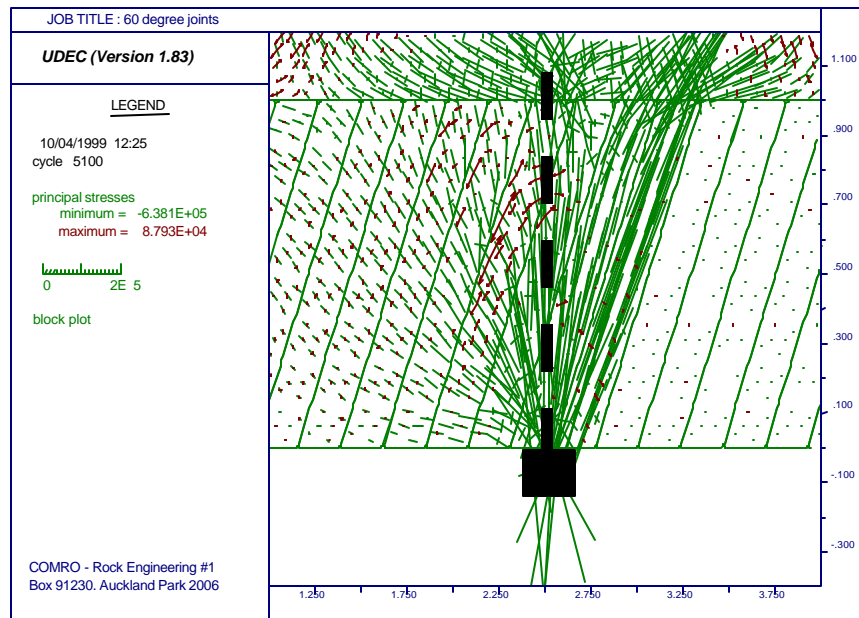
The stress trajectories through the hangingwall beam for the homogeneous case (Figure 4.4.13) and for the beam discretised with different fracture orientations (Figure 4.4.14) are similar for both the elongate and the rockbolt support unit. Thus, the design methodology discussed in Chapter 4.4.2.2 can be applied to rockbolt support as well and the methodology introduced in GAP 627 (Daehnke *et al.*, 1999) can be applied to determine the zone of influence of the rockbolt support units.



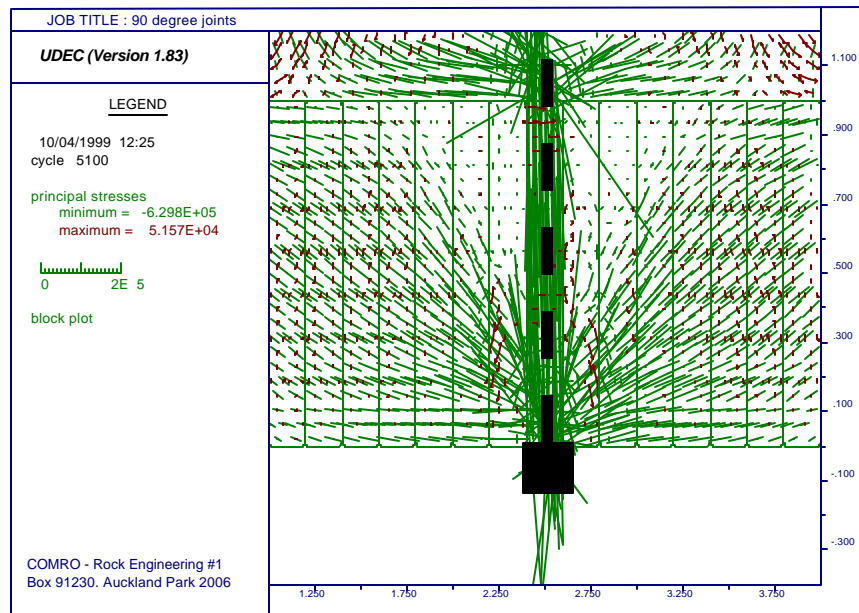
a) 30 degree fractures



b) 45 degree fractures



c) 60° fractures



d) 90° fractures

Figure 4.4.14 *Principal stress trajectories through a hangingwall beam discretised by 90°, 60°, 45° and 30° extension fractures (UDEC modelling results).*

4.5 Quantifying stable hangingwall spans between support units (abstract from GAP 627 (Daehnke *et al.*, 1999), repeated here for convenience)

The qualitative insights gained from numerical simulations are used to develop a simplified conceptual model describing the rock mass stability and quantifying stable spans between adjacent support units. It is believed that the model is suitable to incorporate into a support design procedure, which intends to optimise support spacing, while maintaining an acceptable level of safety.

4.5.1 Hangingwall beam buckling

The design procedure followed here is based on that developed by Evans (1941), and subsequently modified and extended by Beer and Meek (1982), Brady and Brown (1985), and Hutchinson and Diederichs (1996). The solution technique, which is based on the voussoir beam, follows the intuitive idea that, in a discontinuous hangingwall beam, the central transverse crack determines the deformational behaviour (Figure 4.5.1). In the buckling mode the beam becomes unstable to form a 'snap-through' mechanism.

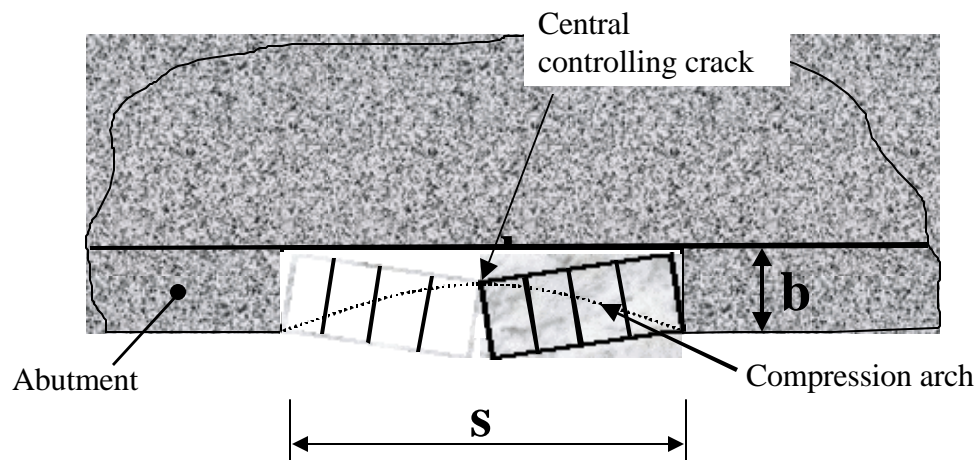


Figure 4.5.1 *Voussoir beam geometry for hangingwall beam analysis.*

In analysing the stability of the voussoir beam the following assumptions are made:

- As the beam deflects, a parabolic compression arch develops in the beam.
- Deflection of the beam occurs before slippage at the abutments. Stability against slippage is determined after the compression arch develops.
- The abutments are stiff, i.e. they do not deform under the arching stress. Each abutment is subjected to the same distributed load as the ends of the beam, however the loaded area is small compared with the beam span. Therefore, elastic compression of the abutments will be small compared with the beam compression, and may be neglected (Brady and Brown¹¹).

The voussoir beam problem is statically indeterminate, i.e. no explicit solution is available and an iterative process is followed to determine the beam equilibrium position. The solution procedure is

given in texts such as Brady and Brown (1985), and Hutchinson and Diederichs (1996), and is not repeated here.

Previously documented results of this solution have used an absolute snap-through limit, which is the limit of stable deflection according to the mathematical formulation. This limit is extremely sensitive to beam thickness, a difficult parameter to estimate accurately and reliably. Hutchinson and Diederichs (1996) recommend a design snap-through limit which is reached when the mid-span deflections reach 10 % of the beam thickness. Beyond this deflection, small differences in thickness have an unacceptably large influence on stability, and the beam's stability becomes uncertain.

Using the design snap-through limit of Hutchinson and Diederichs (1996), the span versus minimum beam thickness is given in Figure 4.5.2. The snap-through limits are given for various values of *in situ* rock mass elasticity modulus (E') parallel to the excavation surface. The *in situ* rock mass modulus is predominantly governed by the stiffness of the rock mass discontinuities, and is lower than the stiffness of solid rock, which is characterised by the Young's modulus. It is apparent from Figure 4.5.2 that the relationship between span and beam thickness is highly dependent on the *in situ* rock mass modulus measured in a direction parallel to the excavation surface.

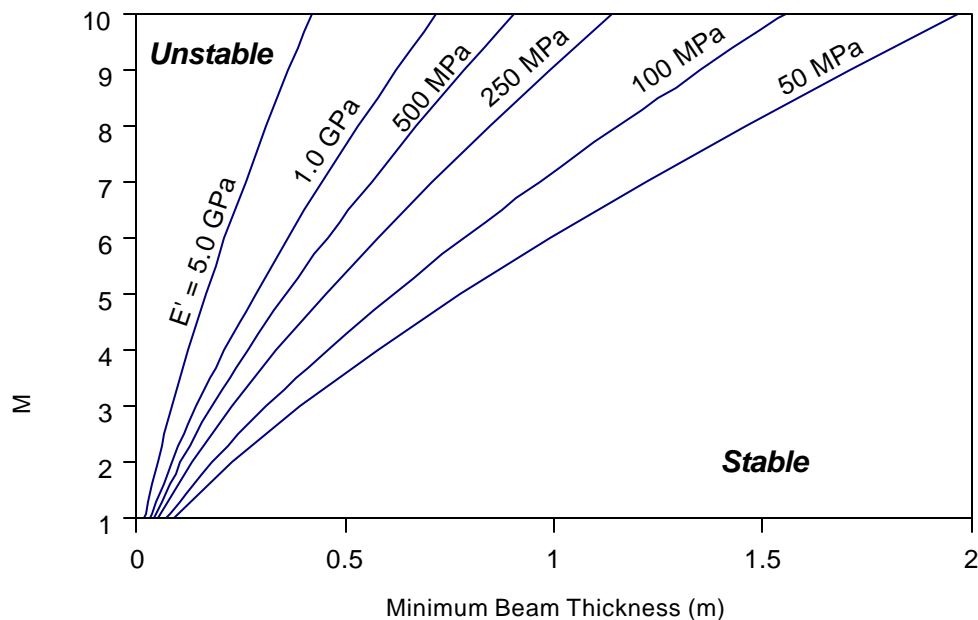


Figure 4.5.2 Span versus minimum beam thickness at 10 % beam deflection for various values of *in situ* rock mass modulus (E').

Bandis *et al.* (1983) made use of experimental data to establish a relationship between normal joint stiffness and normal stress for well interlocked joints in various rock types. The joint stiffness is found to increase with increasing normal stress. For rock mass discontinuities in a typical gold or platinum hangingwall, where the compressive hangingwall stresses are generally less than 5 MPa, a discontinuity stiffness of 40 MPa/mm is assumed for the purposes of this study. It is recognised, however, that further *in situ* discontinuity stiffness measurements are required to obtain more accurate and representative stiffness data.

The joint stiffness is incorporated in the buckling analysis procedure. To simplify the analysis, and in view of the comparatively minor variations in stiffness for normal stresses ranging from 0 to 5 MPa, the stiffness is assumed to be constant. The value selected was 40 MPa/mm, irrespective of the compressive stresses acting within the hangingwall beam.

The effective rock modulus (E') is calculated by multiplying the normal joint stiffness by the lateral deformation (arch shortening) during beam deflection. It is thus assumed that lateral hangingwall deformation occurs at the discontinuities only, and the rock between adjacent discontinuities does not deform. This is a realistic assumption as the Young's modulus of the intact rock is much higher than the effective joint modulus.

Multiple discontinuities act as springs in series, and each discontinuity is compressed equally. Span versus thickness relations shown in Figure 4.5.3 give the stability envelopes of hangingwall beams with three joints, as well as one, three, five and ten joints per metre of hangingwall length.

As shown in Figure 4.5.1, the unsupported hangingwall span needs to be discretised by at least three joints to allow deformation in the buckling mode. Hence, the line shown in the graph of Figure 4.5.3 indicating the stability envelope of a hangingwall discretised by one joint per metre is only shown for maximum stable spans exceeding 3 m. At spans below 3 m the beam would be discretised by less than three joints, and thus no deformation in the buckling mode would be possible.

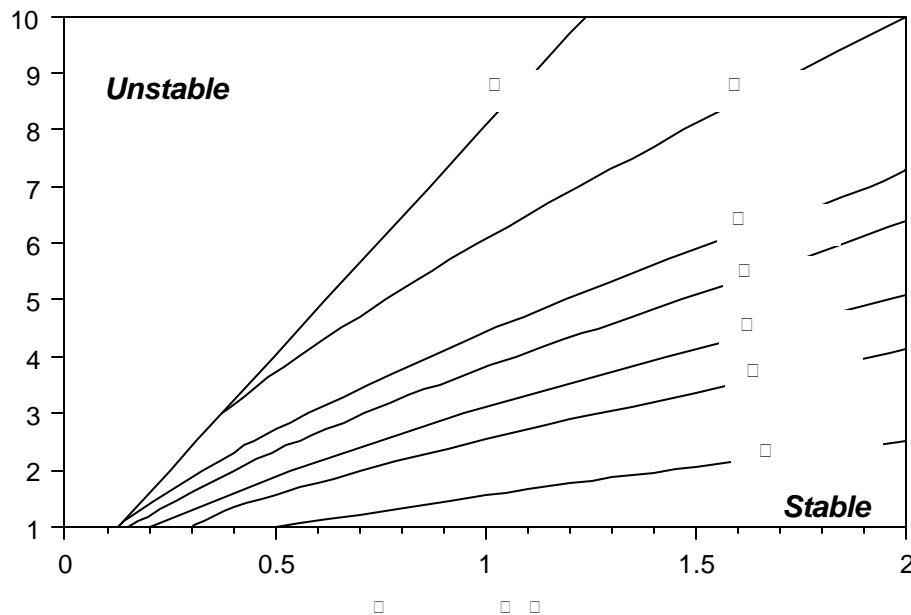


Figure 4.5.3 Buckling stability envelopes of a discontinuous hangingwall beam.

4.5.2 Shear and rotational failure by slip at the abutments

The second failure mechanism considered in this study is shear and rotational failure by slip at the abutments. In Figure 4.5.4 a schematic diagram is depicted of the geometry governing the stability of a hangingwall keyblock. Here shear forces prevent the fall of the block. To analyse this situation in some detail, the following notations are introduced. The weight of the block is denoted by W , the beam thickness by b , the span between adjacent support units by s and s_x is the magnitude of

compressive horizontal stress in the hangingwall. Finally, a and b are the angles that define the orientation of the extension and shear fractures. The hangingwall stress may be generated by two mechanisms, namely:

- In intermediate and deep level mines, the rock dilation associated with fracturing immediately ahead of the stope face may induce compressive stresses parallel to the excavation surface.
- The block rotation associated with the 'snap-through' failure mechanisms may also generate compressive stresses in the hangingwall.

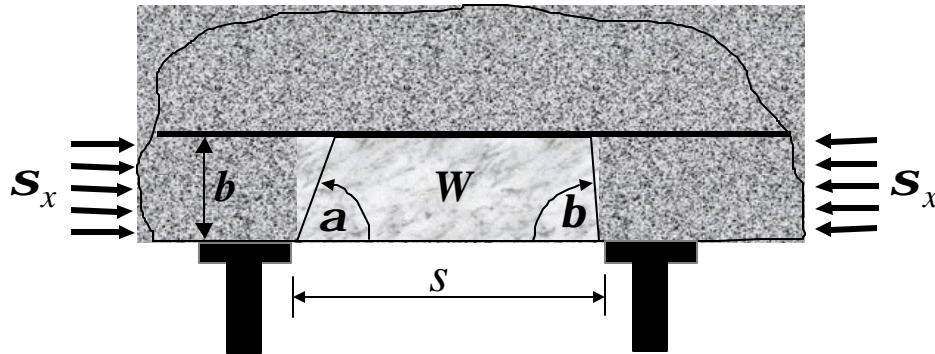


Figure 4.5.4 *Potential keyblock instability due to shear failure at the abutments.*

The discontinuities, which represent mining induced fractures, are assumed to have zero cohesion on the inclined contact surfaces. Hence, for the keyblock to be stable, the lateral thrust at the abutments due to *in situ* compressive hangingwall stresses must mobilise a frictional resistance sufficient to provide the abutment shear force. The frictional resistance for either side of the keyblock can be calculated using the following expressions:

$$V_I = -s_x b \cot(a + j) \quad \text{and} \quad V_{II} = -s_x b \cot(b + j) \quad (4.5.1)$$

The coefficient of friction, m is an important parameter governing the resistance to shear and it defines the angle of friction $j = \arctan(m)$. Typically, underground discontinuities have closely matched surfaces, especially in the case of mining induced fractures. Hence, the apparent friction angle can be relatively high; a range of 30 to 50 degrees is considered realistic.

Stability or instability of the keyblock depends on various factors. The criteria for stability are summarised as follows:

- **Unconditional stability.** The keyblock is unconditionally stable (Figure 4.5.5a) if the forces and moments are both in equilibrium. The forces will not induce the fall of the block if $V_I + V_{II} > W$. Similarly, the moments will not cause dislodging movements (rotation) if the supporting forces satisfy the following inequalities: $V_I > \frac{1}{2}W$ and $V_{II} > \frac{1}{2}W$. Obviously, if the two conditions concerning moments are satisfied, the first criterion will also be fulfilled. A set of necessary and sufficient criteria for unconditional stability can be found from the relationships in Equation 4.5.1 in terms of the angles. The conditions for unconditional stability can now be expressed as follows:

$$\mathbf{a} > \frac{1}{2}\mathbf{p}-\mathbf{j} \text{ and } \mathbf{b} > \frac{1}{2}\mathbf{p}-\mathbf{j} \quad (4.5.2)$$

- *Conditional stability.* If only the criterion concerning forces and *one* of those arising from moments are satisfied, then the block may or may not be stable. To illustrate such a situation, postulate the following:

$$V_I + V_{II} > W; \quad V_I < \frac{1}{2}W; \quad V_{II} > \frac{1}{2}W \quad (4.5.3)$$

Clearly this block is not unconditionally stable, but it may *not* get dislodged if its rotation is *kinematically impossible*. Such a case is illustrated in Figure 4.5.5c. If, however, rotation is possible, failure will occur and the block will fall (Figure 4.5.5d).

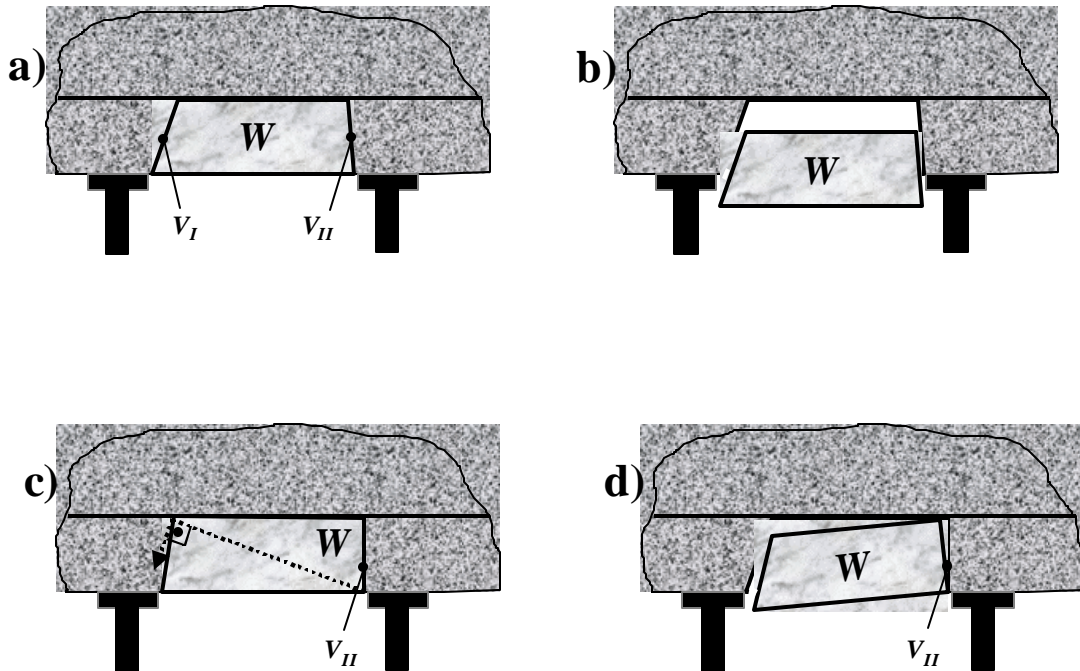


Figure 4.5.5 **Schematic diagrams showing possible failure modes due to shear at discontinuity interfaces.**

- a) **Keyblock is stable as $V_I > \frac{1}{2}W$ and $V_{II} > \frac{1}{2}W$.**
- b) **Keyblock shear failure as $V_I < \frac{1}{2}W$ and $V_{II} < \frac{1}{2}W$.**
- c) **Although $V_I < \frac{1}{2}W$, the keyblock is stable as $V_{II} > \frac{1}{2}W$ and no block rotation is possible.**
- d) **Keyblock is unstable as $V_I < \frac{1}{2}W$ and block rotation is kinematically possible ($V_{II} > \frac{1}{2}W$).**

The next task is to determine the criteria that prevent rotation. As an example, postulate that the block, if it moves, will pivot around its furthestmost hangingwall point on the left (see Figure 4.5.6). Let this point of fulcrum be A. Denote by r the distance between the fulcrum and point B, the furthest point on the right of the top plane of the block. Rotation can occur only if point B can move past the next block to the right.

Let C be the point where the fracture at the right end of the block intersects the hangingwall. Clearly, the limiting geometry is when the block can start to pivot around its fulcrum, that is, around point A. This can occur when the line \overline{BC} (in section) is tangent to the circle of radius r with its centre at point A. If we denote the angle enclosed by lines \overline{AC} and \overline{AB} by e , then this criterion is satisfied if $e + b = \frac{1}{2} p$. Thus if $e + b \leq \frac{1}{2} p$, the keyblock can rotate around its fulcrum and, if $e + b > \frac{1}{2} p$, keyblock rotation is kinematically impossible.

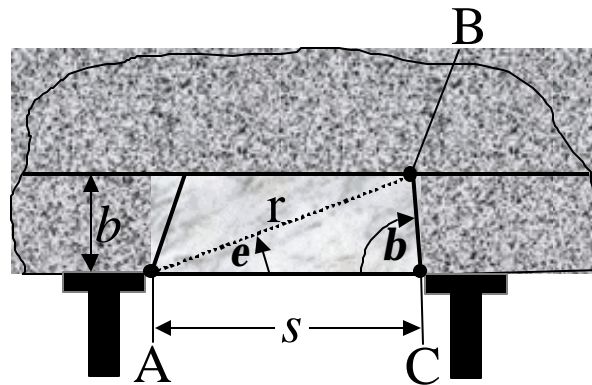


Figure 4.5.6 **Geometry parameters governing the rotational stability of hangingwall blocks.**

The parameters governing the maximum stable hangingwall span are the discontinuity angles (a and b), the fall-out height (b), the friction coefficient (m), and the hangingwall clamping stress (s_x).

The maximum span was determined using the proposed rockfall design methodology for a mine in intermediate depth with five fractures per metre in the hangingwall. Possible failures due to buckling and slip at the discontinuities are analysed. The limiting equilibrium of the keyblock is governed by one of two failure mechanisms: (i) shear failure due to slip at the abutments and/or block rotation, and (ii) buckling failure. Figure 4.5.7 gives stability envelopes for the hangingwall at limiting equilibrium for $s_x = 1,0$ MPa, $b = 1,0$ m and $m = \tan 40^\circ$.

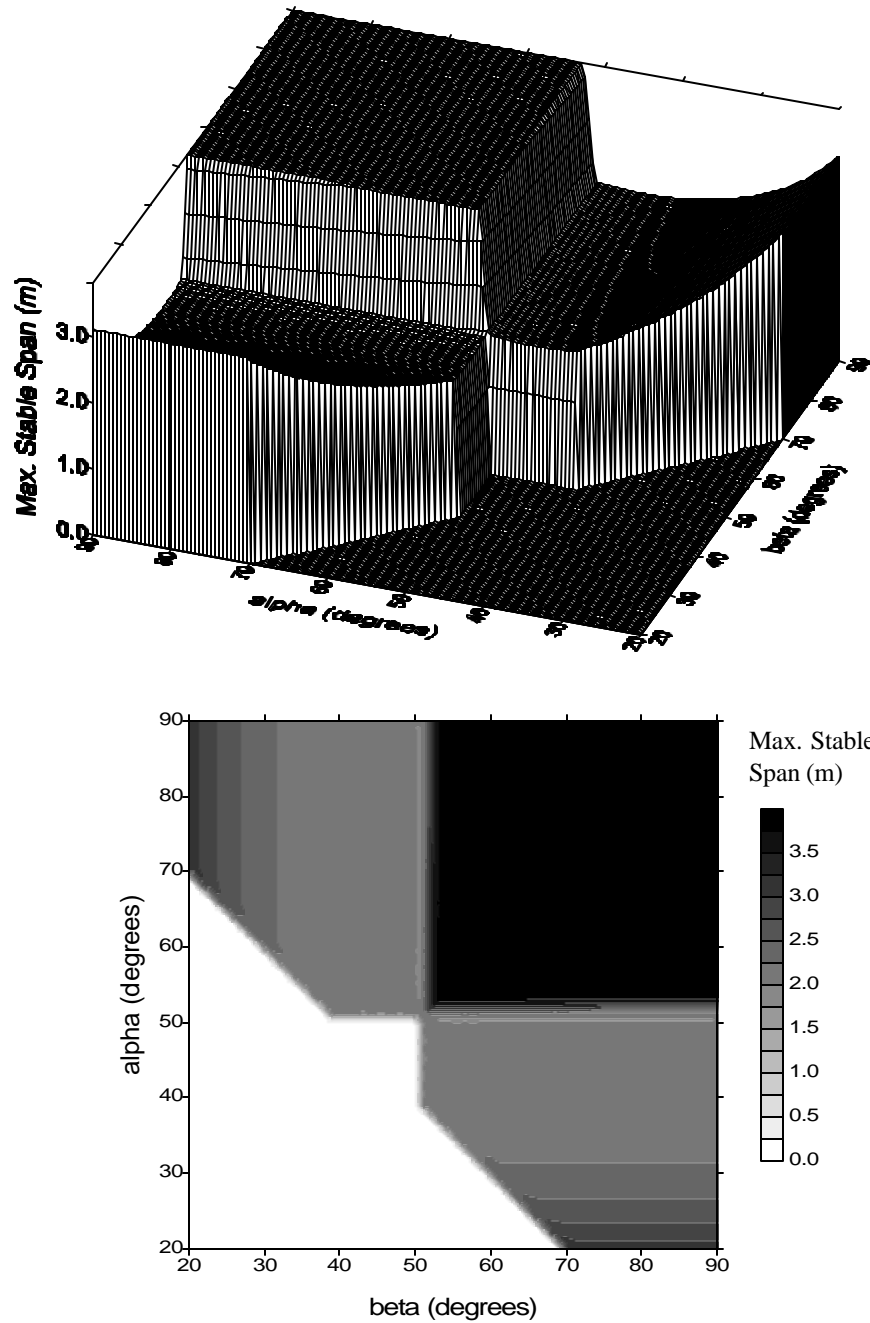


Figure 4.5.7 *Maximum stable span versus discontinuity angles for $S_x = 1.0$ MPa, $b = 1.0$ m and $m = \tan 40^\circ$. Both carpet (top) and contour (bottom) plots are given to facilitate convenient data interpretation.*

As is evident from Figure 4.5.7, the maximum stable span for the case study investigated here varies from zero to 3,8 m. The maximum span is governed by three types of failure mechanisms, which depend on the combinations of discontinuity angles (a and b). A set of stability definitions in the various parts of the a, b plane are illustrated in Figure 4.5.8. The plane is subdivided into four regions and these regions are delineated by inequalities.

- Region A:** This region is defined by $0 < a \leq a_{\min}$ and $0 < b \leq b_{\min}$, where $a_{\min} = b_{\min} = \frac{1}{2} p - j$. Hence, for the example given here ($j = 40^\circ$), $a_{\min} = b_{\min} = 50^\circ$. At angles $0 < a \leq a_{\min}$ and $0 < b \leq b_{\min}$, the supporting forces V_I and V_{II} are negative, and hence all keyblocks, irrespective of size, are *unstable*. This is evident from Figure 4.5.7, which also show that for $0 < a \leq a_{\min}$ and $0 < b \leq b_{\min}$ the maximum stable span is zero.
- Region B:** Here the limits are defined by $a_{\min} < a \leq \frac{1}{2} p$ and $0 < b \leq b_{\min}$. Thus $V_I \geq 0$, $V_{II} < 0$ and the keyblock is conditionally stable, depending on whether keyblock rotation is kinematically possible. It was shown that it is kinematically impossible for a keyblock to rotate if $b/s \geq 1/2 \sin(2b)$ (Daehnke *et al.*, 1999). For keyblocks with a short span the stability condition to prevent rotation becomes $a + b > \frac{1}{2} p$. Hence, in Region B, keyblocks rotate and are unstable if $a + b \leq \frac{1}{2} p$ (see Figures 4.5.7 and 4.5.8).
- Region C:** Here the boundaries are given by the following inequalities $0 < a \leq a_{\min}$ and $b_{\min} < b \leq \frac{1}{2} p$. For these angles $V_I < 0$, $V_{II} \geq 0$ and the keyblock is conditionally stable, depending on whether rotation is kinematically possible. The conditions outlined for Region B are also applicable to Region C, and are thus not repeated here.
- Region D:** This region is delineated by $a_{\min} < a \leq \frac{1}{2} p$ and $b_{\min} < b \leq \frac{1}{2} p$. Here $V_I \geq 0$, $V_{II} \geq 0$ and comparatively large spans are stable. The upper limit of the stable spans are governed by the buckling potential of the beam. Figure 4.5.8 gives the maximum stable spans versus beam thickness for a hangingwall discretised by various numbers of joints. For the case study shown in Figure 4.5.8 ($b = 1$ m, 5 Joints/m), the maximum stable span governed by the buckling potential is 3,8 m.

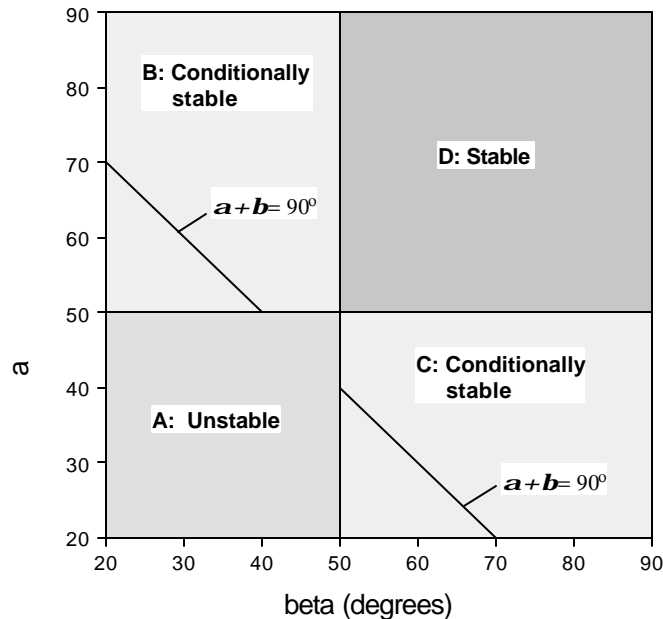


Figure 4.5.8 Stability definitions in the various parts of the a, b plane.

4.6 Rockbolt support design

4.6.1 Proposed rockbolt design guidelines for end anchoring

Flow charts are proposed to design support taking into account the effect of dead weight, shear movement and bending. The effect of shear failure and cantilever failure is treated separately, but a flow chart to account for each of these mechanisms independently, is given below. To design rockbolt support to account for shear failure and the support of deadweight, the first part of the chart in Figure 4.6.1 can be used.

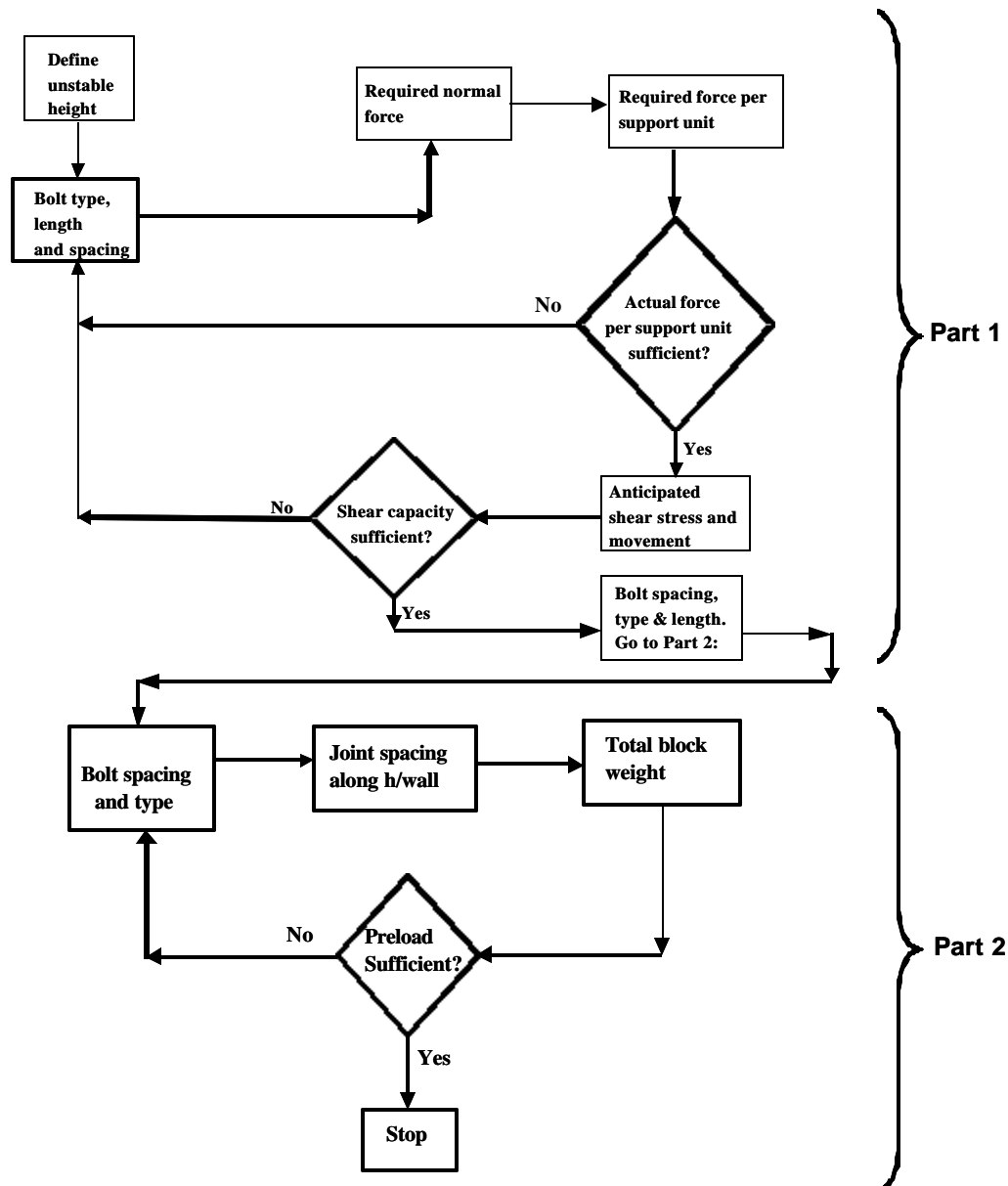


Figure 4.6.1 Flow chart for the design of rockbolt support taking into account deadweight, shear movement and cantilever failure of hangingwall beam.

To design tendon support for a stope hangingwall, choose the bolt type and the average spacing of the bolts. If the unstable height of rock in the hangingwall is known, the weight of the beam that is to be supported can then be obtained, which will in turn give the normal force required to support the hangingwall. The unstable height can be estimated by statistical analyses of the falls of ground that occurred on the mine or installing instrumentation that gives the height of the parting planes that open in the hangingwall. The required force per support unit can be obtained by dividing the total weight of the unstable hangingwall beam by the number of support units. This should then be compared to the actual force per support unit. If the actual force per support unit is not sufficient to prevent failure of the beam, then different bolt types or bolt spacing should be chosen. If the force per support unit is sufficient, the anticipated shear movement and shear stress must be determined. This can be done using numerical modelling. If the shear capacity of the system (which can be grouted or non-grouted bolts) chosen at the start of the design process is sufficient to prevent shear failure of these bolts, the support design process is completed. The engineer can now continue to the second part of the design process, which looks at cantilever failure of the hangingwall beam. The second part of the flow chart is proposed for tendon support design to counter cantilever failure and subsequent bending of the tendon.

The spacing between the joints along the hangingwall surface can be measured underground. Using the equations given in the previous sections in conjunction with the flow charts, the support spacing and the bolt preload can be determined. To determine the block weight, the joint spacing and the distance between the bolts must be taken into account. Chapter 4.3.3 concluded that the preload should always be more than the weight of the block. A factor of safety can be included to ensure that the blocks in the hangingwall are stable. This system accounts for the deadweight situation and the cantilever failure that may occur underground. Using the approach adopted in GAP 627 (Daehnke *et al.*, 1999) and/or GAP 335 (Haile *et al.*, 1998), together with the flow chart presented in Figure 4.6.1, tendon support can be designed to cater for the different hangingwall beams and deformation mechanisms. Although both approaches can be applied to any rock mass structure, it is recommended that the approach adopted in GAP 335 (Haile *et al.*, 1998) should be used if the rock mass is extremely blocky. The design process in GAP 627 (Daehnke *et al.*, 1999) is based on a single bedding plane in the hangingwall of a stope. The effect of a number of bedding planes is not considered in this project.

-

4.7 Numerical analysis of stress wave interactions with tendons

Haile *et al.*, 1998, established a relationship between the rock mass structure, tendon spacing and the peak particle velocities of the rock segments supported by the tendons. The analysis presented in the report was based on data obtained from *in situ* measurements. In this report, the relationship that was obtained in the report (Haile *et al.*, 1998) is investigated by means of numerical modelling. For this analysis, the universal distinct element code, UDEC (ITASCA, 1993), is used. UDEC is a two dimensional code that is able to model discrete blocks and assign different properties to any contact between two blocks. In the model, a P-wave is used to load the rock mass and support units.

4.7.1 Dynamic analysis in UDEC

The dynamic disturbance can be applied as a velocity history or as a stress history. The relationship between the applied stress and the velocity history is given by equations 4.7.1 and 4.7.2, for P- and S-waves, respectively.

$$s_n = 2(r C_p) V_n \quad (\text{for P-wave}) \quad 4.7.1$$

$$s_s = 2(r C_s) V_s \quad (\text{for S-wave}) \quad 4.7.2$$

where

s_n = applied normal stress

s_s = applied shear stress

r = mass density

C_p = P-wave velocity

C_s = S-wave velocity

V_n = input normal velocity

V_s = input shear velocity

The P-wave velocity through an elastic continuous medium is given by the equation:

$$C_p = [K + (4/3)G/r]^{1/2} \quad 4.7.3$$

where K and G are the bulk and shear modulus of the rock respectively.

For quartzite rock with a density of 2700 kg m^{-3} , the velocity of the P-wave is approximately 5600 m s^{-1} . If the applied normal stress is 20 MPa , the input velocity is 0.66 m s^{-1} .

4.7.1.1 UDEC model

A simplified model is used to investigate the influence of dynamic loading on different rock mass conditions and different support conditions. A graphical presentation of the model is given below.

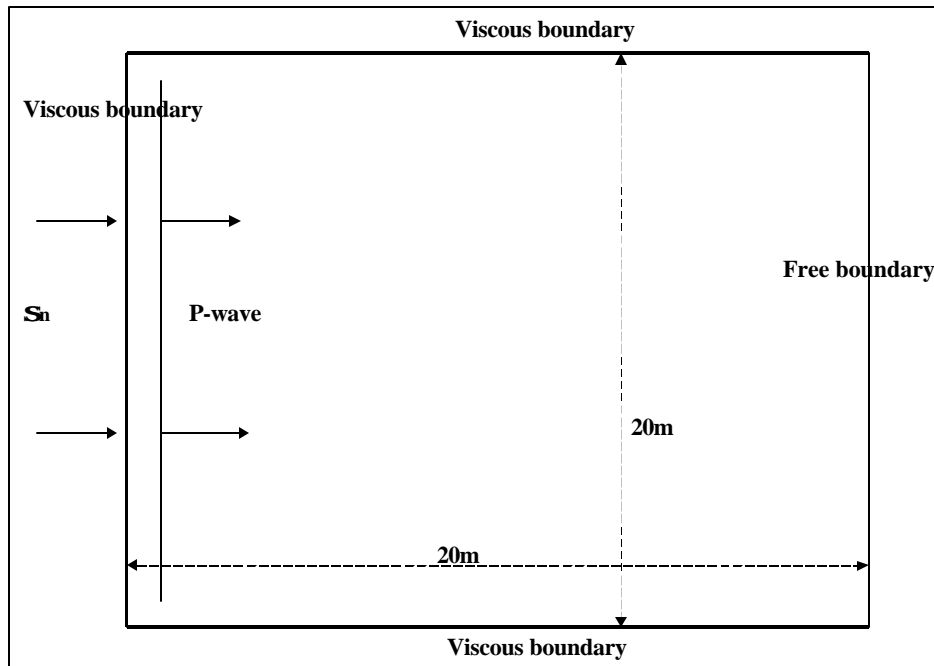


Figure 4.7.1 Graphical presentation of model.

A normal stress is applied to the boundary of the model which results in a P-wave which propagates through the rock mass. The value of the normal stress is varied to investigate the influence of higher velocities on the stability of the rock mass. Three boundaries (left, bottom and top) of the model were assumed to be viscous (non-reflecting) in both the x- and y-directions. The right hand side of the model was assumed to be a free surface. The rock mass is assumed to be under the influence of gravity. The value for the gravitational acceleration is $9,81 \text{ m s}^{-2}$. No normal or shear stresses, either internal or boundary stresses, were applied to the model. The rock mass properties are given below.

Table 4.7.1 Assigned rock mass properties.

Property	Value
Shear modulus	40 GPa
Bulk Modulus	30 GPa
Mass density	2700 kg/m^3
Joint normal stiffness	$2e11 \text{ N m}^{-1}$
Joint shear stiffness	$2e11 \text{ N m}^{-1}$
Joint friction angle	20°

A normal stress in the form of a sine wave is applied to the boundary and is illustrated in Figure 4.7.2. The wave has a frequency of 1000 Hz and is applied for a period of 0,0005 seconds. Thus, only half the wavelength is applied to the model. If the P-wave propagates at a velocity of 5600 m s^{-1} through the rock, it takes 0,00357 s to move through 20 m of rock. The free surface can reflect the wave back into the model. Thus, when the wave has reached the free surface, the model

is saved and the influence of the incident wave is analysed. Any interference due to reflection of the outgoing wave is thus be eliminated.

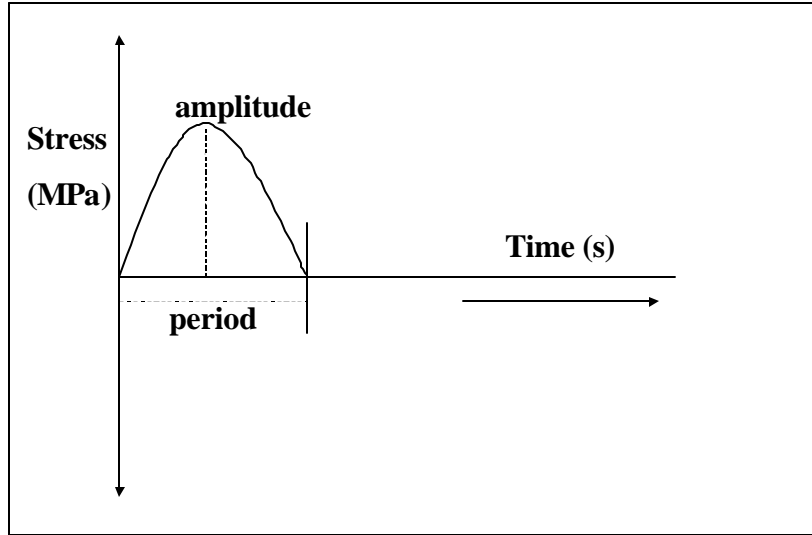


Figure 4.7.2 Sine wave applied as a normal stress to boundary of model.

4.7.2 Elastic Analysis

An elastic analysis was done to calibrate the model against the analytical solutions. The elastic model consists of a 20 m x 20 m block. Velocity history points were located at points along the free surface. From these history points, the time taken for the wave to reach the free surface of the model, and the peak particle velocities at the free surface could be determined. In the elastic model the orientation of the wave front with respect to the horizontal axis can be established and compared to the cases where there are cracks in the model. A plot of the maximum shear stress (isochromatic wave field) can indicate the position of the P-wave at any given time. This is calculated using the following equation.

$$t_{max} = (s_{max} - s_{min})/2 \quad 4.7.4$$

A plot of the isochromatic wave field is shown in the Figure 4.7.3. A plot of the stresses in the x-direction is shown in the Figure 4.7.4.

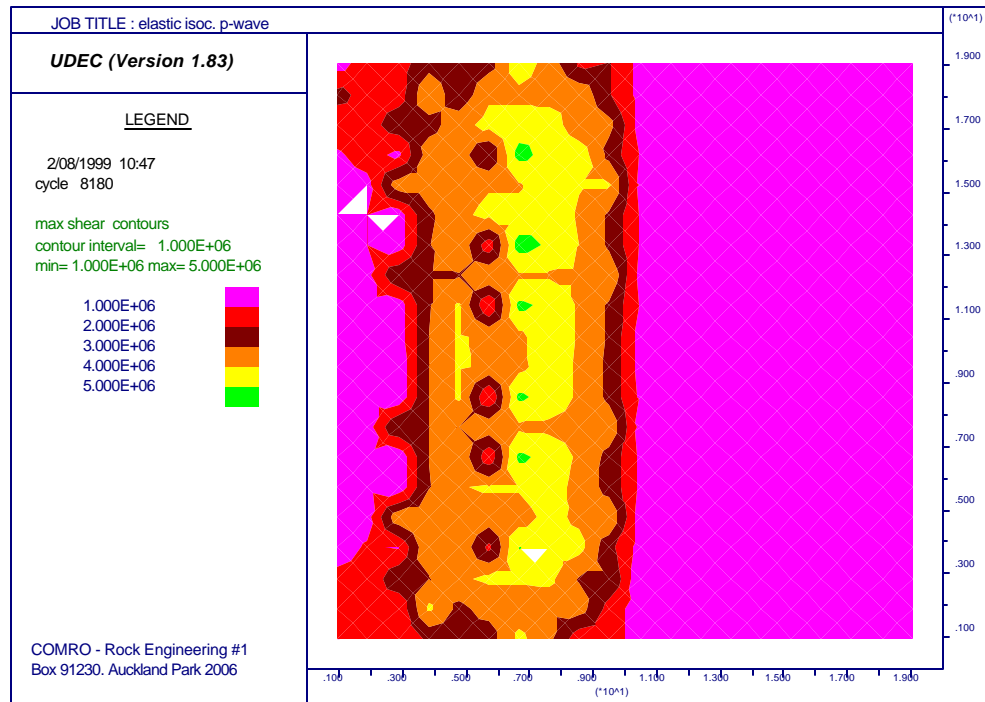


Figure 4.7.3 Isochromatic wave field showing orientation of wave front.

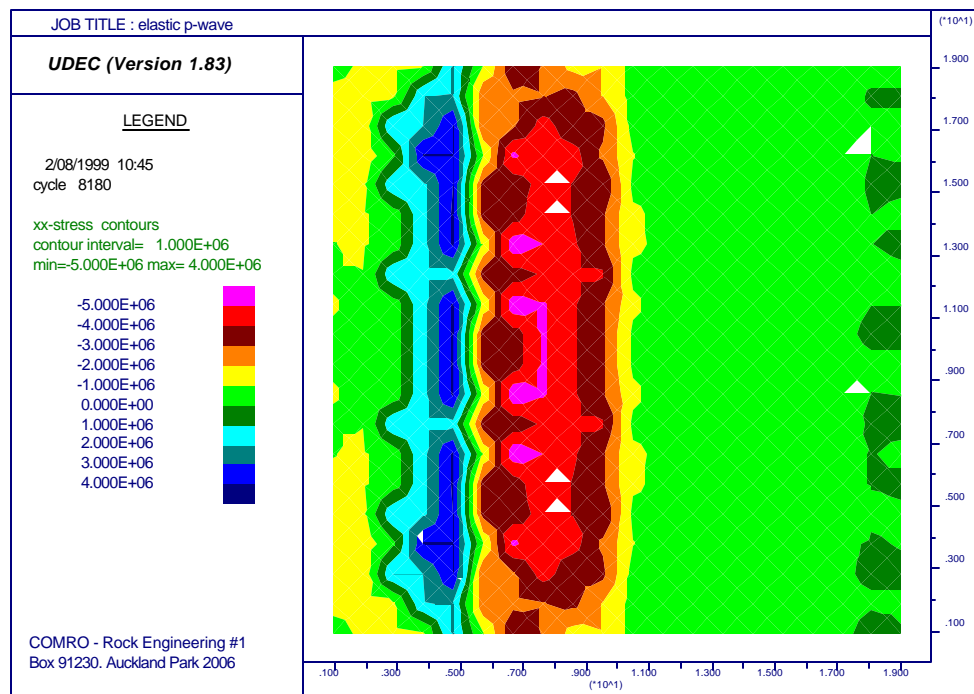


Figure 4.7.4 Contour plot of stresses in x-direction.

The wave in the model is a longitudinal wave, i.e. zones of compression and tension can be distinguished as the wave propagates. The velocity seismogram that was recorded at the centre of the free surface is given below.

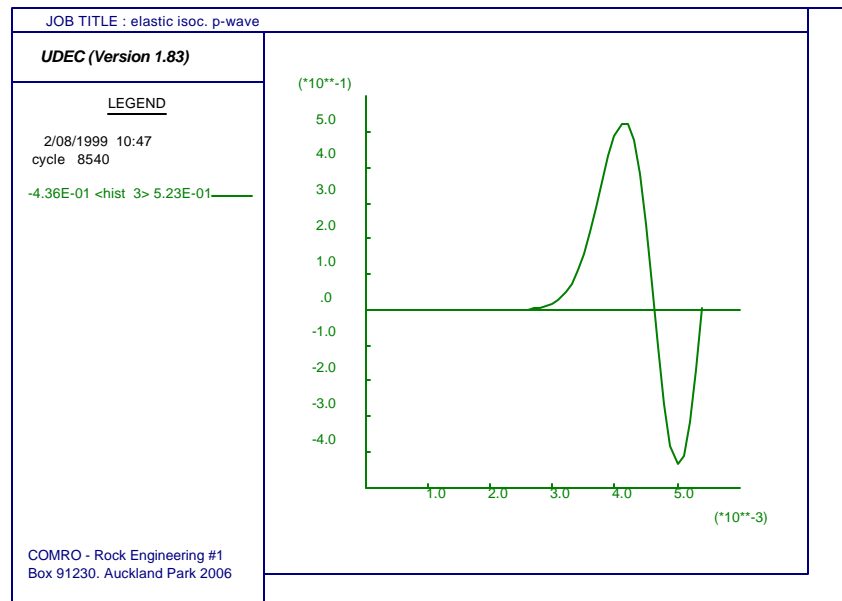


Figure 4.7.5 Velocity seismogram showing ground motion at centre of free surface.

It is evident that the peak particle velocity at the centre point of the free surface is approximately 0,5 m/s. Integration of the velocity will give the acceleration of the points that were monitored.

4.7.3 Influence of cracks

In the elastic medium, the wave travels at a speed of 5600 m s^{-1} and it takes approximately 0,00357 s to reach the free surface. The influence of vertical cracks in the model on the travel time of the P-wave is investigated in the next section.

4.7.3.1 Influence of vertical cracks on the travel time of a vertical P-wave

For a discontinuity spacing of 1 m, the travel time of the P-wave is 0,0043 s (i.e. 0,001 seconds slower than the P-wave in the elastic medium). The wave front orientation through the vertical cracks remains vertical (parallel to the incident P-wave). No interference other than the reduction in wave speed is experienced in the jointed medium. The isochromatic wave field of the P-wave is shown in the Figure 4.7.6.

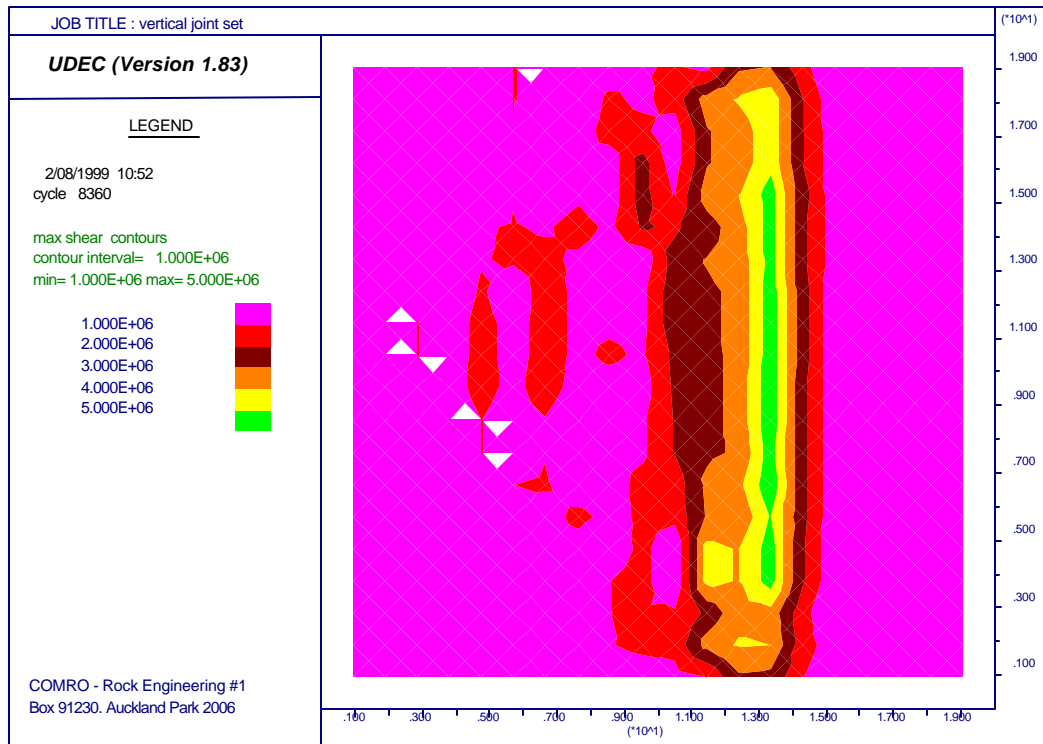


Figure 4.7.6 Isochromatic wave field of p-wave.

The compressive front of the P-wave caused some closure to occur on the joints, but no opening of the joints occurred. A maximum tensile stress of 7 MPa was obtained. Thus, any pre-existing fractures that are parallel to the P-wave and have a tensile strength less than 7 MPa can be expected to open up. Very little shearing occurred along the vertical joints. The ground motion at the centre of the free surface has the same form as in the elastic model. This is shown in Figures 4.7.7 and 4.7.8.

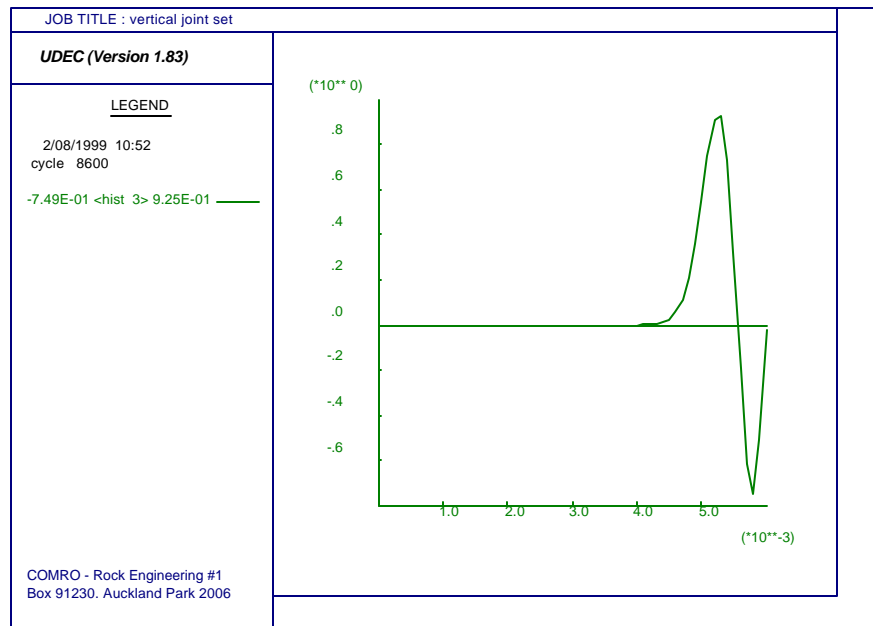


Figure 4.7.7 Ground motion recorded at point P.

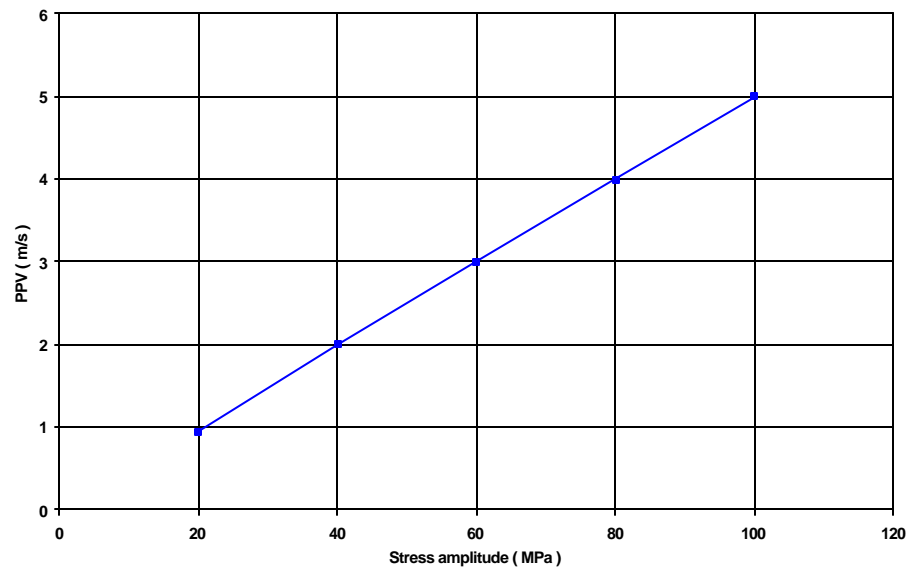


Figure 4.7.8 Influence of stress amplitude and vertical cracks.

4.7.3.2 Influence of joint spacing on the peak particle velocities measured at the free surface and the travel time of the wave

The influence of different joint spacing on the travel time of the P-wave is shown in the Figure 4.7.9. The values are given in Table 4.7.2.

Table 4.7.2 Influence of joint spacing on travel time.

Joint spacing	Travel Time
2 m	0,0035 s
1,5 m	0,0038 s
1 m	0,0043 s
0,5 m	0,0053 s

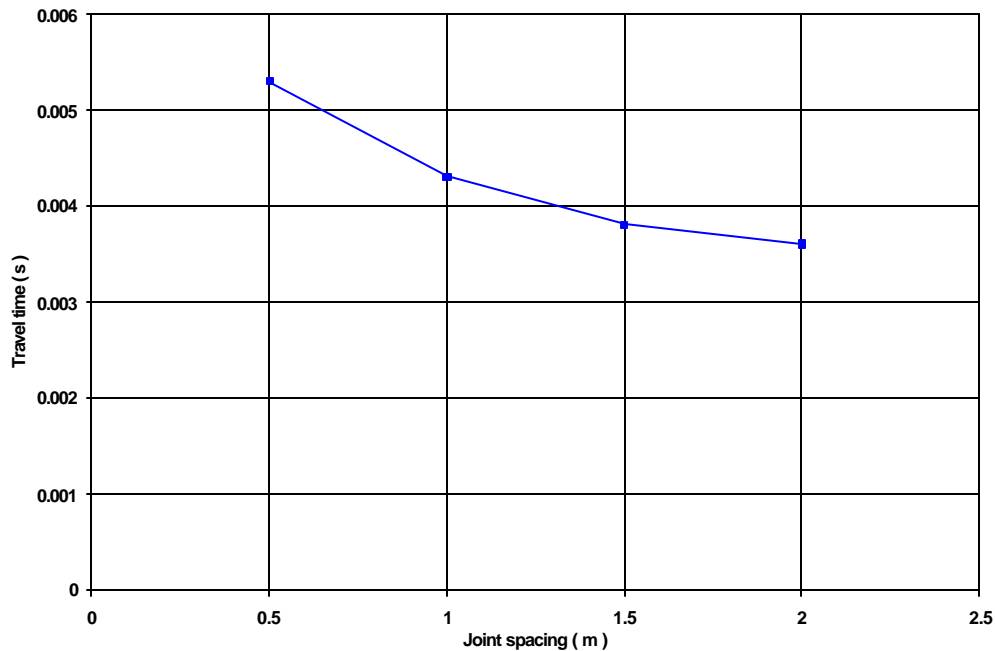


Figure 4.7.9 Influence of joint spacing on the travel time of the wave.

It is clear that the wave speed decreases rapidly with a decrease in the joint spacing.

The influence on the peak particle velocity at the centre of the free surface is shown Table 4.7.3 and Figure 4.7.10. From these results it is evident that the peak particle velocities increase with a decrease in the joint spacing.

Table 4.7.3 Influence of joint spacing on peak particle velocity.

Joint spacing	PPV
2 m	0,55 m/s
1,5 m	0,7 m/s
1 m	0,95 m/s
0,5 m	1,2 m/s

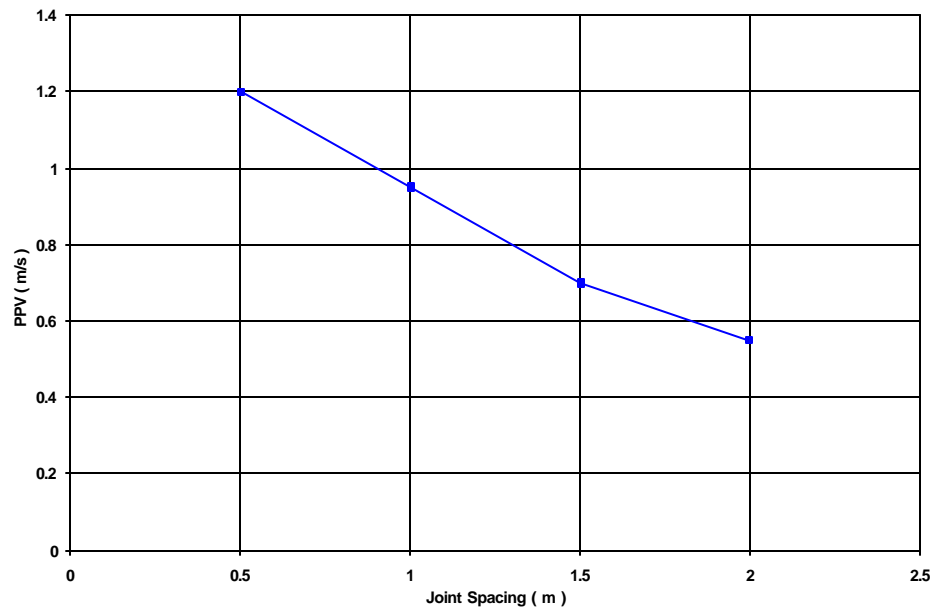


Figure 4.7.10 Influence of joint spacing on peak particle velocity.

4.7.3.3 The influence of horizontal and vertical cracks on the wave travel time and peak particle velocities at the free surface

In the model analysed here, the travel time of a P-wave through rock that has both horizontal and vertical joints spaced at 1 m is 0,0043 seconds. This is similar to the travel time through a rock mass that consists of only vertical joints. Thus, in this model the horizontal joints do not influence the travel time of the P-wave significantly. The horizontal joints do not influence the peak particle velocities at the free surface, nor do they affect the orientation of the P-wave. This is shown in Figure 4.7.11.

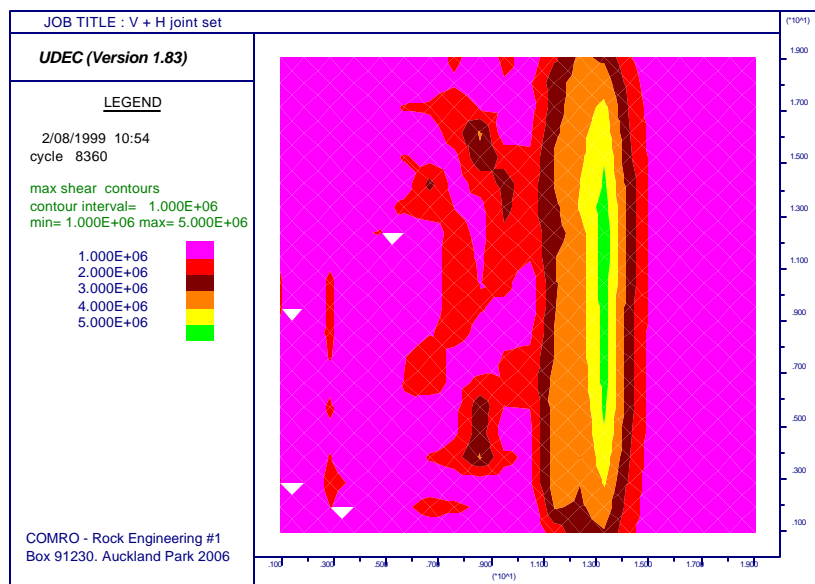


Figure 4.7.11 Isochromatic wave field showing the P-wave.

4.7.3.4 Influence of joint orientation on the P-wave propagation

Consider the scenario where a stress wave travels through a rock mass consisting of joints dipping at 45 degrees with respect to the horizontal, towards the free surface.

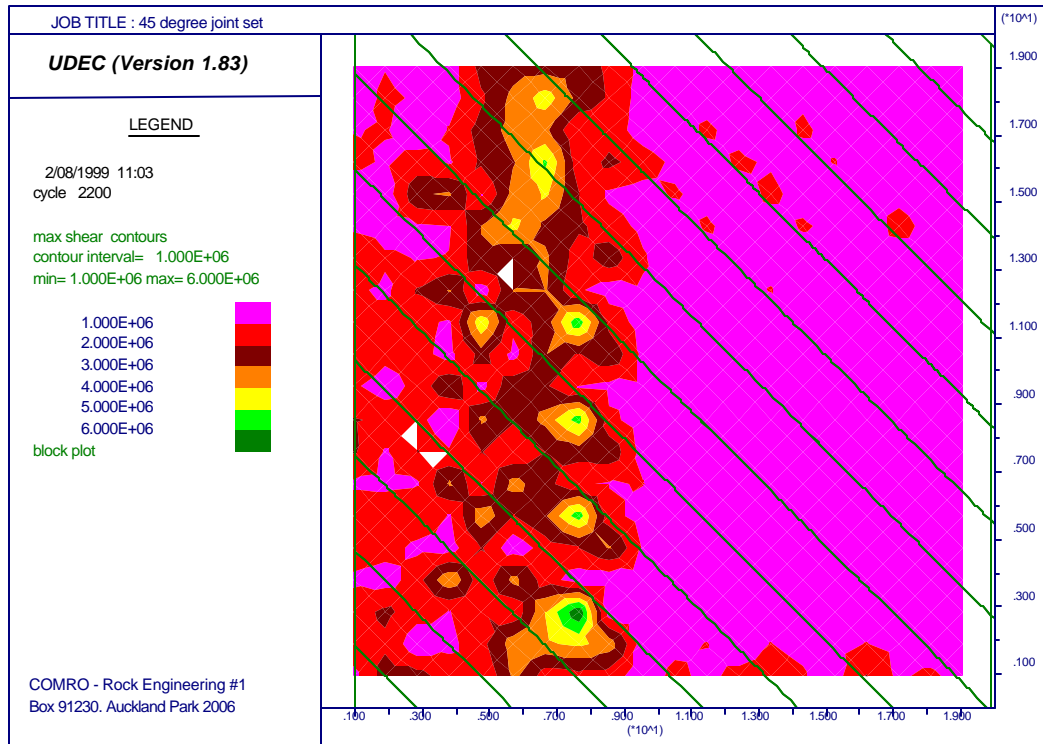


Figure 4.7.12 *Isochromatic wave field showing P-wave.*

When comparing this to the elastic model, we see that the travel time has slightly increased but the peak particle velocities are the same. The joints do not, however, influence the overall orientation of the wave front.

4.7.3.5 Influence of tendon support – comparison to underground data

A simulated rockburst experiment was conducted at Kopanang mine as part of SIMRAC Project GAP 335 (Haile *et al.*, 1998). The effectiveness of the rock bolt reinforcement in influencing the dynamic response of the rock mass and containing potential rockburst damage was the focus of this aspect of the investigation. The monitoring programme and instrumentation to evaluate this included measurement of the area and volume of damage, and the use of geophone arrays between rock bolts (Figure 4.7.13) to measure the stable response of the rock mass.

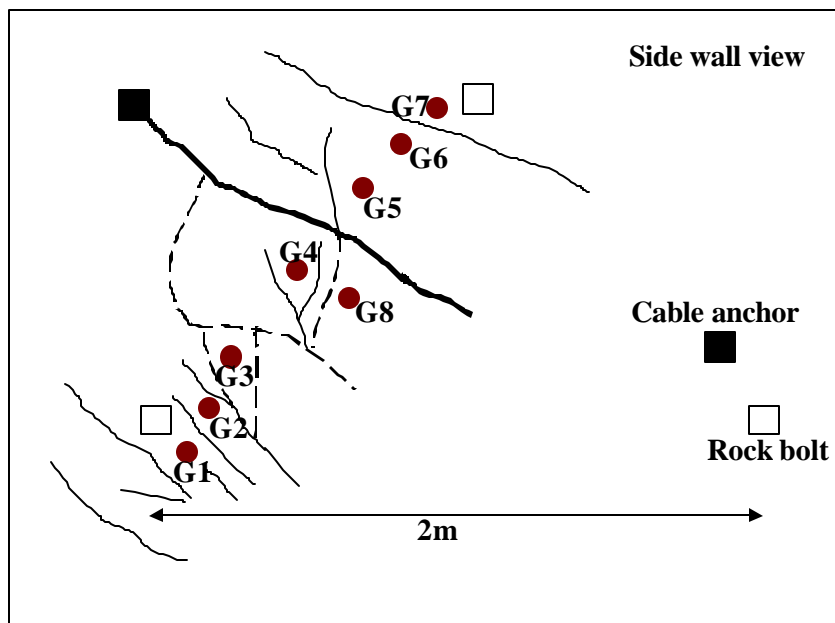


Figure 4.7.13 *The array of geophones between the rock bolt units and an indication of the exposure of the rock mass structure on the sidewall of the tunnel (after Le Bron et al., 1999).*

Mapping of the rock mass structure was also conducted prior to the experiment in order to classify the rock mass at the skin of the tunnel. Mapping of the rock mass indicated the average bedding plane separation in the vicinity of the instrumentation to be approximately 50 cm and dipping at 30° in the plane of the sidewall. Stress fracturing associated with the development of the tunnel was approximately vertical, generally open up to 2 mm and at a spacing of approximately 10 cm along the axis of the tunnel. The stress fracturing made an angle of approximately 20° with the sidewall of the tunnel creating wedge shape blocks within the rock wall.

Prior to the simulated rockburst the tunnel sidewalls were whitewashed and the footwall cleaned to allow easy identification of subsequent damage due to the simulated rockburst. The damage to the excavation is illustrated in Figure 4.7.14 by the exposed (darker) areas on the sidewall and the ejected rock mass on the footwall.



Figure 4.7.14 ***Photograph showing rockburst damage along the experimental tunnel. The area of high intensity damage is in the foreground and low intensity damage towards the background (after Le Bron et al., 1999).***

There was a clearly defined area of high intensity damage over a tunnel length of approximately 10 m. This area is located adjacent to the estimated position of the blastholes, which formed the simulated seismic source. Away from this zone, in advance of the end of the blastholes, minor damage was observed over a further 10 m. In no case was there failure of the rock bolt reinforcement. The blocks that were ejected from the rock wall were defined by the pre-existing discontinuities. The length of the blocks, as delineated in the sidewall rock mass, varied between 40 cm to 80 cm, the width varied between 30 cm to 50 cm as defined by the bedding separation, and the thickness was approximately 15 cm as defined by the stress fracturing. The maximum block volume was approximately $0,07 \text{ m}^3$. All the damage was confined to the sidewall adjacent to the simulated seismic source.

The array of geophones between the rock bolts was located outside the area of observable damage. The data from this site clearly illustrated an influence of a rock bolt reinforcement unit on the dynamic response of the local rock mass. The response of the rock mass in relation to a rock bolt reinforcement unit is shown in Figure 4.7.15.

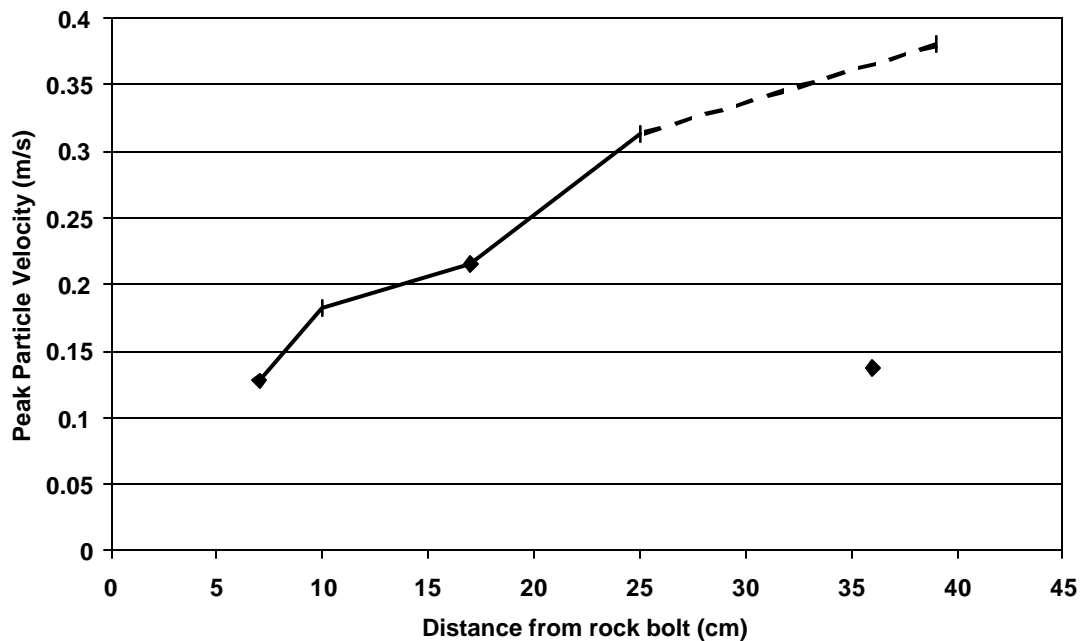


Figure 4.7.15 *In situ relationship between PPV and distance from a rock bolt reinforcement unit (after Le Bron et al., 1999).*

Figure 4.7.15 clearly illustrates the general trend of increased PPV with increased distance from the rock bolt reinforcement. The data point at approximately 36 cm from the rock bolt is anomalous to the general trend and considered to be due to the inherent variability in the rock mass. This behaviour of increased PPV with distance from the rock bolt is in accordance with measurements at other tunnel sites (Haile *et al.*, 1998) under conditions of natural seismicity. Increased amplification of PPV has been shown to be associated with the fracturing around an excavation, and, thus, increased discontinuity of the rock mass (Durrheim *et al.*, 1996). The influence of the rock bolt reinforcement is to maintain a higher degree of interaction and inherent strength within the rock mass. This will thus reduce the potential for amplification of peak ground velocities. With distance away from the rock bolt unit, the discontinuous rock mass is under reduced reinforcement and thus has an increased degree of freedom. In situ observations of rockburst damage (Haile, 1999) have shown this reduced retainment of the rock mass away from the rock bolt reinforcement to result in substantial rock mass unravelling under severe dynamic loading.

In an attempt to mechanistically evaluate the interaction between rock bolt reinforcement and the rock mass under dynamic loading, numerical modelling using the Universal Distinct Element Code was conducted. In this exercise it was not attempted to quantify the influence of the rock bolt unit in terms of absolute PPV values, but to qualitatively capture the mechanism of PPV amplification with distance from the rock bolt. Figure 4.7.16 is an example of the model geometry showing ground velocity perpendicular to the free surface.

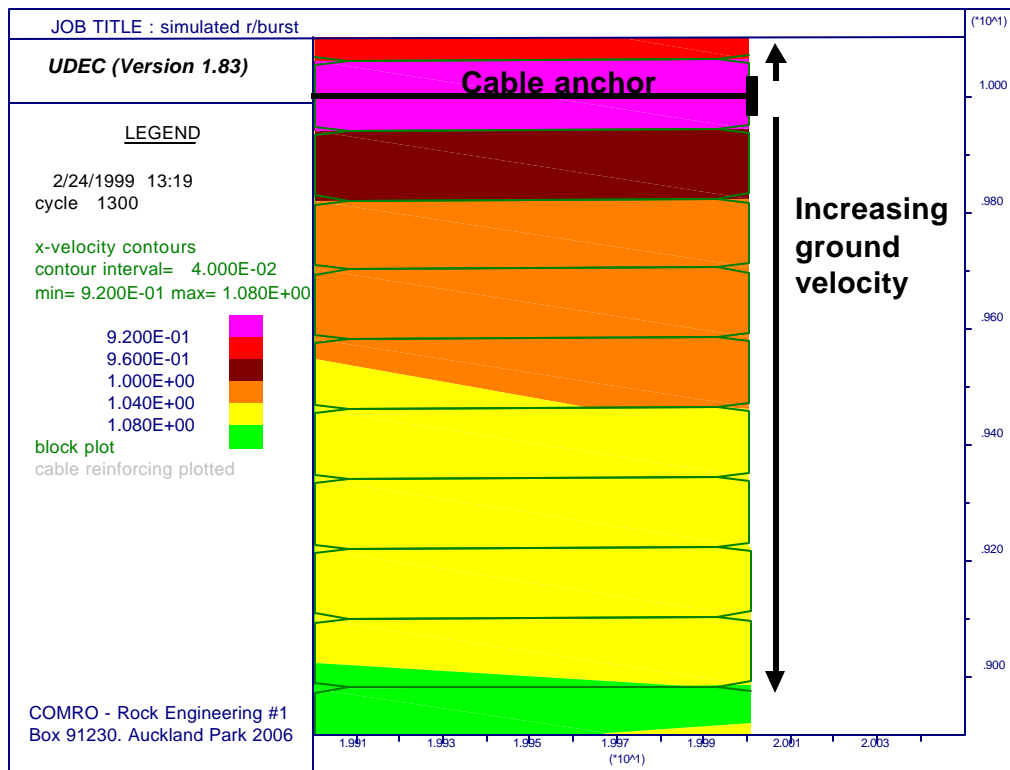


Figure 4.7.16 *Example of the numerical model showing velocity contours, rock mass structure and rock bolt reinforcement unit (after Le Bron et al., 1999).*

Geophones were located at 0,25 m intervals from the support unit at the centre of the free surface in the model. The spacing of the joints close to the free surface where the geophones were positioned were made the same as those measured underground. The other joints were spaced at 1 m to decrease the run time of the model. Figure 4.7.17 shows the influence of support on the peak particle velocities at the free surface.

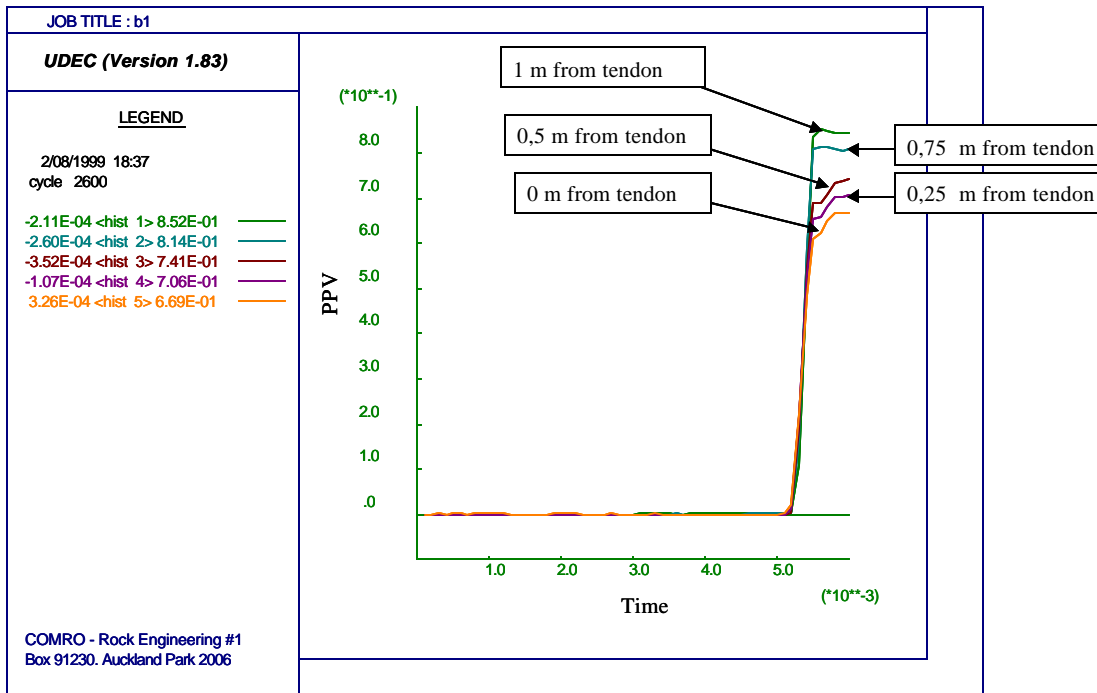


Figure 4.7.17 **Peak particle velocities at support and at 0,25 m intervals away from support.**

The peak particle velocities at the support are lower than further from the support. The trend is the same as that obtained from the underground data (Haile *et al.*, 1998).

4.7.4 Summary of numerical results

Numerical models were used to investigate the interaction of a stress wave with the rock mass. The influence of rock mass parameters, support and wave properties on the stability of the rock mass were investigated.

For the elastic model, the stress amplitude is directly proportional to the peak particle velocities experienced by the points along the free surface. The travel time of the wave is, however, not influenced by the stress amplitude. The travel time of the wave is increased when the joint spacing is decreased and the joint orientation is not parallel to the orientation of the wave front. The orientation of the wave front is not influenced by the joint orientation with respect to the horizontal. This was done for a joint spacing of 2 m and could change if the joint spacing is less than 2 m.

The peak particle velocities that were recorded at the free surface are influenced by the support. The peak particle velocities at points close to the support were lower than at points further from the support. The support spacing made only a small difference. The support length had no influence on the peak particle velocities. No particular trend was established for the influence of block size on the peak particle velocities at the free surface.

4.8 An engineering approach to the design of stope face support systems in tabular stopes

4.8.1 Introduction

An engineering approach to the design of support systems, in particular the support strength, energy absorption and spacing requirements, is proposed. The approach makes use of models and support design methodologies developed as part of SIMRAC projects GAP032 'Stope and Gully Support' (Roberts, 1995), GAP330 'Stope Face Support Systems' (Daehnke *et al.*, 1998), GAP335 'Strata Control in Tunnels' (Haile *et al.*, 1998), and GAP627 'Zones of Support Influence' (Daehnke *et al.*, 1999). The findings of these projects culminate in comparatively complex theoretical models describing the rock mass interaction with support units and support requirements during quasi-static and dynamic loading conditions.

The design method proposed here combines the salient findings of the above-mentioned projects to provide a unified support design methodology for rockfall and rockburst conditions in different geotechnical areas. This design tool is of practical value and enables the rock engineer to make initial designs of appropriate support systems by using a few comparatively straightforward graphs.

It is emphasised, however, that certain assumptions are made during the design process. To ensure rock mass stability and reduce rock-related hazards, these assumptions are generally conservative, i.e. the resulting support system is marginally over-designed, providing some factor of safety. To fully optimise the support system, it is recommended that the complete models developed by, specifically, SIMRAC projects GAP330, GAP335 and GAP627 be applied. It is further recommended that appropriate software, such as SDA II (CSIR, 1999), be used to expedite the more accurate evaluation of support systems.

The core of the design methodology proposed here is a set of seven graphs, which facilitate the design of support systems under various loading and geotechnical conditions. These graphs are given below, and their associated assumptions and design implications are discussed. For convenience, design flowcharts leading to the correct application of the graphs, as well as the graphs themselves, are given in Section 4.8.3. Finally, support design examples for rockfall and rockburst conditions are also given in Section 4.8.3.

4.8.2 Support Design Graphs

4.8.2.1 Fundamental tributary area requirements for rockfall conditions

Figure 4.8.1 gives the maximum tributary area (A_T) that can be supported by a single support unit for rockfall conditions. The tributary area is given as a function of the height of potential rock mass instability and support force. The height of instability (b) is commonly governed by the position of bedding planes, and should be determined from previous rock mass instabilities and FOGs.

The basic tributary area relationship, $F = r g b A_T$, can be re-written as:

$$A_T = \frac{F}{r g b} , \quad [4.8.1]$$

where: A_T = maximum potential tributary area (m^2),

F = support unit load (N),
 r = rock density (2700 kg/m^3),
 g = acceleration due to gravity (10 m/s^2), and
 b = height of instability (m).

Figure 4.8.1 shows the relationship given by Equation 4.8.1 graphically.

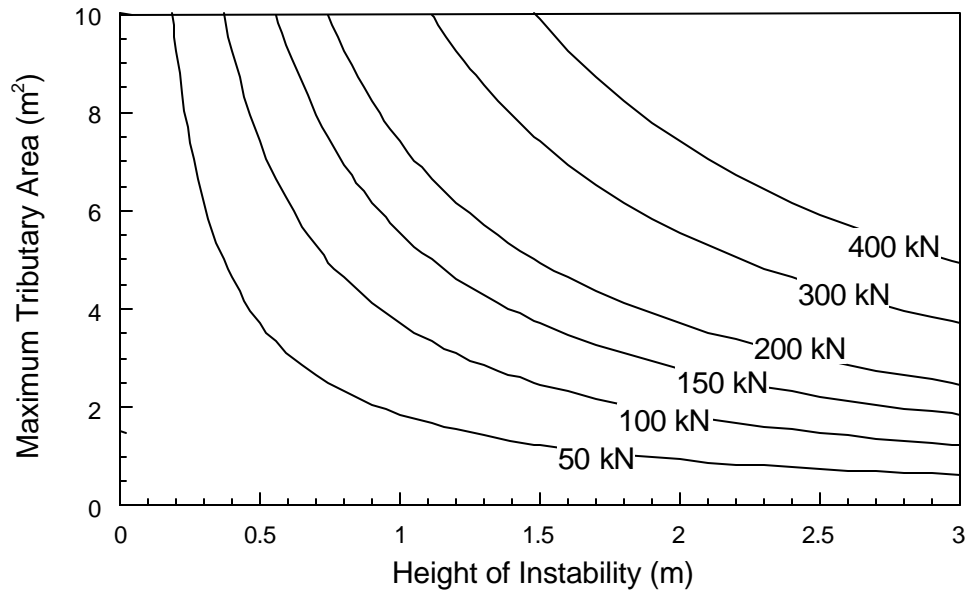


Figure 4.8.1 Tributary area requirements for rockfall conditions.

Assume that a support unit with the force versus deformation characteristics shown in Figure 4.8.2 is used. It is further assumed that the closure rate, as measured in the stope, is 20 mm per metre of face advance, and the support unit should maintain rock mass stability as the face is advanced a further 10 m. This implies that for at least 200 mm of closure the support unit needs to carry sufficient load to meet the tributary area requirements.

At 200 mm deformation the support unit carries a load of 180 kN. For the rock mass to be stable over this deformation range (based on the tributary area criterion), the maximum tributary area should not exceed $4,5 \text{ m}^2$ (determined from Figure 4.8.1, assuming $F = 180 \text{ kN}$ and $b = 1,5 \text{ m}$).

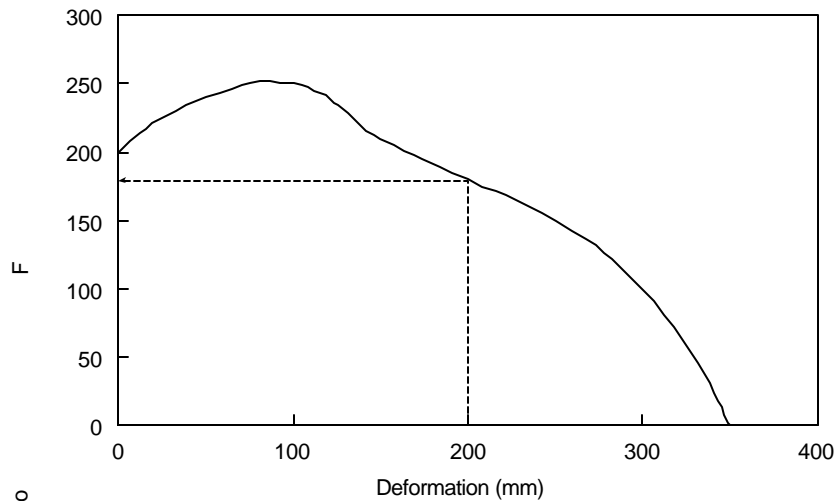


Figure 4.8.2 Design force versus deformation curve of hypothetical support unit (in this example the support unit was initially pre-stressed to 200 kN)

The distance from the stope face, at which the support system needs to ensure rock mass stability (i.e. in the above example: 10 m + support installation distance from the face) is an important support design consideration. This distance should at least extend to the sweeping line (typically 5 – 6 m from the face), and preferably into the back area of the stope (Figure 4.8.3). By ensuring the support performance criteria are met for this distance, the rock mass stability is maintained over an area extending at least up to the sweeping line.

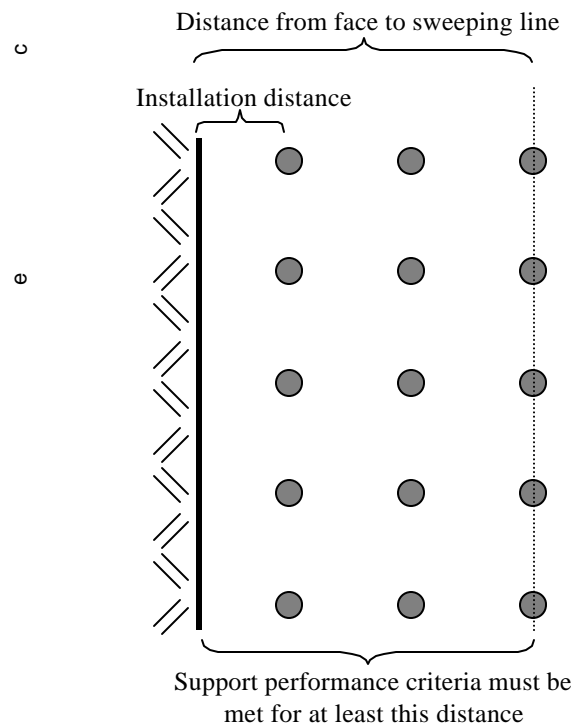


Figure 4.8.3 Stope plan view indicating minimum distance behind face over which the support performance criteria must be met.

4.8.2.2 Fundamental tributary area requirements for rockburst conditions

Energy absorption (rockburst) requirements based on the tributary area criterion follow analogously to the support resistance (rockfall) case. Figure 4.8.4 gives the maximum tributary area as a function of the height of instability and the energy absorption capacity of the support unit. The relationship is based on the well-known kinetic and potential energy absorption criterion (Wagner, 1984), i.e. $E_a = 0.5 m v^2 + m g h$, where $m = r b A_T$. The relationship is re-written as:

$$A_T = \frac{E_a}{r b (0.5 v^2 + g h)} \quad , \quad [4.8.2]$$

where:

- A_T = maximum potential tributary area (m^2),
- E_a = energy absorption capacity of the support unit (J),
- r = rock mass density (2700 kg/m^3),
- b = height of instability (m),
- v = rock ejection velocity (3 m/s),
- g = acceleration due to gravity (10 m/s^2), and
- h = hangingwall displacement during dynamic event (0.2 m).

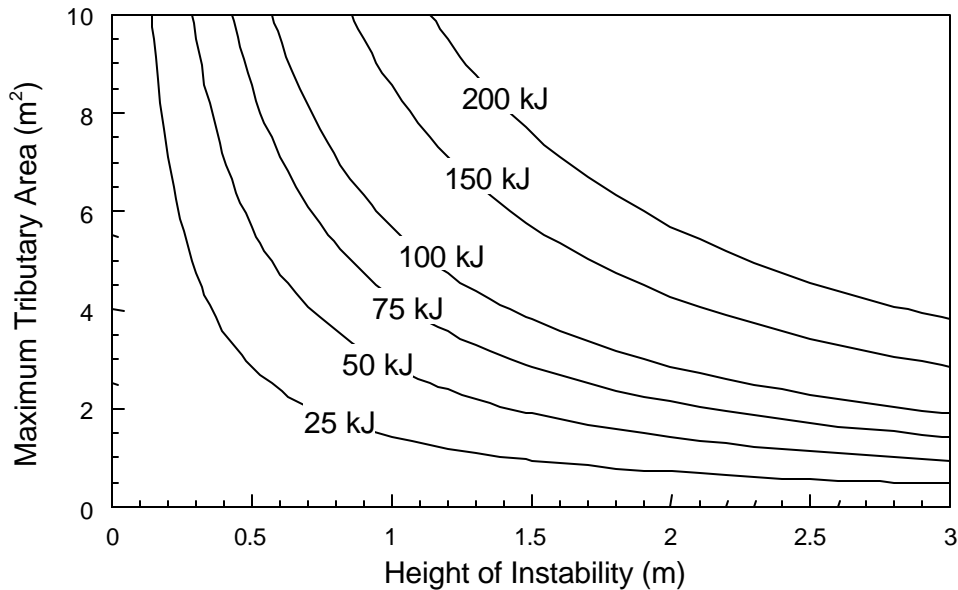


Figure 4.8.4 Tributary area requirements for rockburst conditions.

The use of Figure 4.8.4 is illustrated by means of an example. Assume that a support unit is used with a force versus deformation curve as shown in Figure 4.8.3. The design requirements are that, as the face is advanced a further 5 m, the support unit must maintain rock mass stability during a rockburst and retain a support resistance after dynamic deformation of mg . Stope closure is 20 mm per metre of face advance, i.e. the support unit needs to maintain rockburst stability after having been compressed by up to 100 mm of quasi-static closure. Figure 4.8.5 graphically illustrates the remaining energy absorption capacity of the support unit (calculated by the area under the force versus deformation curve).

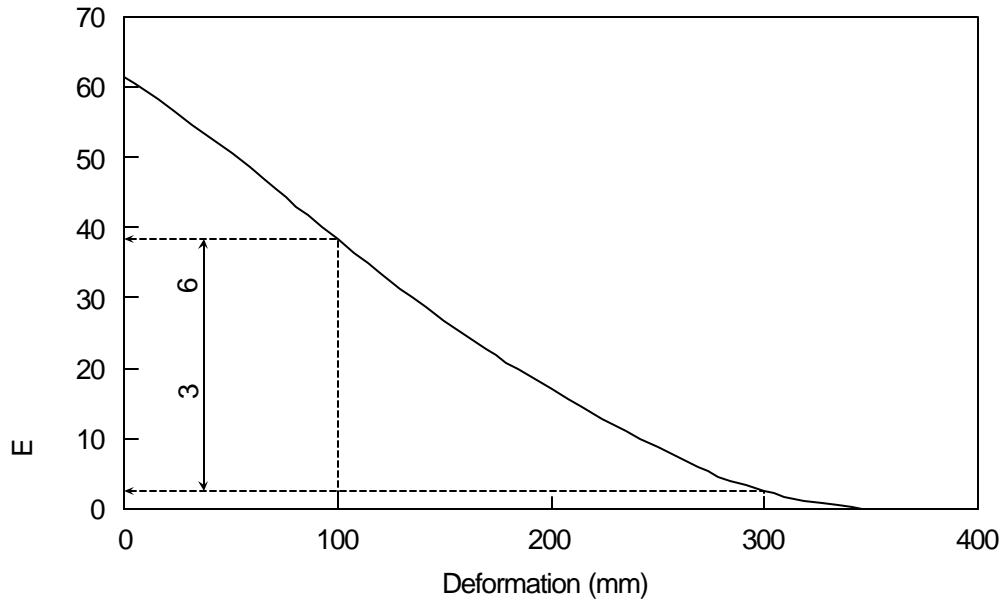


Figure 4.8.5 Remaining energy absorption capacity of the hypothetical support unit.

From Figure 4.8.5 it is apparent that after 100 mm of deformation, 38 kJ of energy absorption capacity remains available. The hangingwall is assumed to displace dynamically over a distance of 0,2 m, i.e. up to 300 mm deformation. At this point only 2 kJ energy absorption capacity remains. The change in energy absorption capacity, i.e. $\Delta E_a = E_a(100 \text{ mm}) - E_a(300 \text{ mm}) = 36 \text{ kJ}$, is the amount of energy available. The tributary area criterion is based on this amount of energy, i.e. in this example 36 kJ. From Figure 4.8.4 it is apparent that the maximum tributary area should not exceed $1,5 \text{ m}^2$ (assuming $E_a = 36 \text{ kJ}$ and $b = 1,5 \text{ m}$).

Two further [□] criteria, which need to be considered when designing rockburst resistant support systems, are:

1. The load carried by the support unit after the rockburst must exceed the corresponding tributary area load. In this example $F(300 \text{ mm}) = 100 \text{ kN}$, which is adequate to support the tributary area load $= r g b T_A = 61 \text{ kN}$. (If the load carried by the support unit after the rockburst is less than the tributary area load, a different support unit should be chosen or the support spacing reduced.)
2. The stoping width minus the total closure after the rockburst should be adequate to prevent injury to, and allow movement of, mine personnel. A minimum post-rockburst stoping width of 0,6 m is recommended, i.e. in the example given here the initial stoping width should not be less than 0,9 m.

In the design method given here a dynamic hangingwall displacement of 0,2 m is assumed. In practice the downward movement of the hangingwall is dependent on the support reaction and, for example, a support system providing high support resistance will arrest the hangingwall within a shorter distance. In this case the potential energy component is decreased and hence the total energy absorption requirements are reduced. In practice most support systems will decelerate the hangingwall over a distance less than 0,2 m. The $h = 0,2 \text{ m}$ assumption made here is conservative. To fully optimise support systems the use of the SDA II software is recommended, where the value of h is explicitly calculated for each support unit.

4.8.2.3 Support spacing requirements for rockfall conditions and hangingwalls with face-parallel fractures (FPFs)

The tributary area requirements reviewed in the previous sections are adequate to address general stability requirements of a continuous, unfractured hangingwall beam. In practice, however, the hangingwall is discretised by joints and mining induced fractures. In a highly discontinuous hangingwall the tributary area criteria are not sufficient to ensure rock mass stability and, in addition, the rock mass stability between adjacent support units needs to be considered.

In this section the stability criteria of a hangingwall with FPFs (face parallel fractures) are developed. The failure of hangingwalls with FPFs is generally characterised by keyblock failure (sliding and rotational failure) and beam buckling. An example of a hangingwall with FPFs is given in Figure 4.8.6.



Figure 4.8.6 Example of a hangingwall with FPFs.

The work conducted as part of SIMRAC projects GAP330 (Daehnke *et al.*, 1998) and GAP627 (Daehnke *et al.*, 1999) quantified the rotational, sliding and buckling stability envelopes of hangingwall keyblocks. It was found that the stability is predominantly governed by the keyblock height (b) and the angles of the discontinuities discretising the keyblock, a and b (see Figure 4.8.7). In intermediate and deep level mines the angles a and b are normally defined by face parallel mining induced extension and shear fractures.

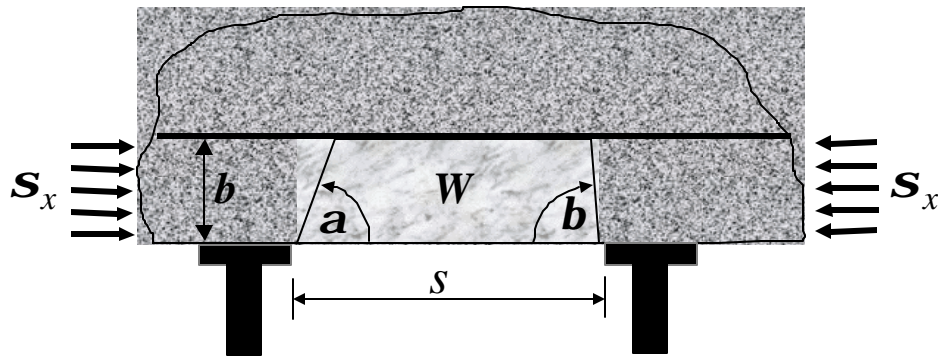


Figure 4.8.7 Critical keyblock parameters influencing the rock mass stability.

It was further found that the compressive hangingwall stresses contribute towards the hangingwall stability. In the design method proposed here, a compressive stress of $s_x = 1$ MPa is assumed. In deep level mines s_x might exceed 1 MPa, however, until further *in situ* measurements have been made, $s_x = 1$ MPa is considered an appropriately conservative assumption for the purposes of designing support systems.

Figure 4.8.8 gives stability envelopes of keyblocks based on instability height (b), support force (F), unsupported span (s), discontinuity angles (a and b), and g , where $g = 90^\circ - f$ and f is the apparent friction angle associated with the fracture surfaces. Due to the interlocking and matching surfaces of mining induced fractures, the apparent friction angle (f) is relatively high, and values of 50° to 60° are considered realistic.

Two main stability zones are given in Figure 4.8.8:

- (i) **Dark grey zone:** Here the keyblocks are discretised by shallow dipping fractures and keyblock rotation and subsequent sliding is likely. In this zone the stability of keyblocks is governed by overlapping zones of support influence, and the work conducted during SIMRAC project GAP627 (Daehnke *et al.*, 1999) is applied to estimate maximum stable unsupported spans, whilst maintaining rock mass stability. In quantifying the extent of the zones of support influence, a bedding plane friction angle of 20° is assumed.
- (ii) **Light grey zone:** Relatively steeply dipping fractures reduce the possibility of block rotation and failure is generally governed by beam buckling. Note that in this case the zones of influence also contribute towards the hangingwall stability, and the maximum stable unsupported spans are consequently extended. The extent of this zone is dependent on the fractured hangingwall stiffness. Data from Bandis *et al.* (1983) was used to estimate the stiffness of the fractured hangingwall (for further details see Daehnke *et al.*, 1998).

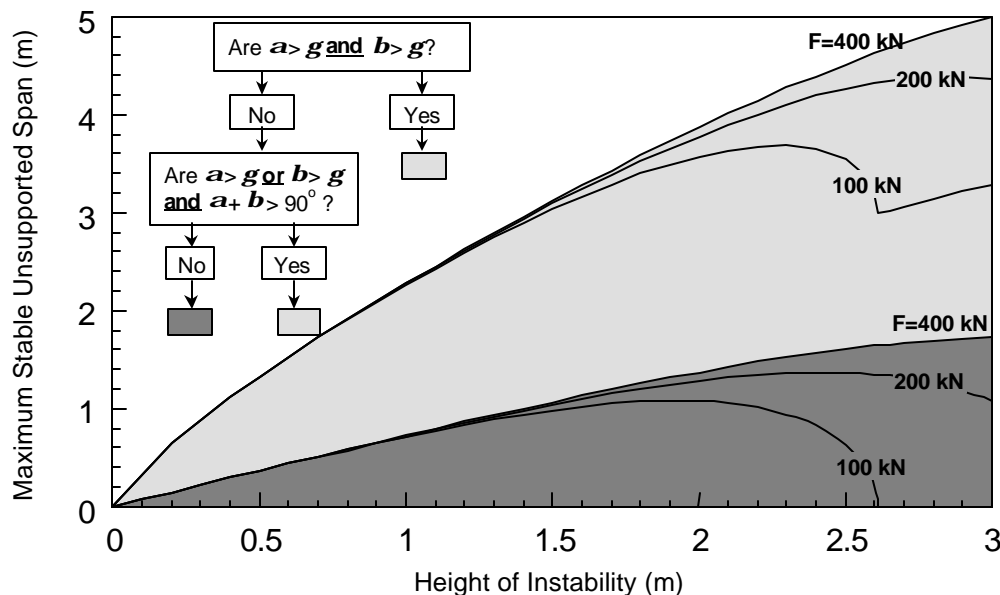


Figure 4.8.8 Rockfall stability envelopes for hangingwalls with FPFs as a function of instability height, unsupported span, support load and discontinuity orientation ($g = 90^\circ - f$, where f is the friction angle associated with the fracture surfaces).

As an example, consider the stability of a hangingwall discretised by face-parallel extension and shear fractures dipping at $a = 50^\circ$ and $b = 30^\circ$, respectively, and the friction angle is assumed to be $f = 50^\circ$ (hence $g = 90^\circ - 50^\circ = 40^\circ$).

Are $a > g$ and $b > g$? No.

Are $a > g$ or $b > g$ and $a + b > 90^\circ$? No.

Since $a + b < 90^\circ$, the dark grey stability zone is applicable (using the flowchart in Figure 4.8.8). Assuming a support unit load of $F = 200$ kN and height of instability $b = 1,5$ m, the maximum stable unsupported span is determined from Figure 4.8.8 as 1,0 m. Note that, by installing props with headboards, the unsupported span remains the same, but the prop spacing can be increased by the length of the load spreader.

If $a = 60^\circ$ and $b = 80^\circ$ and the friction angle is assumed to be $f = 50^\circ$ (hence $g = 40^\circ$), the stability zone is determined by the light grey area. From Figure 4.8.8 the maximum unsupported span is given as 3,0 m (assuming $F = 200$ kN and $b = 1,5$ m).

It is emphasised that the above stability zones are simplified approximations of the stability envelopes developed as part of GAP330 and GAP627 (Daehnke *et al.*, 1998, 1999). To fully optimise the support systems, it is recommended that the SDA II software or the 3D stability plots given by Daehnke *et al.* (1998, 1999) be used.

4.8.2.4 Support spacing requirements for rockburst conditions and hangingwalls with face-parallel fractures (FPFs)

The stability requirements for rockburst conditions and hangingwalls with FPFs follow analogously to the rockfall case. The hangingwall is assumed to be accelerated to a velocity of 3 m/s, which is decelerated over a distance of 0'2 m. The extent of the zones of support influence is calculated for an effective hangingwall weight taking into account the rock mass deceleration (see Daehnke *et al.*, 1998, 1999 for a description of the effective hangingwall weight concept).

Figure 4.8.9 gives the stability envelopes for rockburst conditions of a hangingwall with FPFs. As in the rockfall case, two stability zones (light and dark grey) are shown. The appropriate stability zone is dependent on the discontinuity angles (a and b) and friction angle (f).

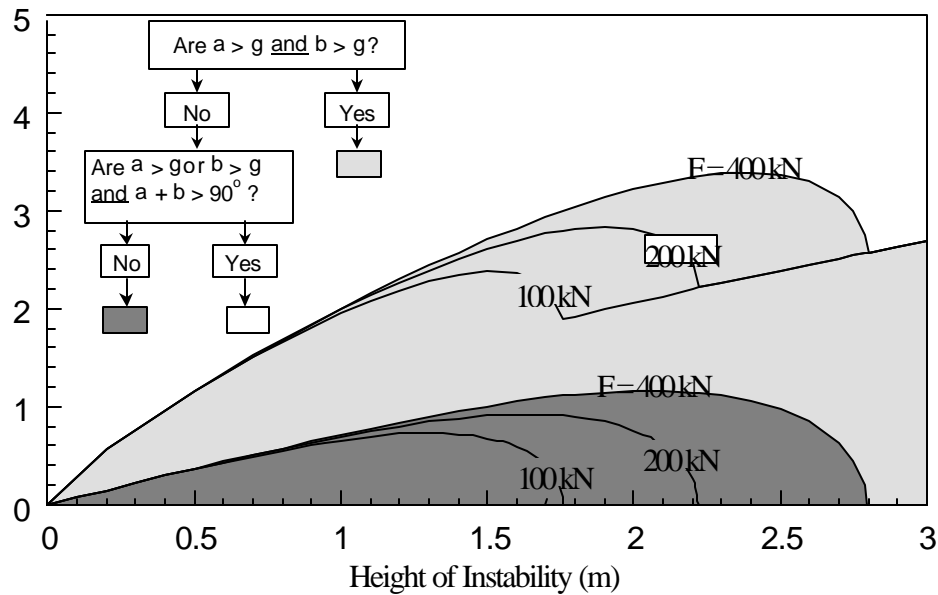


Figure 4.8.9 Rockburst stability envelopes for hangingwalls with FPFs as a function of instability height, unsupported span, support load and discontinuity orientation ($g = 90^\circ - f$, where f is the friction angle associated with the fracture surfaces).

As an example, consider the stability of the same hangingwall, discretised by face-parallel extension and shear fractures dipping at $a = 50^\circ$ and $b = 30^\circ$, respectively and $g = 40^\circ$, used in the previous section.

Are $a > g$ and $b > g$? No.
 Are $a > g$ or $b > g$ and $a + b > 90^\circ$? No.

Since $a + b < 90^\circ$, the dark grey stability zone is applicable (using the flowchart in Figure 4.8.9). Assuming a support unit load of $F = 200$ kN and height of instability $b = 1.5$ m, the maximum stable unsupported span is determined from Figure 4.8.9 as 0.9 m. (This is slightly less than for the rockfall case.) Note that, by installing props with headboards, the unsupported span remains the same, but the prop spacing can be increased by the length of the load spreader.

4.8.2.5 Support spacing requirements for rockfall conditions and blocky hangingwalls

The support spacing requirements described in the previous two sections are only applicable if the hangingwall stability is controlled by sliding, rotating or buckling keyblocks. This section summarises a second approach to support spacing requirements, which is particularly applicable for blocky hangingwall conditions (see, for example, Figure 4.8.10). The design charts are based on work conducted as part of SIMRAC project GAP335 (Haile *et al.*, 1998), and can be used to design the spacing requirements of both prop and tendon support units. A fundamental assumption of the design procedure given here is that, when applied to tendon support, the tendons are anchored beyond the potentially unstable zone into the more competent overlying rock mass. Furthermore, if yielding tendons are used, the required yield length must lie above the potentially unstable zone (see Figure 4.8.11).



Figure 4.8.10 **Example of a blocky hangingwall.**

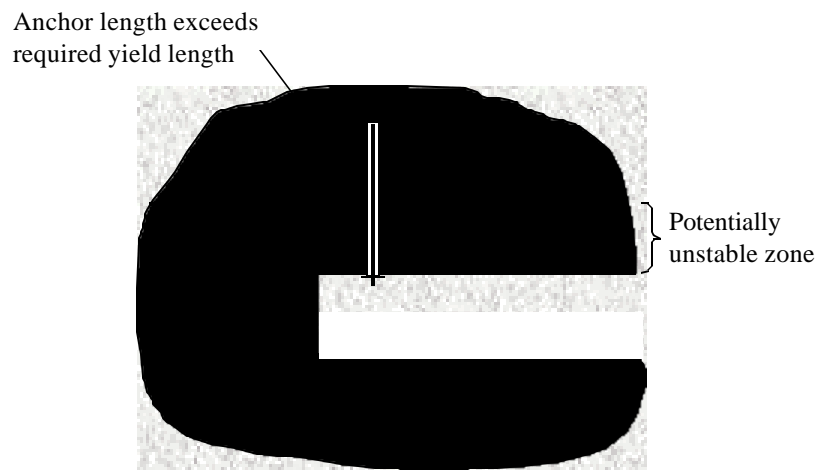


Figure 4.8.11 **Length requirements of yielding tendons.**

Haile *et al.* (1998) found that the critical rock mass parameters determining the stability of blocky rock mass structures are the aspect ratio and the volume of the blocks. Based on the findings of numerical models, these two parameters were found to satisfactorily express the variations in size and geometry of the blocks that make up the rock mass structure, and reflect their relative stability. This correlation is best expressed in the form of a log-log plot, where linear divisions between the rock mass classes, which are based on the relative stability with regard to rock mass unravelling potential, are made (Figure 4.8.12). Also indicated on this chart are equivalent RQD (Rock Quality Designation) values as derived from the work of Palmstrøm (1996).

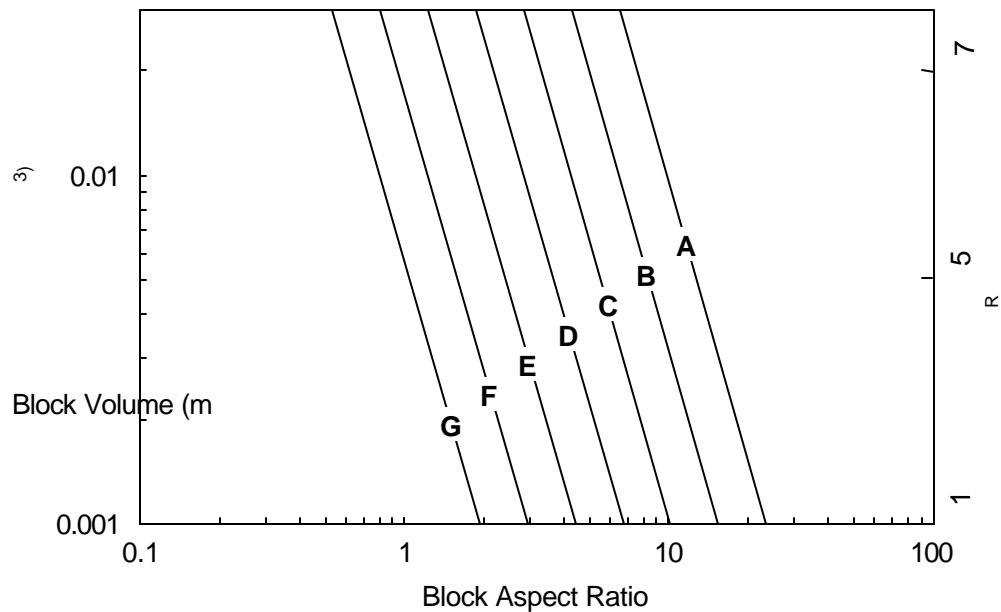


Figure 4.8.12 *Classification of a rock mass on the basis of the aspect ratio parallel to the hangingwall skin and the volume of the blocks.*

Once the rock mass classification is established, the stability of the rock mass between adjacent support units can be determined. This relationship, as derived from numerical modelling (Haile *et al.*, 1998), is illustrated in Figure 4.8.13. The relationship is given as a function of depth of instability, from a completely stable span, to a 1.5 m depth of instability. In practice, the rock mechanics engineer should always design to achieve a stable span. In certain situations, however, a limited amount of rock fallout between adjacent support units will be predicted to occur. If the resulting arches are unstable, areal coverage or reduced spacing of support units is required to prevent stope workers from rock hazards.

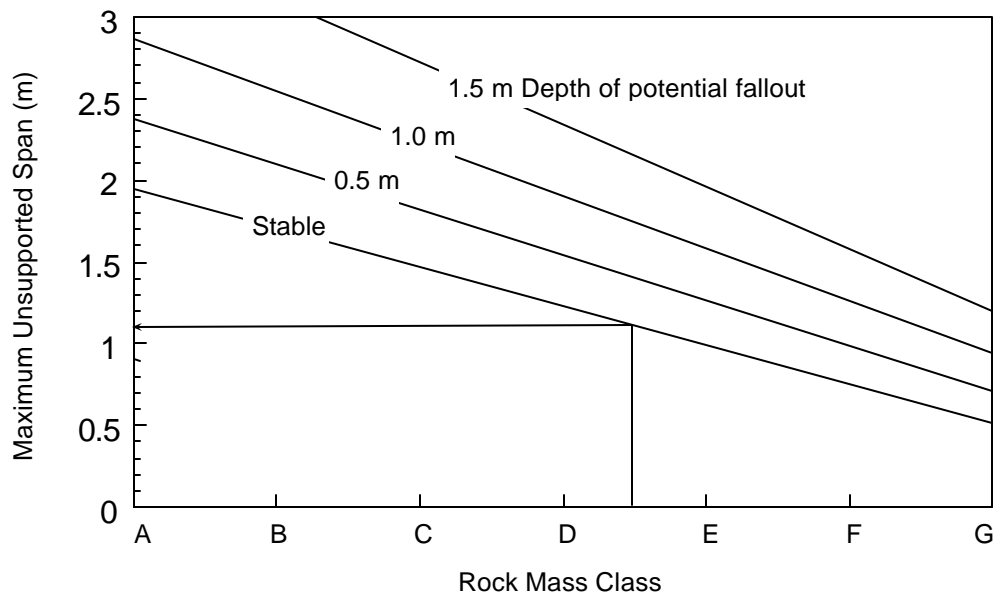


Figure 4.8.13 *Maximum unsupported span for blocky rock mass structures as a function of rock mass class and depth of instability (rockfall conditions)*

An example is given to illustrate the application of Figures 7.2.52 and 7.2.53. Consider a blocky rock mass structure with blocks that are approximately 15 cm in length in the strike direction, 30 cm in the dip direction, with a thickness of 5 cm. This would give an average estimated block volume of $0,002 \text{ m}^3$ and an average aspect ratio in the strike direction of 3 and in the dip direction of 6. For a simplified analysis the average aspect ratio (4,5) should be used. For a more detailed analysis the spacing in the strike and dip directions can be related to the aspect ratios in the corresponding directions, i.e. Figures 7.2.52 and 7.2.53 are used twice to determine the strike and dip spacing based on the respective aspect ratios.

From Figure 4.8.12, considering an aspect ratio of 4,5 and block volume of $0,002 \text{ m}^3$, a rock mass class of D/E is found. Using Figure 4.8.13, a rock mass class of D/E implies a maximum unsupported span of 1,1 m to ensure a stable hangingwall. The recommended support spacing is applicable for both prop and tendon support spacing, provided the tendons are long enough to be anchored in competent rock.

4.8.2.6 Support spacing requirements for rockburst conditions and blocky hangingwalls

For rockburst conditions Figure 4.8.12 is used to determine the appropriate rock mass class, based on the geometrical parameters of the blocks. Figure 4.8.14 is then applied to estimate maximum unsupported spans as a function of rock mass class and depth of instability. Figure 4.8.14 is based on dynamic correction factors established by Haile *et al.* (1998), where the block ejection velocity is assumed to be 3 m/s and the reduced support spacing for dynamic conditions is proportional to the anticipated increase in the depth of instability.

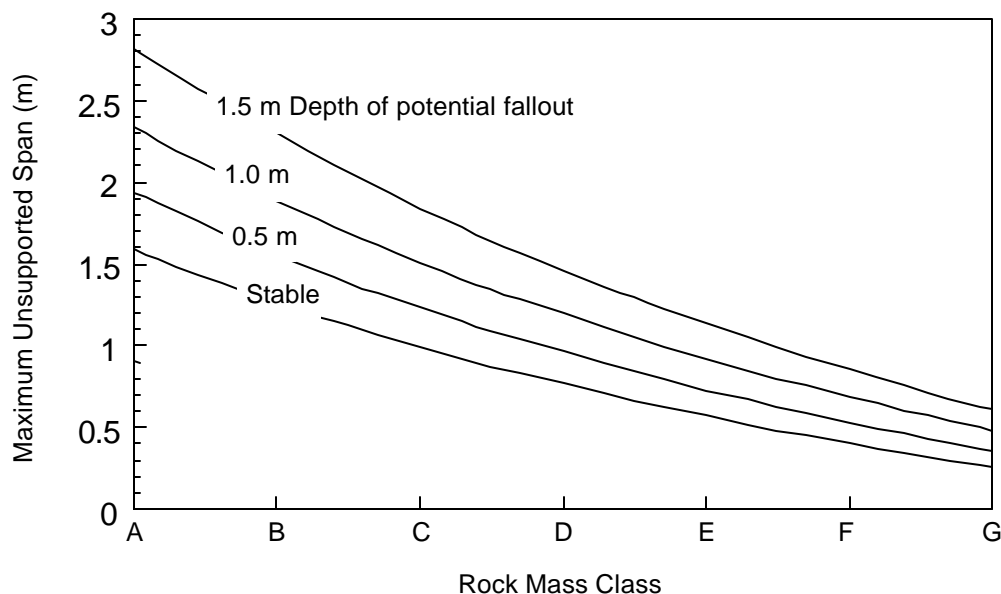


Figure 4.8.14 Maximum unsupported span for blocky rock mass structures as a function of rock mass class and depth of instability (rockburst conditions).

4.8.2.7 Support spacing calculation procedure

Support spacing for hangingwalls with FPFs

The support design method gives insights into spacing and associated stable hangingwall spans in the strike direction only. Due to the face-parallel mining-induced fracture orientation in intermediate and deep level mines, the hangingwall rock is generally less prone to failure between two support units in the dip direction, compared to failure between units in the strike direction. Probabilistic keyblock analyses (Daehnke *et al.*, 1998) have shown that, for a typical discontinuity spacing and attitude as encountered in intermediate depth and deep gold mines, the support spacing in the dip direction can be increased by a factor of $\pm 1,5$ compared with the strike spacing, while maintaining an equal probability of keyblock failure in the dip versus strike direction. Hence, to propose a prudent system, it is recommended that the support spacing in the dip direction can be up to but should not exceed 1,5 times the spacing in the strike direction. This simplifies the design procedure by eliminating the need for complicated three-dimensional analyses. Furthermore, this relationship has been found to be generally valid in practice, but, however, may not apply in blocky ground such as can be expected in sections of lagging panels which intersect siding parallel fractures.

In order to determine the strike and dip spacing of support units, the following calculation procedure is proposed:

The centre-to-centre strike spacing (s_s) of support units is calculated as:

$$s_s = \min \left\{ \begin{array}{l} \sqrt{\frac{T_A}{1.5}} \\ s_{FPF} + w \end{array} \right. , \quad [53]$$

where: T_A = maximum potential tributary area (from Figures I and II, overleaf)
 s_{FPF} = maximum stable span for hangingwalls with FPFs (from Figures III and IV, overleaf)
 w = width of the support unit or headboard.

The unsupported span in the dip direction can be up to but must not exceed 1,5 times the unsupported span in the strike direction.

Support spacing for blocky hangingwalls

For blocky hangingwalls, the centre-to-centre strike spacing (s_s) of support units is calculated as:

$$s_s = \min \left\{ \begin{array}{l} \sqrt{T_A} \\ s_B + w \end{array} \right. , \quad [54]$$

where: T_A = maximum potential tributary area (from Figures I and II, overleaf)

s_B = maximum stable span for blocky hangingwalls (from Figures V, VI and VII, overleaf)
 w = width of the support unit or headboard.

The centre-to-centre dip spacing of support units is recommended to be approximately equal to the centre-to-centre strike spacing.

4.8.3 Support Design Procedures

In this section support design procedures, based on (i) shallow and intermediate/deep mines and (ii) hangingwalls with face-parallel fractures and blocky hangingwalls, are proposed. Design flowcharts are given to facilitate the convenient use of the appropriate design charts in Figures 4.8.15 and 4.8.16 for shallow mines and intermediate- and deep-level mines, respectively.

For hangingwall conditions in which both the stability of keyblocks, as well as the unravelling of a blocky rock mass structure governs the rock mass integrity, it is recommended to determine the maximum stable spans for both blocky hangingwalls and hangingwalls with FPFs. In this case, the ultimate support spacing to be used should be the minimum of the blocky hangingwall and hangingwall with FPFs analyses.

Finally, the rock engineer should at all times apply his/her engineering judgement to design support systems offering a high probability of rock mass stability. The work presented here considers only two fundamental failure mechanisms and may well be unsuitable for particular geotechnical areas. At all times a conservative approach should be taken to support system design. For particularly complex rock mass structures and/or poorly understood failure mechanisms, support spacing should be further reduced and support resistance and energy absorption capacities increased.

Shallow Mines

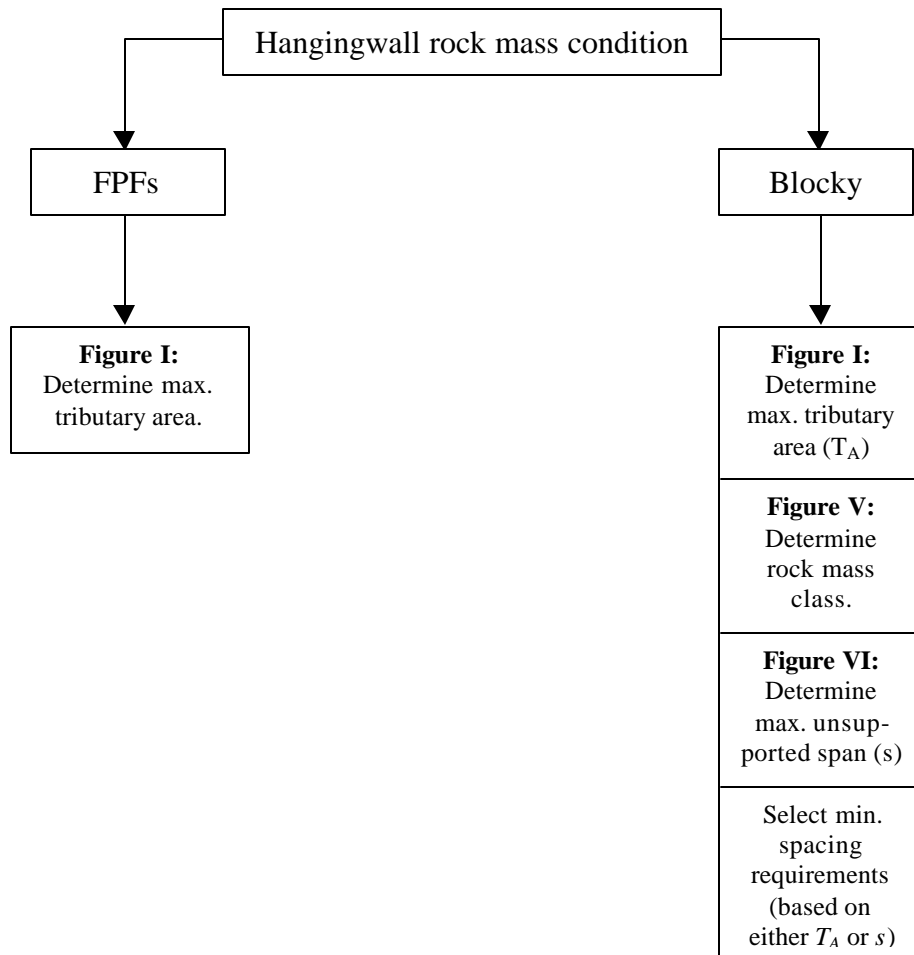


Figure 4.8.15 **Design flowchart for shallow mines (figures given overleaf).**

Intermediate- and Deep-Level Mines

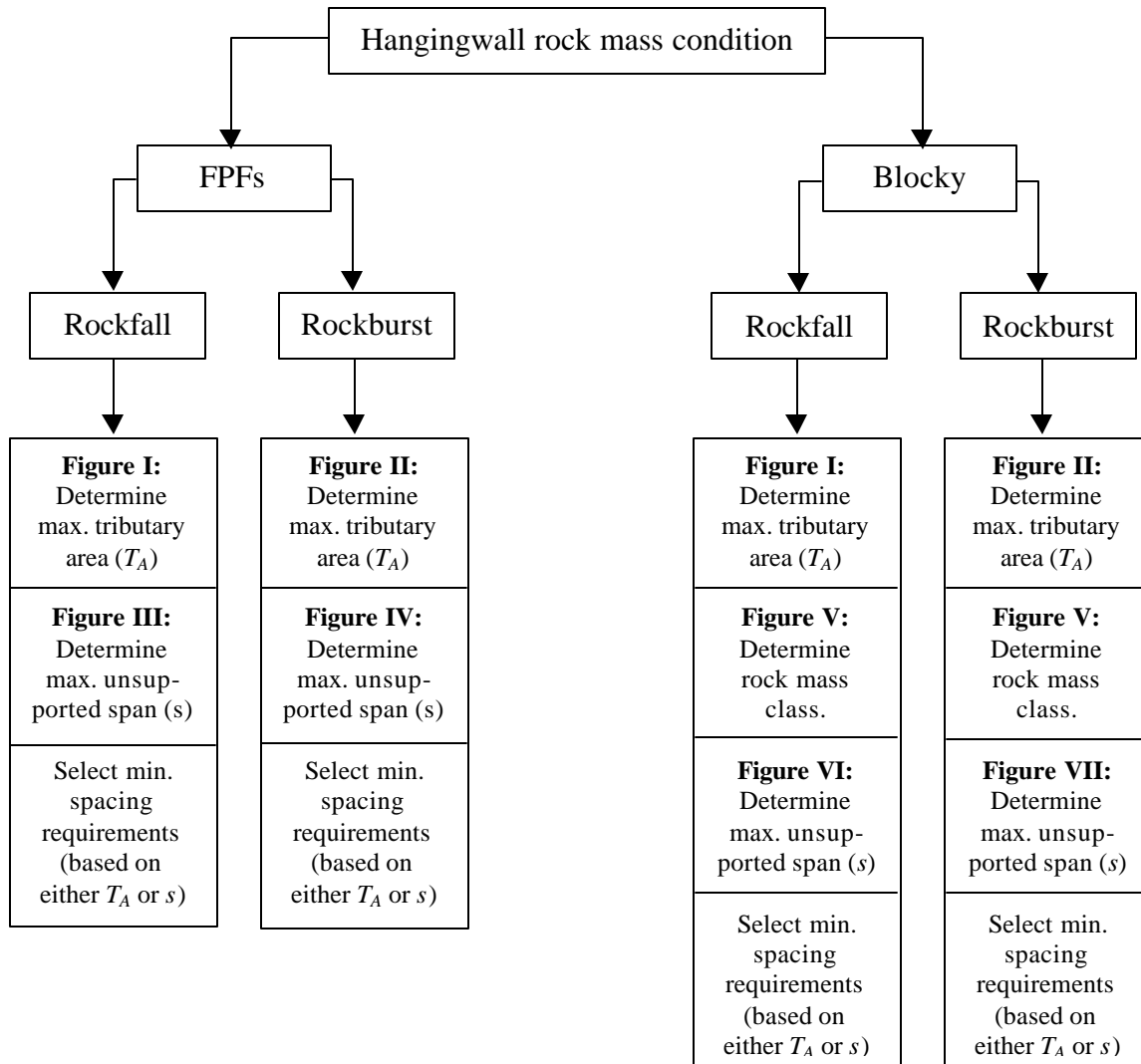


Figure 4.8.16

Design flowchart for intermediate- and deep-level mines (figures given overleaf).

Tributary Area Analyses

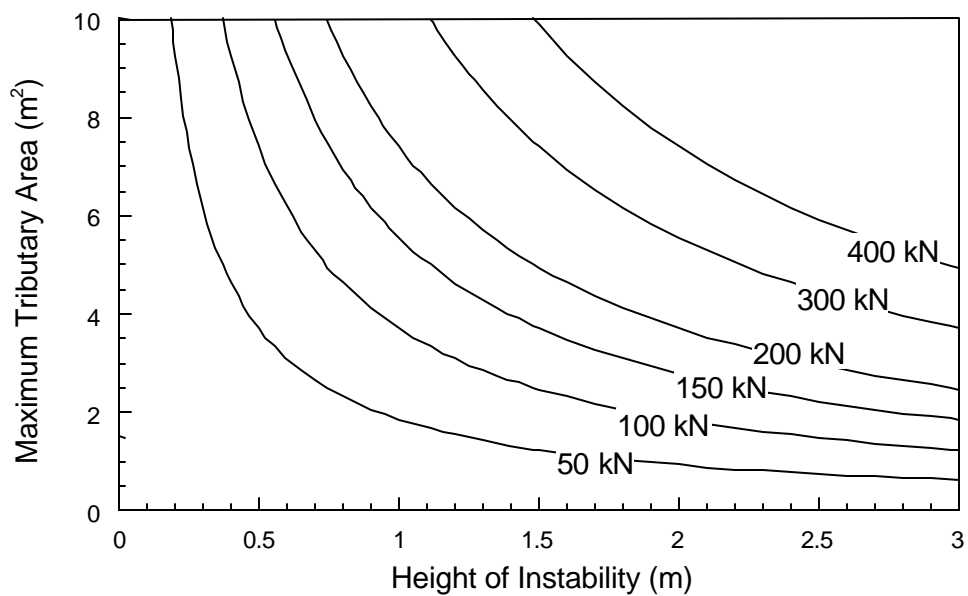


Figure I Tributary area requirements for rockfall conditions.

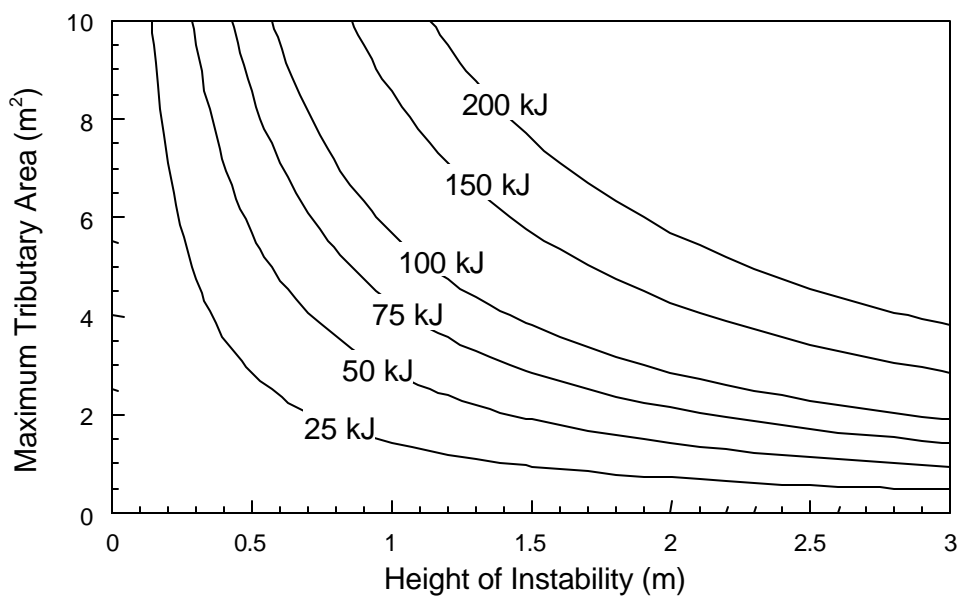


Figure II Tributary area requirements for rockburst conditions.

Stability Analyses for Hangingwalls with FPFs

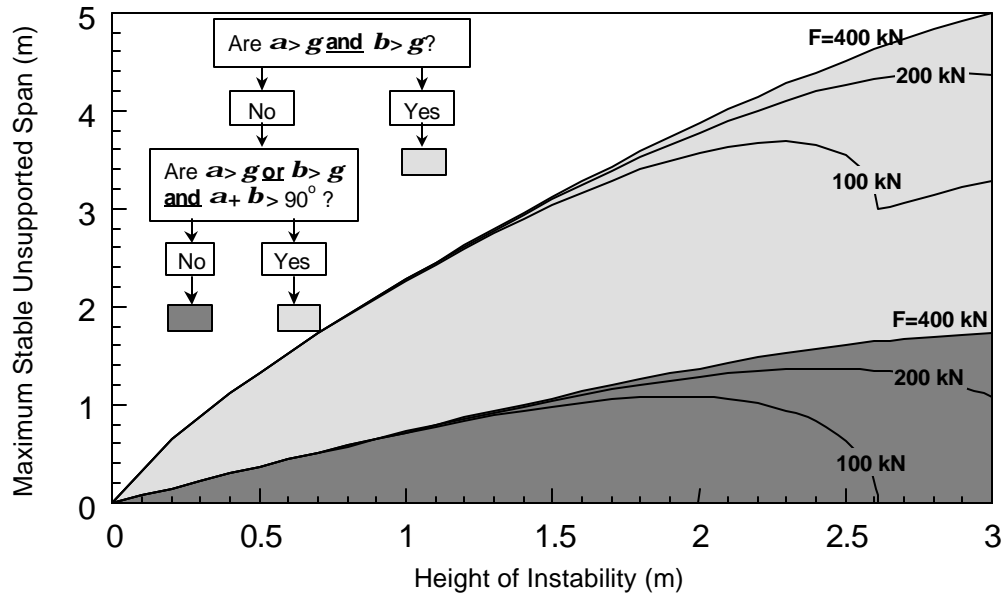


Figure III Rockfall stability envelopes for hangingwalls with FPFs ($g = 90^\circ - f$, where f is the friction angle associated with the fracture surfaces).

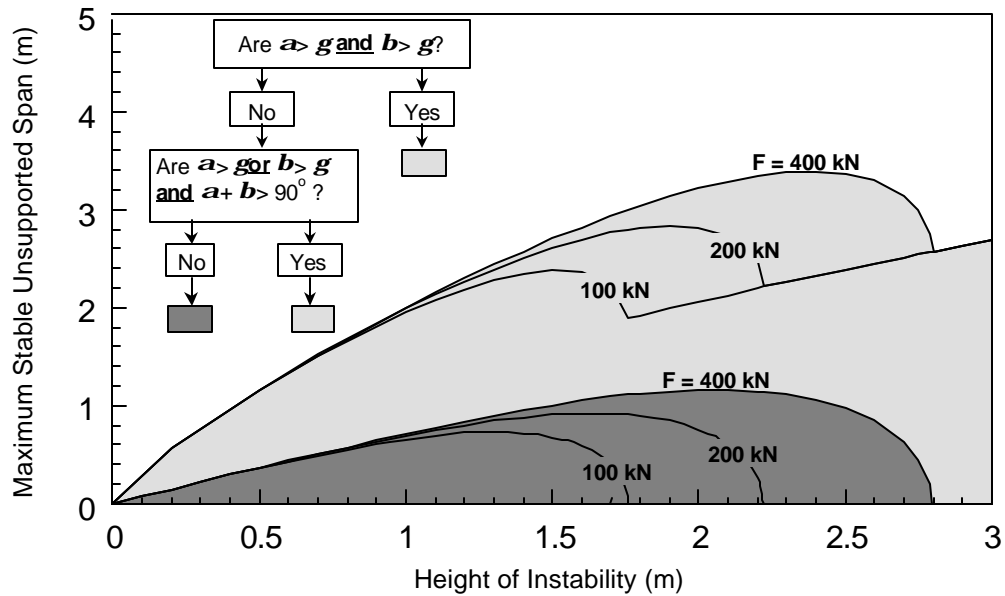


Figure IV Rockburst stability envelopes for hangingwalls with FPFs ($g = 90^\circ - f$, where f is the friction angle associated with the fracture surfaces).

Stability Analyses for Blocky Hangingwalls

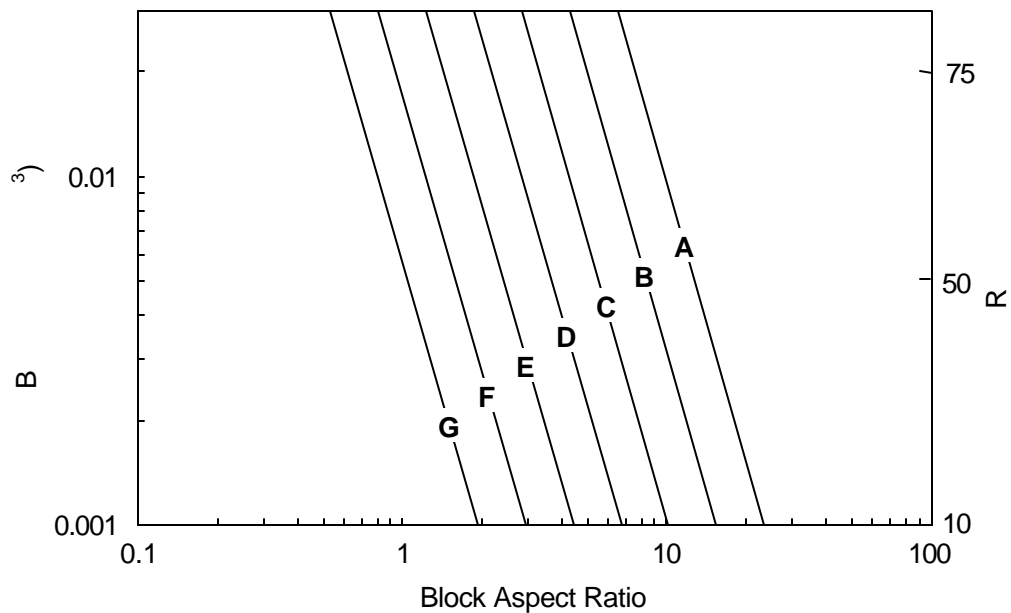


Figure V *Classification of a rock mass on the basis of the aspect ratio parallel to the hangingwall skin and the volume of the blocks.*

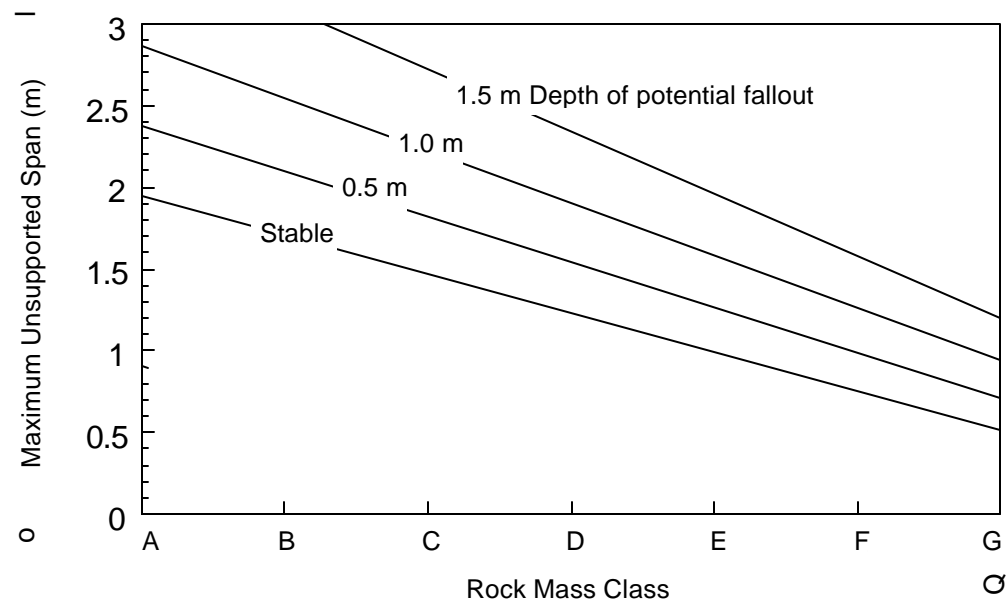


Figure VI *Maximum unsupported span for blocky rock mass structures as a function of rock mass class and depth of instability (rockfall conditions).*

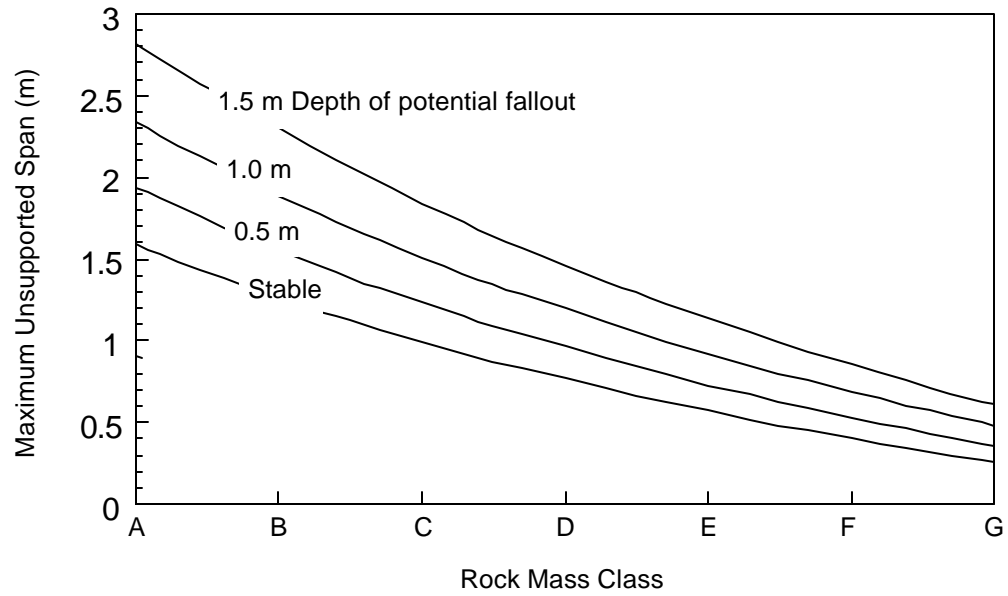


Figure VII *Maximum unsupported span for blocky rock mass structures as a function of rock mass class and depth of instability (rockburst conditions).*

Support Design Example

To illustrate the support design procedure, the optimum spacing of Loadmaster props in an intermediate depth mine for rockfall and rockburst conditions is determined. The height of instability (hangingwall beam thickness) is 1,0 m, the closure rate is 20 mm per metre of face advance, the stoping width is 1,6 m, and the hangingwall is discretised by extension and shear fractures dipping at 80° and 60°, respectively. The hangingwall is smooth, and the sliding, rotational and buckling failure of keyblocks governs the hangingwall stability.

A. Rockfall Conditions

A1. *Determine force versus deformation characteristics of Loadmaster props:*

By means of laboratory compression tests, the 1,6 m Loadmaster force versus deformation characteristics shown in Figure 4.8.17 were established (the characteristics of the most commonly used elongate types are given in Daehnke *et al.*, 1998). Ten laboratory compression tests were conducted and Figure 4.8.17 shows the mean of the 10 tests, as well as the 90 % probability curve (further details of probability curves are given by Daehnke *et al.*, 1998). In this example, the 90 % probability curve is used as the reference force versus deformation curve of the Loadmaster prop.

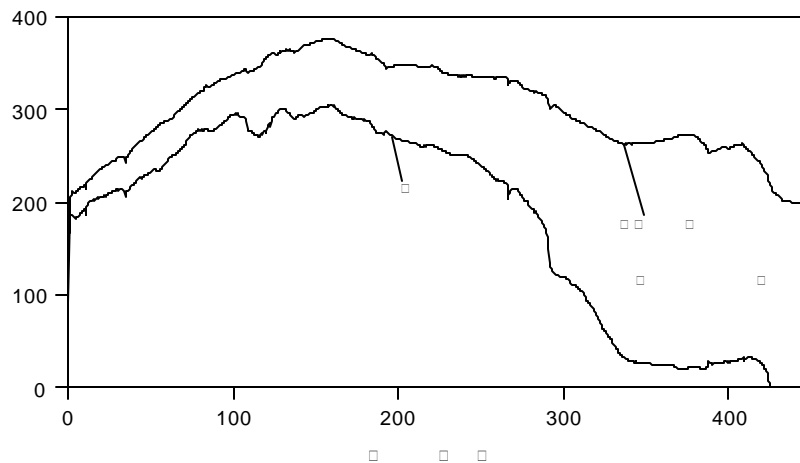


Figure 4.8.17 **Force versus deformation characteristics of the Loadmaster prop**

The Loadmaster reference curve is downgraded for loading rate by the following equation (Roberts, 1995):

$$F_{u/g} = F_{lab} \left[m \log \left(\frac{v_{u/g}}{v_{lab}} \right) + 1 \right],$$

where: $F_{u/g}$ = adjusted force
 F_{lab} = original force as measured during laboratory test
 v_{lab} = laboratory test velocity
 $v_{u/g}$ = underground site velocity
 m = empirically determined correction factors,
 where: $m = 0,123$ for rockbursts, and
 $m = 0,084$ for rockfalls.

The corrected 90 % design curve is shown in Figure 4.8.18 ($v_{lab} = 30 \text{ mm/min}$, $v_{u/g} = 20 \text{ mm/day}$ assuming the face is advanced every day).

Correction factors for stopping width are given by Roberts (1995). Since the stopping width in this example is 1,6 m, and the length of the laboratory tested Loadmaster was 1,6 m, no correction for prop height is necessary.

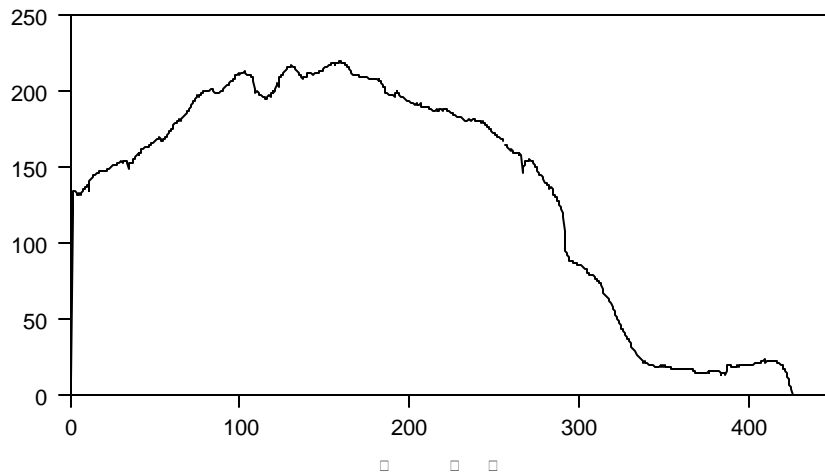


Figure 4.8.18 **Corrected Loadmaster reference curve (90 % probability)**

A2. Tributary area spacing requirements:

From Figure 4.8.18 it is apparent that the prop is initially set at a load of 135 kN. The yield load exceeds this value up to a total deformation of 285 mm. At a closure rate of 20 mm/m face advance, this implies that the prop will exceed 135 kN up to a distance of 14,25 m behind the stope face. This is considered a suitable working lifespan for the prop to ensure hangingwall stability in the working area, and hence the tributary area spacing requirements are based on a single support unit carrying 135 kN. From Figure I it is evident that, with $F = 135 \text{ kN}$ and height of instability $b = 1,0 \text{ m}$, the maximum tributary area should not exceed $4,5 \text{ m}^2$.

A3. Hangingwall with FPFs stability analysis:

For extension and shear fracture angles of $\alpha = 80^\circ$ and $\beta = 60^\circ$, respectively, the light grey zone of Figure III is applicable (assuming a friction angle $\phi = 50^\circ$). The maximum unsupported span in the strike direction, at $b = 1,0 \text{ m}$, is $s_{FPF} = 2,2 \text{ m}$.

The recommended support spacing should be based on the minimum of the tributary area spacing and the maximum unsupported strike span requirements. When using props without headboards, the strike spacing (centre to centre) of the props is approximately equal to the unsupported span. Hence, $T_A = s_s \times s_d$, where T_A is the tributary area and s_s , s_d are the strike and dip spacing of support units. In this example $T_A \leq 4,5 \text{ m}^2$. Using Equation 53, the recommended centre-to-centre strike spacing (s_s) is calculated as:

$$s_s = \min \left\{ \begin{array}{l} \sqrt{\frac{T_A}{1.5}} \\ s_{FPF} + w \end{array} \right\} = \min \left\{ \begin{array}{l} \sqrt{\frac{4.5}{1.5}} \\ 2.2 \end{array} \right\} = 1.73 \text{ m.}$$

The dip spacing can be up to, but must not exceed, $1,5 s_s = 2,60 \text{ m}$. Thus, a strike spacing of 1,73 m and dip spacing of 2,60 m is recommended.

B. Rockburst Conditions

B1. *Determine the energy absorption capacity of Loadmaster props:*

Figure 4.8.19 shows the force versus deformation characteristics of a Loadmaster prop loaded dynamically. The mean of 10 laboratory compression tests, as well as the 90 % probability curve, is given. The prop was initially compressed at a slow rate over a distance of 80 mm. Thereafter the prop was rapidly compressed at a rate of 3 m/s over a distance of 200 mm, followed once again by slow loading.

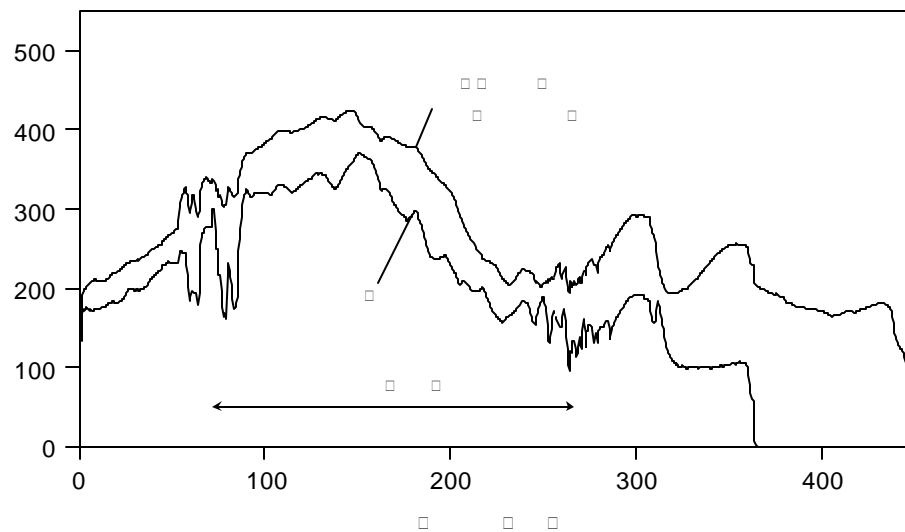


Figure 4.8.19 ***Dynamic force versus deformation characteristics of the Loadmaster prop.***

Figure 4.8.20 gives the remaining energy absorption capacity of the Loadmaster prop (based on the 90 % reference curve given in Figure 4.8.19). From the graph it is apparent that between 80 mm and 280 mm dynamic compression, 50,8 kJ of energy is absorbed.

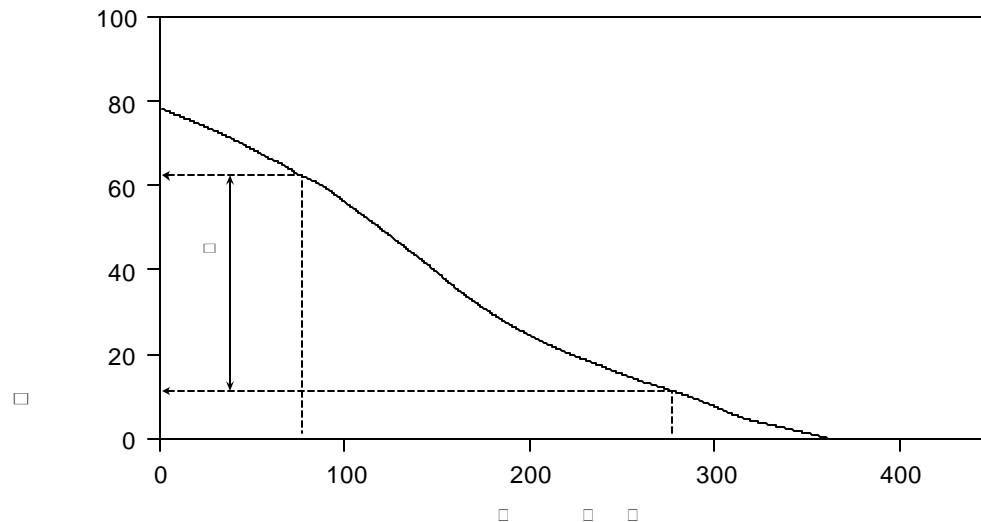


Figure 4.8.20 *Energy absorption capacity of the Loadmaster prop.*

B2. Tributary area spacing requirements:

Assuming the prop is subjected to rockburst loading (3 m/s over 0,2 m) after 80 mm of quasi-static convergence, 50,8 kJ of energy can be absorbed. From Figure II, at a height of instability of 1,0 m and 50 kJ, the maximum tributary area for rockburst conditions is found to be 2,9 m².

Further rockburst support criteria that need to be satisfied are:

- (i) The load carried by the support unit after the rockburst must exceed the corresponding tributary area load. In this example $F(280 \text{ mm}) = 140 \text{ kN}$ (from Figure 4.8.18), which is adequate to support the tributary area load $= r g b T_A = 78 \text{ kN}$.
- (ii) The stoping width minus the total closure after the rockburst should be adequate to prevent injury to and allow movement of mine personnel ($> 0,6 \text{ m}$ is recommended). In the example given here the initial stoping width is 1,6 m and thus the post-rockburst stoping width ($1,6 \text{ m} - 0,08 \text{ m} - 0,2 \text{ m} = 1,32 \text{ m}$) is adequate.

Note that by checking the energy absorption capacity of the prop after 80 mm of quasi-static convergence, it is implied that the prop will meet the rockburst criteria as the face is advanced a further 4 m ($80 \text{ mm} \div 20 \text{ mm/m face advance}$). At prop to face distances exceeding 4 m plus the installation distance from the face, the rockburst criteria are not necessarily met and the energy absorption capacity, post-rockburst support resistance or post-rockburst stoping width may be inadequate.

B3. Hangingwall with FPFs stability analysis:

For extension and shear fracture angles of $a = 80^\circ$ and $b = 60^\circ$, respectively, the light grey zone of Figure IV is applicable (assuming a friction angle of $f = 50^\circ$). The maximum unsupported span in the strike direction, at $b = 1,0 \text{ m}$, is $s_{FPF} = 1,9 \text{ m}$.

The centre-to-centre strike spacing (s_s) is calculated using Equation 53, i.e.

$$s_s = \min \left\{ \sqrt{\frac{T_A}{1.5}}, s_{FPF} + w \right\} = \min \left\{ \sqrt{\frac{2.9}{1.5}}, 1.9 \right\} = 1.39 \text{ m.}$$

The dip spacing can be up to, but must not exceed, $1,5 s_s = 2,09 \text{ m}$. Thus, a maximum strike spacing of 1,39 m and dip spacing of 2,09 m is recommended.

Note that in the case of shallow dipping fractures ($\alpha < 40^\circ$ and $\beta < 40^\circ$ if the fracture surface friction angle $f = 50^\circ$) the maximum strike spacing is limited to 0,75 m and 0,65 m for rockfall and rockburst conditions, respectively (determined from Figures III and IV for $b = 1.0 \text{ m}$). In this case considerably closer support spacing and/or the use of strike parallel headboards is recommended.

4.8.4 Conclusions

It is clear from the above discussion that the proposed design procedure provides a link between the continuous and discontinuous analyses. This is accomplished by making use of the zones of support influence to determine the length of the unsupported beam, s , and using this length in the discontinuous analysis. This method is not as conservative as the present design methodology, where the continuous and discontinuous analyses are independent of each other, and will thus allow for more optimal designs.

A unified methodology to evaluate support systems catering for rockfall and rockburst conditions is proposed. The method consists of two stages: (i) a tributary area analysis, and (ii) a zone of influence analysis, which determines the general support resistance and spacing requirements for the support system as a whole, and a stability analysis considering hangingwall failure due to buckling, shear and block rotation, which gives maximum safe spacing of individual support units.

The new design methodology also combines both the zone of influence and keyblock stability theories, thus providing an improved support design tool. It is recommended that, following *in situ* evaluations of the support design methodology proposed here, the methodology be incorporated in a program such as SDA for use in the industry.

It is further recommended that additional work be conducted to quantify the effects of arbitrarily oriented discontinuities of geological origin on support spacing in the strike and particularly the dip directions. Further work could also re-address the influence of the modified hangingwall stress distribution and zones of influence due to loading by the stope face, support units and backfill. The horizontal clamping stress is a vital part of the design procedure. Further work needs to be done to clarify the magnitude and role of this important component.